Application of Engineered Porosity and Modified Effective Moduli to the Design of Orthopaedic Implants

John Anthony Choren
Marquette University

APPLICATION OF ENGINEERED POROSITY AND MODIFIED EFFECTIVE MODULI TO THE DESIGN OF ORTHOPAEDIC IMPLANTS

by

John Anthony Choren, P.E.

A Dissertation submitted to the Faculty of the Graduate School,
Marquette University,
in Partial Fulfillment of the Requirements for
the Degree of Doctor of Philosophy

Milwaukee, Wisconsin

December 2011

ABSTRACT
APPLICATION OF ENGINEERED POROSITY AND MODIFIED EFFECTIVE MODULI TO THE DESIGN OF ORTHOPAEDIC IMPLANTS

John Anthony Choren, P.E.

Marquette University, 2011

Commercially available orthopaedic implants have a bending stiffness (flexural rigidity) that is at least 10 times greater than cortical bone. Effects of this stiffness mismatch have been extensively studied relative to total hip arthroplasty (THA). Clinical experience with THA has shown that stiffness mismatch is the primary cause of accelerated bone resorption due to the stress shielding, resulting in sub-optimal bone loading, aseptic loosening and inadequate bone support for a future revision implant.

Attempts to incorporate design features that reduce the flexural rigidity of implants have yielded inconsistent results or failures due to biomaterial incompatibilities and practical manufacturing complications. The recent development of additive manufacturing (AM) processes allow the fabrication of closed-cell porous Ti or CoCr microstructures as a practical means of fabrication while reducing implant stiffness.

The use of engineered porosity to modify flexural rigidity requires an ability to predict moduli from microstructural parameters. The literature is replete with different formulas which are often contradictory; existing equations relating porosity to effective moduli are generally interpretive and not predictive.

This study applied finite element methods to three-dimensional porous structures with different arrangements of spheroidal voids. The resulting data show that the effective Young's modulus varies linearly with ψ, the ratio of pore radius to center-to-center dimension, for a porosity range of 20 to 50%. In addition, the arrangement of spherical voids was found to have only a minimal effect on the resultant Young's modulus. Predictive equations for Poisson's ratio are second-order and dependent upon the void arrangement. The effect of changes in loading direction on moduli indicate that the three microstructures evaluated in this study are anisotropic, with anisotropy increasing with both ψ and volume porosity. The predictive equations developed in this study were validated with AM fabrication and testing of prototypical Ti6Al4V spinal rods. Constructs of a rhombohedral (FCC) pore arrangement with 30% porosity showed an effective reduction of ~ 50% in Young's modulus. Predicted values for flexural rigidity fell within 95% confidence intervals for the tested porous Ti6Al4V constructs, confirming a design methodology with the potential of reducing the flexural rigidity, and resulting bone resorption, of orthopaedic implants.

ACKNOWLEDGEMENTS

John Anthony Choren, P.E.

This work could not have been completed without the assistance of many people who gave generously of their time. Among those to whom I owe thanks is Jordan Weston, who helped me with my SolidWorks solid modeling challenges, and Thomas F. Schuppe, Ph.D., who although retired from teaching at MSOE, gave freely of his time to help me with the statistical analyses of the study data. I also appreciate the assistance given me by Mylin Cumberland, DePuy Orthopaedics, Inc., Magnus René, Arcam AB, and Stefan Ritt, SLM Solutions GmbH, who graciously provided prototype implants for testing.

I also want to thank the members of my Committee, Dean C. Jeutter, Ph.D., P.E., Stephen M. Heinrich, Ph.D., Joseph C. Musto, Ph.D., P.E., Jeffrey M. Toth, Ph.D., and Mei Wang, Ph.D., who were always available with thoughtful advice, assistance and encouragement.

Of all those at Marquette, I am most grateful for the patience and support given to me by my Advisor and Dissertation Director, M. Barbara Silver-Thorn, Ph.D. Dr. Silver-Thorn was the first person I spoke to when I walked into the Biomedical Engineering department nine years ago and she has been supportive of my efforts ever since. I could not have accomplished this work without her help.

I also want to acknowledge my father, Anthony M. Choren, B.S.M.E., University of Wisconsin, 1941, for providing the inspiration, persistence and intellectual curiosity needed for me to become an engineer in the first place.

Most importantly, I need to recognize and thank my wonderful wife, Suzanne M. Choren for putting up with the long hours spent in completing this work. She has been totally supportive throughout this entire nine-year process and was always there to encourage and support me when the work became difficult.

This work is dedicated to you, Lady Sue.

TABLE OF CONTENTS

LIST OF TABLES

LIST OF FIGURES

APPLICATION OF ENGINEERED POROSITY AND MODIFIED EFFECTIVE MODULI TO THE DESIGN OF ORTHOPAEDIC IMPLANTS

1. Introduction

1.1 Problem statement

Joint replacement surgery has been performed to relieve pain and restore joint function for more than 50 years and has become a relatively common procedure. These procedures typically involve lower extremity joints. The most recent data from the CDC's National Center for Health Statistics summarizes that 230,000 hip replacement and 540,000 knee replacement surgeries were performed in the U.S. in 2007 alone [1]. The success of these surgeries is dependent upon the use of biocompatible materials, satisfactory design of the endoprosthesis or implant itself and proper operative techniques [2].

Design of the implant is complicated by the large bending stiffness (or flexural rigidity) of orthopaedic implants which is at least 10 times greater than cortical bone. Effects of this stiffness mismatch have been extensively studied relative to total hip arthroplasty (THA) and clinical experience has shown that stiffness mismatch is the primary cause of accelerated bone resorption due to stress shielding. This response to sub-optimal bone loading can lead to loss of proximal support [3], implant subsidence [4], potential bone fracture [5], possible fatigue fracture of the implant [6], and, most importantly, reduction of bone stock that jeopardizes the outcome of any future revision surgery [7, 8, 9, 10, 11, 12, 13].

Despite widespread awareness of these factors, the problem of implant stiffness has not been completely solved. Research suggests that flexural rigidity should vary along the length of the prosthesis using "anisotropic" materials with a defined structure to allow a "distribution of elastic properties inside the stem" [14, 15, 16] or within other implant configurations.

Past attempts to incorporate design features that reduce flexural rigidity have yielded inconsistent results or failures due to biomaterial incompatibilities and practical manufacturing complications. Recent developments in additive manufacturing (AM) processes allow the production of closed-cell porous microstructures in titanium or cobalt-chromium as a practical means of implant fabrication while offering the potential of reduced implant stiffness. The application of engineered porosity may provide these desired properties because, as the engineer/architect Robert le Ricolais (1894-1977) noted, "…the art of structure is where to put the holes."

The design of porous structures with the potential to usefully modify the flexural rigidity of an implant requires an ability to predict moduli from microstructural parameters. The literature is replete with different formulas describing purported relationships between porosity and mechanical properties which are often divergent and sometimes contradictory [17]. Additionally, existing equations relating porosity to effective moduli are generally interpretive and not predictive.

Given, first, the clinical concerns relative to bone loss due to the stiffness mismatch between bone and implant, second, the possible use and distribution of closed-cell porosity to modify the effective moduli of an implant, and thirdly, recent developments in practical AM technology, the primary research question to be addressed by this work is…

> *Can engineered porosity be applied to predictably reduce the flexural rigidity of an orthopaedic implant?*

1.2 Research objectives

The goal/purpose of this research is to develop a substantive answer to this question. The specific research objectives are:

1) to determine whether a relationship that accurately describes the effective moduli of a porous structure as a function of specific design parameters exists in the literature.

2) to refine an extant or develop a new predictive relationship by applying finite element (FE) methods to different microstructures incorporating these parameters.

3) to determine whether a porous structure can be designed and integrated in a prototypical implant segment.

4) to fabricate and test this implant design to refute or confirm the validity of the predictive equations.

5) to assess the clinical applicability of the methology to the design of reduced-stiffness implants.

This listing of research objectives effectively establishes the organization of the dissertation. Chapter 2 includes a review of research regarding the clinical effects of flexural rigidity, a function of moduli and geometry, on patient outcomes and implant design. A thorough review of the literature to determine the existence of predictive relationships for effective moduli as a function of porosity is detailed in Chapter 3. The application of FE methods to the evaluation of porous microstructures is described in Chapter 4. Chapter 5 summarizes the design, fabrication and testing of a prototypical implant to evaluate the validity of the predictive equations. Based on the results of this research, the clinical applicability of the evaluated methodology will be discussed in the Conclusions/Summary section.

1.3 References

[1] National Hospital Discharge Survey: 2007 Summary, *National Health Statistics Reports*, No. 29, October 26, 2010. Downloaded at http:// http://www.cdc.gov/nchs/data/nhsr/nhsr029.pdf.

[2] Joshi, M.G., Santare, M.H., Advani, S.G., *Survey of stress analyses of the femoral hip prosthesis*, ASME Applied Mechanical Review, Vol. 53, No. 1, pp. 1-18, 2000.

[3] Bobyn, Mortimer, Glassman, Engh, et al., *Producing and Avoiding Stress Shielding*, Clinical Orthopaedics and Related Research, Vol. 274, pp. 79-96, 1992

[4] Glassman, A., Bobyn, J., Tanzer, M., *New Femoral Designs: Do They Influence Stress Shielding?, Clinical Orthopaedics and Related Research, Vol. 453, pp. 64-74, 2006.*

[5] Huiskes, R., Weinans, H., Van Rietbergen, B., *The Relationship Between Stress Shielding and Bone Resorption Around Total Hip Stems and the Effects of Flexible Materials*, Clinical Orthopaedics and Related Research, Vol. 274, pp. 124-134, 1992.

[6] Lewis, J.L., Askew, M.J., Wixson, R.L. et al., *The Influence of Prosthetic Stem Stiffness and of a Calcar Collar on Stresses in the Proximal End of the Femur with a Cemented Femoral Component*, Journal of Bone and Joint Surgery, Vol. 66-A, No. 2, pp. 280-286, 1984.

[7] Brown, I.W., Ring, P.A., *Osteolytic Changes in the Upper Femoral Shaft Following Porous-Coated Hip Replacement*, Journal of Bone & Joint Surgery (Br), Vol. 67-B, No. 2, pp. 218-221, 1985.

[8] Karrholm, J., Anderberg, C., Snorrason, F., et al., *Evaluation of a Femoral Stem with Reduced Stiffness*, Journal of Bone and Joint Surgery, Vol. 84-A, No. 9, pp. 1651-1658, 2002.

[9] Engh, C.A., Bobyn, J.D., *The Influence of Stem Size and Extent of Porous Coating on Femoral Bone Resorption after Primary Cementless Hip Arthroplasty*, Clinical Orthopaedics and Related Research, Vol. 231, pp. 7-28, 1988.

[10] Engh, C.A., Young, A.M., Engh, C.A. Sr., Hopper, R.H., *Clinical Consequences of Stress Shielding After Porous-Coated Total Hip Arthroplasty*, Clinical Orthopaedics and Related Research, Vol. 417, pp. 157-163, 2003.

[11] Huiskes, R., Boeklagen, R., *Mathematical Shape Optimization of Hip Prosthesis Design*, Journal of Biomechanics, Vol. 22, No. 8/9, pp. 793-804, 1989.

[12] Nistor, L., Blaha, J.D., et al., *In Vivo Measurements of Relative Motion between an Uncemented Femoral Total Hip Component and the Femur by Roentgen Stereophotogrammetric Analysis*, Clinical Orthopaedics and Related Research, Vol. 269, pp. 220-227, 1991.

[13] Bugbee, W.D., Culpepper, W.J., Engh, C.A. Jr., Engh C.A. Sr., *Long-Term Clinical Consequences of Stress-Shielding after Total Hip Arthroplasty without Cement*, Journal of Bone and Joint Surgery, Vol. 79, No. 7, pp. 1007-1012, 1997.

[14] Kuiper, J.H., Huiskes, R., *Mathematical Optimization of Elastic Properties: Application to Cementless Hip Stem Design*, Journal of Biomechanical Engineering, Vol. 119, No. 2, pp. 166-174, 1997.

[15] Tensi, H.M., Gese, H., Ascherl, R., *Non-linear three-dimensional finite element analysis of a cementless hip endoprosthesis*, Proceedings of the Institution of Mechanical Engineers: Journal of Engineering in Medicine, Vol. 203, Part H, pp. 215-222, 1989.

[16] Niinimaki, T. J., Puranen, J.P., Jalovaara, P K., *Total Hip Arthroplasty Using Isoelastic Femoral Stems: A Seven- to Nine-Year Follow-Up in 108 Patients*, Journal of Bone & Joint Surgery (Br), Vol. 76-B, pp. 413-418, 1994.

[17] Hashin, Z, *The Elastic Moduli of Heterogeneous Materials,* Journal of Applied Mechanics,Vol. 29, pp.143-150, 1962.

2. Clinical relevance to orthopaedic design

2.1 Introduction

Early failures of acrylic and nylon prostheses created an impetus for the development and use of metal components in total hip arthroplasty (THA). However, problems associated with implant loosening along with proximal and distal migration tempered early enthusiasm for these designs [1]. Due in part to these issues, THA procedures, pioneered by Charnley in 1958, came to rely on acrylic bone cement for intramedullary fixation. The popularity of the Charnley technique was due to its high rate of success in older patients. However, a lower success rate became evident in younger patients, usually under age 40. Over the intervening years, painful loosening of the implant became more common [2]. By 1983, a National Institutes of Health consensus panel on THA named loosening as the number one problem with cemented prostheses [3]. The loosening of these cemented implants was frequently accompanied by severe osteolysis which complicated subsequent revision surgeries [4].

In response to these problems, press-fit cementless fixation, which relies on a larger, canal-filling geometry, was developed for use with young and active patients. One disadvantage of this increase in implant size is a larger mismatch in stiffness between the implant and the adjacent bone than would be typical of stems that rely on cement for fixation [5, 6].

Although the terms **stiffness** or **bending stiffness** are commonly used in the medical literature cited below, a more accurate term is **flexural rigidity** as it properly incorporates intrinsic material properties and extrinsic geometric features as the **product of the modulus of elasticity, E, and the moment of inertia, I**, at a given transverse cross section.

2.2 Flexural rigidity and bone resorption

Prior to the surgical insertion of the prosthesis, the hip joint load is carried directly by the bone, with loads applied to the head of the femur and forces distributed across the entire cross section of the femoral shaft. This loading leads to a homeostatic equilibrium in which the amount of stress-induced bone formation is balanced by the amount of bone loss associated with normal osteoclast activity [7, 8]. Bending and axial compression are the major modes of femoral loading prior to THA. After insertion, the load is transferred from the endoprosthesis to the bone through localized contact with the metaphysis and medullary cavity and as shear across the bone/prosthesis interface [9, 1].

In conceptual terms, the femur is a hollow tube that, due to its offset geometry, undergoes bending in response to ambulatory loads. Filling this hollow tube with a metal prosthesis stiffens the tube and accordingly reduces its ability to bend in response to the applied load [26]. As a result, the stresses in the cortical bone adjacent to the endoprosthesis are subnormal and the bone reacts with a reduction in cortical thickness. This is a natural process of strain-adaptive bone remodeling which, presumably, leads to a new equilibrium state [10, 7].

Research using dual energy X-ray absorptiometry (DEXA) indicates that a new state of equilibrium is not achieved and that bone loss, while diminished, is progressive over time [11]. The reduction in the physiologic load seen by the proximal bone results in a mechanically-induced osteopenia, generally referred to as “stress shielding”. There is no standard testing protocol, nor a consistent definition of this phenomenon [12].

Stress shielding refers to a reduction in the stress levels within the periprosthetic bone and cannot be perceived *per se*. Bone resorption is a physical manifestation of stress shielding consistent with the bone remodeling principles initially described by Wolff in 1892 [13, 14]. The

mechanical parameters that regulate periprosthetic bone loss are difficult to quantify. However, it is widely accepted that the greater the flexural rigidity of the implanted stem, the greater the extent of stress shielding in the proximal femur. This phenomenon, particularly in the case of relatively stiff stems, can cause bone mass reductions up to 50% [15].

Clinical concerns

A concern with THA prostheses is the possibility that resorptive bone remodeling will, in the long term, lead to loss of proximal implant support, implant subsistence and implant or bony fracture [13]. Research on local stresses and bone adaptation by Huiskes *et al.* [16] indicates that the most severe complication associated with joint replacement is aseptic loosening. This threatens the long-term structural integrity of the bone-prosthesis structure and the application of THA to younger (< 55 years) patients.

In a study that used dual-energy X-ray absorptiometry (DEXA) to assess bone loss, Kilgus *et al.* [17] reported a 35% reduction in bone mineral density in the area adjacent to the proximal third of the prosthesis after 5-7 years. In a subsequent study of periprosthetic bone remodeling, Sychterz *et al.* [18] reported that after ~ 6 years following THA, DEXA analyses disclosed an average 23% overall decrease in bone mineral content in the femur implanted with an prosthesis and that females experienced an average bone loss of 31%, significantly higher than the 12% average loss in males.

Studies by Lewis *et al.* [19] on the influence of prosthetic stem rigidity suggest that the loss of proximal support due to bone resorption, with firm fixation distally, may also be a major cause of fatigue failure of femoral stems. In their assessment of implant failures, Bauer *et al.* [20] add that maintaining initial mechanical fixation depends in part on maintaining local bone mass and minimizing bone resorption (osteolysis). Aside from these qualitative assessments, there

have been numerous studies aimed at measuring the extent and severity of this peri-implant bone loss. In an early DEXA study, Engh *et al.* [21] demonstrated that after an average of 5 years, the bone loss associated with cementless THA ranged from 7 to 52%, with the greatest loss in the femoral metaphysis proximal to the lesser trochanter. In a later study, Engh *et al.* [11] confirmed that adjacent to the proximal third of the prosthesis the extent of proximal bone loss was substantial and ranged from 27 to 78%.

In a recent review of femoral designs, Glassman *et al.* [22] conclude that the loss of supportive bone may predispose patients to progressive implant migration in the absence of loosening. Thus, whether the clinical concern is initial fixation, loosening, subsidence, or stem fracture, the bone loss due to stress shielding impairs the construction as a whole and can lead to inadequate support for a revision implant in the future [15].

Adaptive bone reactions around prostheses have been reported to stabilize after approximately a year post-operatively, but progressive late reactions have also been noted by others [23]. Kiratli *et al.* evaluated post-operative bone loss using DEXA and concluded that bone remodeling does not stabilize in two years. Rather, there is evidence of continued resorption between 2 and 5 years post-surgery and that bone loss progresses in small decrements not discernible by standard radiographs [24, 25]. Other assessments of bone loss over time are often inconclusive as early clinical studies of bone resorption relied on radiographic measurements that predated DEXA technology [23].

Analysis of typical roentgenographic data only provides a subjective impression of bone remodeling and does not allow true quantification of bone resorption [13]. Even quantitative computerized tomographic scanning and routine single- or dual-photon absorptiometry are non-specific and imprecise for the determination of changes in bone-mineral density about a metallic

prosthesis. As a consequence, the changes in bone resorption as reported in pre-DEXA studies were rarely differentiated beyond the second post-operative year [26].

Despite these data accuracy concerns, the study by Huiskes *et al.* [27] on stress shielding and bone resorption notes that even if the bone remodeling process does stop after a few years, a loss of proximal bone mass on the order of 50% "provides little confidence for the time when these patients get older and become prone to falls and other accidents as … the remaining bone may not be adequate to withstand the impact forces". As Huiskes noted in two subsequent studies on THA complications, that while "…the stress shielding scenario constitutes a potential failure mechanism", clinical failures are "hardly ever reported" [10, 28].

Despite this conclusion, a large body of research indicates that the loss of proximal support increases the risk of fatigue fracture of the stem and jeopardizes any future revision that would require extraction of an otherwise well-fixed stem [29, 30, 10, 31, 32]. Surgery of this type is a technically challenging procedure that may not leave adequate bone for satisfactory support of a revision implant [22]. Studies by Huiskes *et al.* [33], Nistor *et al*. [34], Bugbee *et al.* [35] and Weinans *et al*. [12] over 11 years have summarized that periprosthetic bone remodeling may contribute to increased mid-thigh pain or decreased function, fracture of the femur or the femoral component, loss of fixation of the implant, increased prevalence or severity of osteolysis and, again, difficulty in performing a revision.

The 1997 paper by Bugbee *et al.* [35] also concludes that "the prevalence of these adverse consequences has not been reported, to our knowledge". While such consequences are not widespread, the preservation of femoral bone stock is an important and desirable goal [22]. This is especially significant when considering that cementless implants are typically used in younger patients where the potential for revision during the patient's lifetime is high and the need to keep reconstructive options open is paramount [13, 36].

Additional clinical factors

Another continuing concern regarding cementless femoral hip stems is persistent thigh pain despite stable fixation [37, 38]. Significant thigh pain after implantation of a cementless prosthesis occurs in as many as 20% of arthroplasty patients, a problematic outcome as one of the clinical indications for performing THA in the first place is joint pain [36]. Although the etiology of thigh pain remains unclear, research suggests that it is attributable to excessive stem stiffness and the resulting modulus mismatch between implant and host bone [6, 36, 39]. In a small sample of patients with conventional hip stems, Cameron noted that the incidence of thigh pain was reported by 2 of 5 patients. In larger group of 48 patients, the incidence of thigh pain with a solid stem was 40% versus the incidence of 5% with a reduced-stiffness stem [40]. These results indicate that clinical concerns regarding excessive stem stiffness extend beyond proximal bone loss.

Over the past three decades, various implant features have been proposed as factors contributing to subsequent stress shielding. Among these are stem stiffness, implant geometry, stem material, ingrowth surface, and level of porous coating [11, 31, 22, 41, 42, 43, 44]. Canine studies have demonstrated that an effective means of promoting proximal load transfer and a reduction in stress shielding is to reduce the stiffness of the stem [41, 45, 13, 46]. Additionally, the study on the determinants of stress shielding by Sumner *et al.* [41] noted that other variables, including the presence, absence or placement of the porous coating, did not significantly affect the pattern of long-term bone remodeling.

The indication that stem stiffness, rather than porous coating level, plays a dominant role in affecting bone resorption was also confirmed in human studies [47, 48, 22]. In terms of quantification, Bobyn *et al.* [49] determined that the long-term femoral strain patterns can be

substantially altered by a 3- to 5-fold reduction in stem stiffness and that the greatest effect could be realized in the femoral shaft adjacent to the middle one-half of the stem.

Other work by Engh *et al.* [50] on the influence of stem size noted that the incidence of pronounced bone resorption occurs in at least 20% of cases and increases with stem size and the flexural rigidity of the implant. In their study of 411 cases of cementless THA, stems ≥ 13.5 mm in diameter showed 5 times the incidence of pronounced resorption as compared with stems ≤ 12.0 mm in diameter. In a separate study, Bobyn *et al.* concluded that **to reduce bone resorption, the implant should possess a bending stiffness of about one-half to one-third that of the host human femur** [13].

Bone density effects

Other biomechanical studies have shown that stress shielding is dependent upon the density of the host bone, as well as the flexural rigidity of the implant. Research by Carter *et al.* [51] on the compressive behavior of bone has shown that Young's modulus of either cortical or cancellous bone is proportional to the apparent bone density cubed and can be approximated by the relation:

$$E = E_c \, \dot{g}^{0.06} \, (\rho/\rho_c)^3$$

where E is the compressive modulus (MPa) of a bone specimen of apparent density ρ (g/cm^3) tested at a strain rate $\dot{g}$ (sec^{-1}) and E_c is the compressive modulus of cortical bone of apparent density ρ_c tested at a strain rate of 1.0 sec^{-1}. As human cortical bone has a Young's modulus E_c of approximately 22,100 MPa and an apparent density ρ_c of 1.8 g/cm^3, this equation reduces to:

$$E = 3740 \, \dot{g}^{0.06} \, \rho^3$$

While the physiological range of strain rate $\dot{g}$ is 0.002 to 0.01s^{-1} and the choice of strain rate is arbitrary, Young's modulus is relatively insensitive to variation in this parameter [47]. For this reason, Huskies *et al.* [27] used this equation and ignored the strain rate term in assessing the relationship between stress shielding and bone resorption. This relationship is significant in that Young's modulus can be determined given the cross-sectional density data from a CT scan and the flexural rigidity can be calculated given the corresponding bone geometry.

Beyond variations in bone mineral density, other factors that influence bone resorption include the cortical thickness of the femur receiving the stem [31, 52]. In a study of mechanical compatibility between prostheses and femoral bone, Dujovne *et al.* [39] concluded that resorptive bone remodeling is typically discussed solely in terms of implant stiffness and efforts to design more mechanically compatible stems have been "arbitrary" because these efforts have not considered or accounted for the stiffness characteristics of the host femur. Huiskes *et al.* similarly concluded that the **important causative factor for bone resorption is implant stiffness relative to bone stiffness, rather than implant stiffness in an absolute sense** [27].

Dujovne *et al.* [39] presented data on the axial and bending stiffness of 65 femora calculated from cross-sectional CT scans taken at 10 mm intervals along the longitudinal axis of each femur. These data were then compared to that of two commercially-available implant designs. Dujovne *et al.* note that while the commercial implants were as much as 2 times less stiff than the femur in the distal region, these same implants were 4 to 5 times stiffer than the bone in the proximal region. More significantly, the stems were always stiffer axially than the corresponding femur by as much as 10-30 times for all stem sizes. This is consistent with research by Sychterz *et al.* [52] which indicated that that axial bone rigidity, defined as the product of the modulus of elasticity, E, and cross-sectional area, A, rather than the flexural rigidity of the femur, was strongly correlated with bone loss. Bobyn *et al.* [49] in their canine

study of stem stiffness and bone resorption also observed that the greatest disparity in stem stiffness relative to the femur is axial, not in torsional or bending stiffness. While hollowing the cylindrical portion of a hip stem is an inefficient means of modifying bending stiffness, axial rigidity is effectively reduced as it is proportional to changes in cross-sectional area. In their evaluation of a hollow prosthesis, Gross *et al.* [5] emphasized the goal of "stiffness adjustment" by noting that the proximal 10 mm of the bone is most sensitive to changes in stem rigidity and could benefit most from an "optimization process". Bobyn *et al.* [13] also observed that proximal bone resorption would be attenuated if the stiffness of the proximal stem could be "appropriately adjusted" relative to that of the metaphysis. Dujovne *et al.* [39] add that while "mechanical compatibility" cannot be quantified, there needs to be some acceptable mechanical relationship between implant and femur in terms of stiffness parameters.

Bone-implant interface concerns

While excessive stem stiffness is potentially harmful, excessive flexibility can jeopardize fixation and stability at the bone-implant interface [53, 26]. As stem stiffness is reduced, shear stresses at the interface increase. These higher stresses can lead to proximal interface failure and the enhancement of relative interface motions if the implant becomes unbonded. This micromotion at the interface is one of the dominant causes of the long-term failure of total hip replacements [54, 10].

Micromotion between the surfaces of as little as 75μm has induced the development of a fibrous tissue layer at the bone-implant interface in some studies. Other researchers have noted the bone ingrowth occurred *in vivo* as long as micromotion did not exceed a range of 28-40 μm. [55]. Brunette *et al.* [61] note that the tolerated micromotion threshold is somewhere between 50 and 150 μm. These results suggest that any consistent relative motion at the interface that exceeds 50 μm may compromise implant fixation. The problem is not only how to minimize

stress shielding, but rather how to minimize bone resorption while keeping interface stresses and motions at an acceptable level [57, 1, 58, 13].

In a review by Bobyn *et al.* [13] of the dissertation by J. Miller on "The Paradox of Isoelasticity", he notes that "…flexible stems allow more bending of the femur, together with the implant, imposing higher shear displacement at the interfaces and potentially preventing bone ingrowth" and that "flexible implants deform more under load and are more susceptible to fatigue fracture". Harvey *et al.* [53] evaluated the effect of flexibility of the femoral stem and conclude that it is necessary to balance the competing objectives of minimum bone-remodeling and maximum fixation of the implant. In their review of stress analyses of hip prostheses, Joshi *et al.* [1] also note that research often focuses primarily on stress shielding and overlooks the increased proximal micromotion and interface shear stresses. These authors conclude that some combination of modified stem length and reduced stiffness is needed to achieve a satisfactory compromise between these competing objectives.

2.3 "Isoelasticity" and alternative designs

Early attempts to incorporate design features that reduce the flexural rigidity of the implant and minimize bone resorption due to stress shielding have led to inconsistent results and, in some cases, catastrophic failures [22, 10]. Researchers and implant manufacturers have developed, marketed and evaluated reduced-stiffness implants broadly characterized as "isoelastic" prostheses. Most of these isoelastic designs have involved changing material properties or modifying the structural characteristics to reduce the moment of inertia of the implant [39].

Studies by Morscher *et al.* [59], major proponents of this concept, suggested that "by adjusting the physical characteristics of the foreign material to that of the bone tissue" they

achieved an "optimum approximation of the physical characteristics of an implant to that of bone". As described by Andrew *et al*. [60], "…the concept of isoelasticity is that the implant and bone should deform as one unit. To achieve this, the stiffness of the cortical tube, and the femoral stem it surrounds, must be approximately matched, reducing relative movement between the bone and the femoral stem". While this perspective may have conceptual appeal, neither of these studies defined elasticity or stiffness in quantifiable terms [6].

The RM Isoelastic® stem (Mathys Ltd. Bettlach, Switzerland) was introduced in 1973 as one of the first commercial efforts aimed at achieving a more physiological loading of the femur. Polyacetyl resin was selected for the bulk of the femoral component because of its "tensile strength, durability and the proximity of its modulus to that of bone" with a stainless steel core to avoid "over-elasticity" in the neck region of the prosthesis [58]. An early evaluation by Morscher *et al.* [61] of the RM Isoelastic (RMI) implant focused on testing done to assure biocompatibility but offers little quantitative data regarding the stiffness of the implant. As noted in a subsequent report by Morscher *et al.* [59], because of the high incidence of loosening of the RMI implant, "reinforcement" of the prosthesis became necessary in 1977. Although no data were presented, these authors maintain that "much better results were obtained" as a consequence of this modification.

Initial clinical experience with the RMI implant was described by Bombelli *et al.* [62] but provided little detail other than to note that "…we have tested the fracture strength of the collar-neck portion experimentally and shown it to be double that of a steel prosthesis and four to five times greater than the strength of the bone itself. The plastic-metal combination is a little more elastic than pure metal… to allow for a certain amount of shock absorption".

The DEXA-based evaluation by Ang *et al.* [63] summarizes the encouraging short-term (≤ 1 year) results of the RMI stem and notes that loss of bone mass was "minor, recovering early,

in the flexible isoelastic implants". However, earlier assessments which lacked the accuracy of DEXA technology concluded that "while early results are encouraging, this prosthesis needs a longer follow-up evaluation to prove its effectiveness" [60, 64]. Niinimaki *et al.* [65] in their 7-9 year follow-up study, also acknowledged that while early results were encouraging, the RMI stem shows a high rate of loosening and the results are "worse than those reported for other uncemented stems". Matricali *et al.* [66] also evaluated the RMI prosthesis in 19 revision surgeries and reported that they had a "far less acceptable result" than that reported by others.

In a more recent report summarizing the use of the RMI on younger patients, Ali et al. [67] conclude that "we have concerns over the longer term survival of the prosthesis" due to its high incidence of lateral migration. In the longest study of the RMI implant, Trebse *et al.* [58] state that with a survival rate of 69% (10-year) and 48% (15-year), "it presents one of the worst performances reported for a cementless total hip replacement". Figure 2.1 provides visual indication of extent of the longer-term problems associated with the Mathys implant.

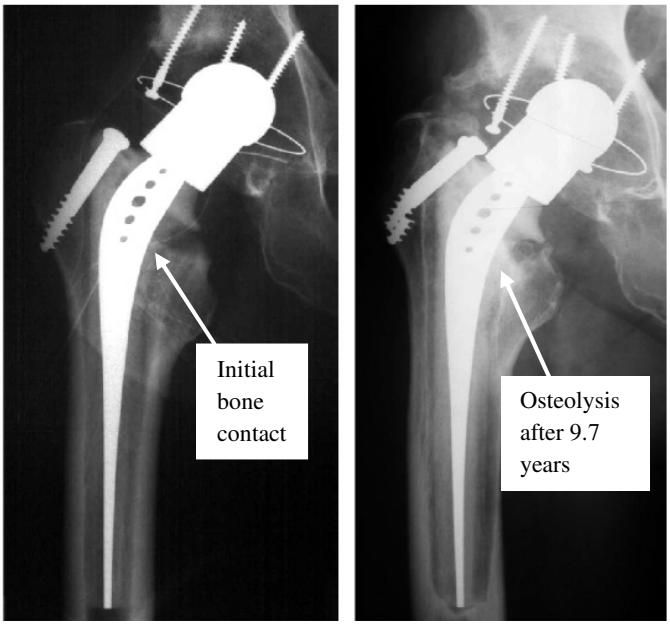

Figure 2.1: Images of the RM Isoelastic (RMI) implant. Adapted from [58].

As a result of this sub-standard clinical experience, the concept of isoelasticity became an example of failed innovation as described by Huiskes [10]. In another evaluation of the RMI prosthesis, Au [4] noted that the perceived advantage of isoelasticity "is hard to justify in clinical practice". The clinical review of this prosthesis by Jakim *et al.* [68] concluded that the concept of isoelasticity has failed to fulfill original clinical expectations and that "it seems unlikely that an ideal mimic can be fashioned from plastic materials".

Beyond the clinical complications associated with the RMI hip stem, the term "isoelastic' is misleading in that it suggests "equal elasticity". Bobyn *et al.* [13] suggested that it is more appropriate to seek to create an implant structure that is "physioelastic", to describe a post-operative condition in which the flexural rigidity and loading of the implant-bone composite approximates that of the unaltered femur.

Several researchers evaluated (or promoted) the adoption of a hollow-stemmed prosthesis as a means of achieving a more nearly "physioelastic" condition [5, 49]. The hollow Cenos (Artos Medizinische Produkte GmbH, Berlin, Germany) stem relies on extra flexibility to reduce stress shielding with "very satisfying" but unquantified results reported by Schmidt *et al.* [69] after 1 year of clinical experience.

Others have evaluated implant properties and stress distribution in the femur as a result of incorporating transverse holes or removing material from the proximal one-third of the stem [70, 71]. Effects of these modifications were inconclusive and influenced by other design or manufacturing issues.

Another hollow stem, the SHEP implant (Howmedica GmbH, Schönkirchen, Germany) as described by Täger [72] and shown in Figure 2.2, has holes along the length of the cobalt-chromium (CoCr) alloy stem and relies on the ingrowth of cancellous bone to fixate the implant.

Täger reports a 94% success rate for the use of the SHEP stem in at least 150 patients over a six-year period.

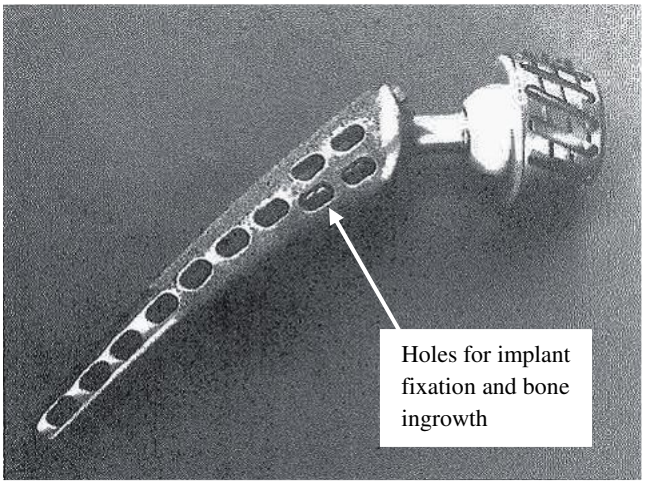

Figure 2.2: Image of the hollow Spongiosa-Hip joint-Endo-Prosthesis (SHEP). Adapted from [72].

Butel [73] developed and evaluated a nonrigid femoral implant that claimed to provide a unit comprised of bone and prosthesis that *together* (emphasis by Butel) would have similar elastic properties as bone. The Butel stem consisted of four metallic rods, joined at the distal end. In a review of 61 hips using this stem, Butel *et al.* do not include any quantitative analysis of the stem design or its effect on bone resorption. A subsequent clinical evaluation by Jacobsson *et al.* [74] noted that the flexible stem of the Butel femoral component produces high shear forces in the proximal interface which has led to loosening, overload on the prosthesis and fatigue fracture. With a failure rate of 43%, the Butel femoral prostheses were deemed a "clinical failure".

Another approach to the reduction of stem stiffness is inclusion of a slot in the distal stem, as in the S-ROM® stem (Joint Medical Products, Stamford, Connecticut). Cameron [40] evaluated the clinical performance of this stem, which is split distally to reduce bending stiffness. While his 3-6 year evaluation disclosed acceptable overall results and a significant reduction in

thigh pain, the effect of the slotted distal stem design does not address the problem of proximal implant stiffness, the zone in which the greatest mismatch in rigidity occurs [49].

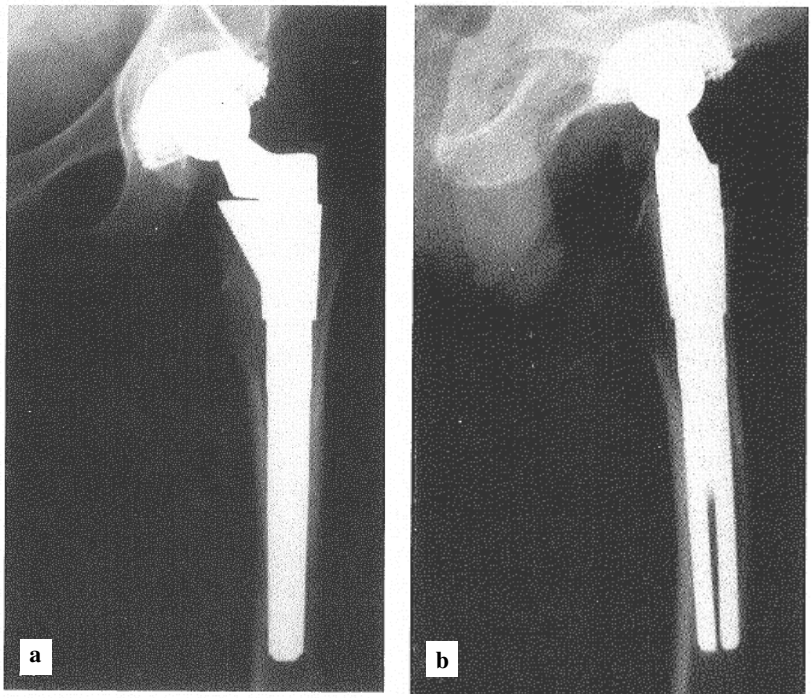

Figure 2.3: Images of the S-ROM prosthesis; **a**) coronal plane; **b**) sagittal plane. Adapted from [49].

Other methods of reducing femoral implant stiffness include the removal of metal from the outer surface of the component and replacement with a polymer to fill out the geometry of the prosthesis [37]. Clinical trials by Nistor *et al.* [34] of the LMPCH titanium stem (Biomet, Inc., Warsaw, Indiana), coated with a solid inner layer and porous outer layer of polyethylene, each 1.5 mm thick, were generally not successful due to implant subsidence. High rates of revision, mechanical failure (delamination) of the polymer coating and associated osteolysis led to the abandonment of the design [53].

Another composite material prosthesis is the Epoch® hip (Zimmer, Inc., Warsaw, Indiana). This current femoral stem design incorporates an inner metallic core, an outer porous

metal mesh of titanium (Ti) metal fibers with effective thickness of 0.83 mm and an intervening polymer layer of polyaryletherketone that has been injection-molded onto the CoCr core [30]. The clinical report by Akhavan *et al.* [75] noted that the proximal bending stiffness of the implant is "similar" to that of the proximal part of the femur and two to six times less than the bending stiffness of a comparatively sized Ti or CoCr alloy implant. The clinical study of the Epoch stem by Glassman *et al.* [37], showed stable initial fixation and minimal micromotion but the study was "too short to determine the long-term outcome of the procedure" relative to adaptive bone remodeling. The studies by Karrholm *et al.* [30] assessed longer-term performance of this implant design and noted that proximal bone resorption was less than with other uncemented stems.

Stiffness modification concepts

After reporting on the poor clinical results of the RMI stem, Niinimaki *et al.* [65] noted that "…the modulus of elasticity of the stem should perhaps be adjusted more accurately". Conclusions reached by Kuiper *et al.* [15] and Simões *et al.* [76] are similar, suggesting that the modulus of elasticity should vary along the prosthesis length, with a relatively high proximal-medial modulus and a low distal modulus, matching the cortical bone modulus at the prosthesis tip [77]. The finite element (FE) studies of a controlled-modulus prosthesis by Simões *et al.* [78] demonstrate that the desired load transfer distribution can be produced, minimizing both calcar stress shielding and interface micromotion. In a 2000 paper by Simões *et al*. [76], the authors note that **the development of a controlled-stiffness implant is limited by currently available materials and the fabrication process involved**. "At present, for the hip prosthesis, this remains a theoretical solution since it is difficult to manufacture a device with a very highly differentiated modulus". Bobyn *et al.* [13] concluded that only with the use of composite structures might it be possible to adequately address the stiffness mismatch for all stem sizes,

especially in the metaphysis. "Hopefully, the next decade will witness innovations in design and materials that will permit the realization of these objectives."

Glassman *et al.* [22] and Harvey *et al.* [53] also recognized the potential advantage of carbon fiber composites which offer a combination of high fatigue strength and elastic moduli closer to bone than that of metal alloys. These composite materials can be fabricated to be nonhomogeneous and nonisotropic such that the flexural rigidity can be varied within different implant regions [76]. Despite these perceived advantages, the clinical success of carbon fiber composite femoral implants has been limited by problems with stem fracture and inadequate fixation at the polymer-bone interface [37]. These composite implants lack the ability for osseointegration as they cannot be fabricated with conventional porous coatings or other bone ingrowth surfaces [22]. This practical complication leads research and development back to the use of metal alloys for an endoprosthesis.

There are distinct advantages in keeping the implant entirely metallic, including a proven history of use and FDA approval considerations [49]. Although implant manufacturers have long promoted the use of titanium alloy stems as a "less stiff" material, adequate consideration of the consequences of stem geometry has been lacking [6]. Glassman *et al.* [37] noted that the flexural advantage of using Ti is reduced with the larger stem sizes (>14 or 15 mm diameter) because of the dominant effect of stem geometry on stiffness. However, even with smaller stem sizes, the proximal femur is still understressed by at least 10-fold with a Ti implant when compared to the stresses in the intact femur [36].

As early as 1972, Lembert *et al.* [79] noted that if a prosthesis were made of a metallic material that was more compliant than solid metal, the "loads would be more evenly distributed and much, if not all, of the motion between the implant and bone would be overcome" [80]. While this predates recent concerns regarding micromotion at the bone-implant interface, the

concept of a more physiologically compatible implant was recognized four decades ago. Since then some implant designs have incorporated structural design features which (either intentionally or as a result of unrelated requirements) have reduced the stiffness of the implant. For example, Bobyn *et al.* observed that the flutes on the distal portion of the HG Multilock (Zimmer, Inc.) stem, which increase in depth with increasing stem size, provide an additional gain in flexibility of up to 25% with the larger stem sizes as compared to that of a solid, non-fluted stem [13].

Flexural rigidity and porosity

In their FE analysis of a cementless prosthesis, Tensi *et al.* [81] note that neither a very stiff implant nor an "isoelastic" one provides an ideal solution. "Probably anisotropic materials, such as unidirectional solidified metal alloys, are a possible solution". Kuiper *et al.* [15] in their study of the mathematical optimization of elastic properties arrived at a similar conclusion. "Reducing the stem stiffness decreases the amount of stress shielding and hence the amount of bone loss. However, this measure inevitably promotes higher proximal interface stresses and thereby increases the risk of proximal interface failure. The designer's task therefore is to optimize the stem stiffness in order to find the best compromise in the conflict. Yet, a better compromise might be found when the stem material was nonhomogeneous, in other words, when an arbitrary distribution of the elastic properties inside the stem was allowed". Mukherjee *et al.* [82] suggested "…a material optimization scheme via finite element with input of the right material properties and a technology to fabricate devices which will allow the devices to have different strength and modulus properties from the proximal to the distal end".

The success of prior efforts to implement this scheme has been limited by combination of biomaterial incompatibilities, practical manufacturing complications and insufficient understanding of flexural rigidity as it is applied to orthopaedic implants. With the recent development of additive manufacturing processes, including the laser sintering and electron beam

melting of biocompatible metallic powders, comes the potential to create closed cell porous materials as a practical means of reducing stem stiffness and tailoring the mechanical properties of the implant to clinical requirements.

2.4 References

[1] Joshi, M.G., Santare, M.H., Advani, S.G., *Survey of stress analyses of the femoral hip prosthesis*, ASME Applied Mechanical Review, Vol. 53, No. 1, pp. 1-18, 2000.

[2] Gruen, T.A., McNeice, G.M., Amstutz, H.C., *"Modes of Failure" of Cemented Stem-type Femoral Components*, Clinical Orthopaedics and Related Research, Vol. 141, pp. 17-27, 1979.

[3] Engh, C.A., Claus, A.M., Hopper, R.H., Engh, C.A., *Long-Term Results Using Anatomic Medullary Locking Hip Prosthesis,* Clinical Orthopaedics and Related Research, Vol. 393, pp. 137-146, 2001.

[4] Au, M.K., *Isoelastic Total Hip Replacement: Critical Evaluation of Prosthetic Isoelasticity*, Journal of the Formosan Medical Association, Vol. 93, No. 6, pp. 497-502, 1994.

[5] Gross, S., Abel, E.W., *A finite element analysis of hollow stemmed hip prostheses as a means of reducing stress shielding of the femur*, Journal of Biomechanics, Vol. 34, pp. 995-1003, 2001.

[6] Skinner, H.B., *Isoelasticity and Total Hip Arthroplasty*, Orthopedics, Vol. 14, No. 3, pp. 323-328, 1991.

[7] Wan, Z., Dorr, L.D., Woodsome, T., Ranawat, A., Song, M., *Effect of Stem Stiffness and Bone Stiffness on Bone Remodeling in Cemented Total Hip Replacement*, The Journal of Arthroplasty, Vol. 14, No. 2, pp. 149-158, 1999.

[8] Weinans, H., Huiskes, R., van Rietbergen, B., Sumner, D., Turner, T., Galante, J., *Adaptive Bone Remodeling Around Bonded Noncemented Total Hip Arthroplasty: A Comparison between Animal Experiments and Computer Simulation*, Journal of Orthopaedic Research, Vol. 11, No. 4, pp. 500-513, 1993.

[9] Joshi, M.G., et al., *Analysis of femoral hip prosthesis designed to reduce stress shielding*, Journal of Biomechanics, Vol. 33, pp. 1655-1662, 2000.

[10] Huiskes, R., *Failed innovation in total hip replacement: Diagnosis and proposals for a cure*, Acta Orthopaedica Scandinavica, Vol. 64, No. 6, pp. 699-716, 1993.

[11] Engh, C.A., O'Connor, D., Jasty, M., McGovern, T.F., Bobyn, J.D., Harris, W.H., *Quantification of Implant Micromotion, Strain Shielding and Bone Resorption With Porous-Coated Anatomic Medullary Locking Femoral Prostheses*, Clinical Orthopaedics and Related Research, Vol. 285, pp. 13-29, 1992.

[12] Weinans, H., Sumner, D., Igloria, R., Natarajan, R., *Sensitivity of periprosthetic stress-shielding to load and the bone density-modulus relationship in subject-specific finite element models*, Journal of Biomechanics, Vol. 33, pp. 809-817, 2000.

[13] Bobyn, Mortimer, Glassman, Engh, et al., *Producing and Avoiding Stress Shielding*, Clinical Orthopaedics and Related Research, Vol. 274, pp. 79-96, 1992

[14] Jacobs, C.R., *The mechanobiology of cancellous bone structural adaptation*, Journal of Rehabilitation Research and Development, Vol. 37, No. 2, pp. 209-216, 2000.

[15] Kuiper, J.H., Huiskes, R., *Mathematical Optimization of Elastic Properties: Application to Cementless Hip Stem Design*, Journal of Biomechanical Engineering, Vol. 119, No. 2, pp. 166-174, 1997.

[16] Huiskes, R., Nunamaker, D., *Local Stresses and Bone Adaption Around Orthopedic Implants*, Calcified Tissue International, Vol. 36, pp. S110-S117, 1984.

[17] Kilgus, D.J., Shimaoka, E.E., Tipton, J.S., Eberle, R.W., *Dual-Energy X-Ray Absorptiometry Measurement of Bone Mineral Density around Porous-Coated Cementless Femoral Implants*, Journal of Bone & Joint Surgery (Br), Vol. 75-B, No. 2, pp. 279-287, 1993.

[18] Sychterz, C.J., Engh, C.A., *The Influence of Clinical Factors on Periprosthetic Bone Remodeling*, Clinical Orthopaedics and Related Research, Vol. 322, pp. 285-292, 1996.

[19] Lewis, J.L., Askew, M.J., Wixson, R.L. et al., *The Influence of Prosthetic Stem Stiffness and of a Calcar Collar on Stresses in the Proximal End of the Femur with a Cemented Femoral Component*, Journal of Bone and Joint Surgery, Vol. 66-A, No. 2, pp. 280-286, 1984.

[20] Bauer, T.W., Schils, J., The *pathology of total joint arthroplasty: II. Mechanisms of implant failure*, Skeletal Radiology, Vol. 28, No. 9, pp. 483-497, 1999.

[21] Engh, C.A., McGovern, T.F., Bobyn, J.D., Harris, W.H., *A Quantitative Evaluation of Periprosthetic Bone-Remodeling After Cementless Total Hip Arthroplasty*, Journal of Bone and Joint Surgery, Vol. 74, No. 7, pp. 1009-1020, 1992.

[22] Glassman, A., Bobyn, J., Tanzer, M., *New Femoral Designs: Do They Influence Stress Shielding?, Clinical Orthopaedics and Related Research, Vol. 453, pp. 64-74, 2006.*

[23] Huiskes, R., Weinans, H., Grootenboer, H.J., et al., *Adaptive Bone-Remodeling Theory Applied to Prosthetic-Design Analysis*, Journal of Biomechanics, Vol. 20, No. 11/12, pp. 1135-1150, 1987.

[24] Van Rietbergen, B., Huiskes, R., Weinans, H., et al., *The Mechanism of Bone Remodeling and Resorption Around Press-Fitted THA Stems*, Journal of Biomechanics, Vol. 26, No. 4/5, pp. 369-382, 1993.

[25] Kiratli, B.J., Heiner, J.P., McBeath, A.A., Wilson, M.A., *Determination of BMD by Dual X-Ray Absorptiometry in Patients with Uncemented Total Hip Arthroplasty*, Journal of Orthopaedic Research, Vol. 10, No. 6, pp. 836-844, 1992.

[26] Engh, C.A., Bobyn, J.D., *The Influence of Stem Size and Extent of Porous Coating on Femoral Bone Resorption after Primary Cementless Hip Arthroplasty*, Clinical Orthopaedics and Related Research, Vol. 231, pp. 7-28, 1988.

[27] Huiskes, R., Weinans, H., Van Rietbergen, B., *The Relationship Between Stress Shielding and Bone Resorption Around Total Hip Stems and the Effects of Flexible Materials*, Clinical Orthopaedics and Related Research, Vol. 274, pp. 124-134, 1992.

[28] Huiskes, R., *Stress Shielding and Bone Resorption in THA: Clinical Versus Computer-Simulation Studies*, Acta Orthopaedica Belgica, Vol. 59, Suppl. 1, pp. 118-129, 1993.

[29] Brown, I.W., Ring, P.A., *Osteolytic Changes in the Upper Femoral Shaft Following Porous-Coated Hip Replacement*, Journal of Bone & Joint Surgery (Br), Vol. 67-B, No. 2, pp. 218-221, 1985.

[30] Karrholm, J., Anderberg, C., Snorrason, F., et al., *Evaluation of a Femoral Stem with Reduced Stiffness*, Journal of Bone and Joint Surgery, Vol. 84-A, No. 9, pp. 1651-1658, 2002.

[31] Engh, C.A. Jr., Sychterz, C., Engh, C. Sr., *Factors Affecting Femoral Bone Remodeling After Cementless Total Hip Arthroplasty*, The Journal of Arthroplasty, Vol. 14, No. 5, pp. 637-644, 1999.

[32] Engh, C.A., Young, A.M., Engh, C.A. Sr., Hopper, R.H., *Clinical Consequences of Stress Shielding After Porous-Coated Total Hip Arthroplasty*, Clinical Orthopaedics and Related Research, Vol. 417, pp. 157-163, 2003.

[33] Huiskes, R., Boeklagen, R., *Mathematical Shape Optimization of Hip Prosthesis Design*, Journal of Biomechanics, Vol. 22, No. 8/9, pp. 793-804, 1989.

[34] Nistor, L., Blaha, J.D., et al., *In Vivo Measurements of Relative Motion between an Uncemented Femoral Total Hip Component and the Femur by Roentgen Stereophotogrammetric Analysis*, Clinical Orthopaedics and Related Research, Vol. 269, pp. 220-227, 1991.

[35] Bugbee, W.D., Culpepper, W.J., Engh, C.A. Jr., Engh C.A. Sr., *Long-Term Clinical Consequences of Stress-Shielding after Total Hip Arthroplasty without Cement*, Journal of Bone and Joint Surgery, Vol. 79, No. 7, pp. 1007-1012, 1997.

[36] Namba, R.S., Keyak, J.H., Kim, A.S. et al., *Cementless Implant Composition and Femoral Stress*, Clinical Orthopaedics and Related Research, Vol. 347, pp. 261-267, 1998.

[37] Glassman, A.H., Crowninshield, R.D., Schenck, R., Herberts, P., *A Low Stiffness Composite Biologically Fixed Prosthesis*, Clinical Orthopaedics and Related Research, Vol. 393, pp. 128-135, 2001.

[38] Skinner, H.B., Curlin, F.J., *Decreased Pain with Lower Flexural Rigidity of Uncemented Femoral Prostheses*, Orthopedics, Vol. 13, No. 11, pp. 1223-1228, 1990.

[39] Dujovne, A R., Bobyn, J D., Krygier, J. J., Miller, J E., Brooks, C E., *Mechanical Compatibility of Noncemented Hip Prostheses with the Human Femur*, The Journal of Arthroplasty, Vol. 8, No. 1, pp. 7-22, 1993.

[40] Cameron, H.U., *The 3-6 Year Results of a Modular Noncemented Low-bending Stiffness Hip Implant*, Journal of Arthroplasty, Vol. 8, No. 3, pp. 239-243, 1993.

[41] Sumner, D.R., Galante, J.O., *Determinants of Stress Shielding: Design Versus Materials Versus Interface*, Clinical Orthopaedics and Related Research, Vol. 274, pp. 202-212, 1992.

[42] Huo, M.H., Brown, B.S., *What's New in Hip Arthroplasty?*, Journal of Bone and Joint Surgery, Vol. 85-A, No. 9, pp. 1852-1866, 2003.

[43] Keaveny, T.M., Bartel, D.L., *Effects of Porous Coating and Collar Support on Early Load Transfer for a Cementless Hip Prosthesis*, Journal of Biomechanics, Vol. 26, No. 10, pp. 1205-1216, 1993.

[44] Keaveny, T.M., Bartel, D.L., *Effects of Porous Coating, with and without Collar Support, on Early Relative Motion for a Cementless Hip Prosthesis*, Journal of Biomechanics, Vol. 26, No. 12, pp.1355-1368, 1993.

[45] Maistrelli, G.L., Fornasier, V., Binnington, A., et al., *Effect of Stem Modulus in a Total Hip Arthroplasty Model*, Journal of Bone and Joint Surgery (Br), Vol. 73-B, pp. 43-46, 1991.

[46] Turner, T.M., Sumner, D.R., Urban, R.M., Igloria, R., Galante, J.O., *Maintenance of Proximal Cortical Bone with Use of a Less Stiff Femoral Component in Hemiarthroplasty of the Hip without Cement*, Journal of Bone and Joint Surgery, Vol. 79-A, No. 9, pp. 1381-1390, 1997.

[47] Skinner, H.B., Kilgus, D.J., Keyak, J., et al., *Correlation of Computed Finite Element Stresses to Bone Density after Remodeling around Cementless Femoral Implants*, Clinical Orthopaedics and Related Research, Vol.305, pp. 178-179, 1994.

[48] McAuley, J.P., Sychterz, C.J., Engh, C.A., *Influence of Porous Coating Level on Proximal Femoral Remodeling*, Clinical Orthopaedics and Related Research, Vol. 371, pp. 146-153, 2000.

[49] Bobyn, J., Glassman, A., Goto, H., Krygier, J., et al., *The Effect of Stem Stiffness on Femoral Bone Resorption after Canine Porous-coated Total Hip Arthroplasty*, Clinical Orthopaedics and Related Research, Vol. 261, pp. 196-213, 1990.

[50] Engh, C.A., Bobyn, J.D., Glassman, A.H., *Porous-coated Hip Replacement: The Factors Governing Bone Ingrowth, Stress Shielding, and Clinical Results*, Journal of Bone & Joint Surgery (Br), Vol. 69-B, No. 1, pp. 45-55, 1987.

[51] Carter, D.R., Hayes, W.C., *The Compressive Behavior of Bone as a Two-Phase Porous Structure*, The Journal of Bone and Joint Surgery, Vol. 59-A, No. 7, pp. 954-962, 1977.

[52] Sychterz, C.J., Topoleski, L.D.T., Sacco, M., Engh, C.A. Sr., *Effect of Femoral Stiffness on Bone Remodeling After Uncemented Arthroplasty*, Clinical Orthopaedics and Related Research, Vol. 389, pp. 218-227, 2001.

[53] Harvey, E.J., Bobyn, J.D., Tanzer, M. et al., *Effect of Flexibility of the Femoral Stem on Bone-Remodeling and Fixation of the Stem in a Canine Total Hip Arthroplasty Model without Cement*, Journal of Bone and Joint Surgery, Vol. 81-A, No. 1, pp. 93-107, 1999.

[54] Simões, J.A., Monteiro, J., Vaz, M.A., *Numerical-Experimental Method for the Validation of a Controlled Stiffness Femoral Prosthesis*, Journal of Biomechanical Engineering, Vol. 123, pp. 234-238, 2001.

[55] Kienapfel, H., Sprey, C., Wilke, A., Griss, P., *Implant Fixation by Bone Ingrowth*, Journal of Arthroplasty, Vol. 14, pp. 355-368, 1999.

[56] Brunette, D.M., Chehroudi, B., *The effects of the surface topography of micromachined titanium substrata on cell behavior in vitro and in vivo*, Journal of Biomechanical Engineering, Vol. 121, pp. 49-57, 1999.

[57] Kowalczyk, P., *Design Optimization of Cementless Femoral Hip Prostheses Using Finite Element Analysis*, Journal of Biomechanical Engineering, Vol. 123, pp. 396-402, 2001.

[58] Trebse, R., Milosev, I., Kovac, S., Milek, M., Pisot, V., *Poor results from the isoelastic total hip replacement: 14-17 year follow-up of 149 cementless prostheses*, Acta Orthopaedica, Vol. 76, No. 2, pp. 169-176, 2005.

[59] Morscher, E.W., Dick, W., *Cementless Fixation of "Isoelastic" Hip Endoprostheses Manufactured from Plastic Materials*, Clinical Orthopaedics and Related Research, Vol. 176, pp. 77-87, 1983.

[60] Andrew, T., Flanagan, J., Gerundini, M., Bombelli, R., *The Isoelastic, Noncemented Total Hip Arthroplasty: Preliminary Experience with 400 Cases*, Clinical Orthopaedics and Related Research, Vol. 206, pp. 127-138, 1986.

[61] Morscher, E. Bombelli, R. Schenk, R. Mathys, R., *The Treatment of Femoral Neck Fractures with an Isoelastic Endoprosthesis Implanted Without Bone Cement*, Archives of Orthopaedic and Trauma Surgery, Vol. 98, No. 2, pp. 93-100, 1981.

[62] Bombelli, R., Mathys, R., *Cementless isoelastic RM total hip prosthesis*, Journal of the Royal Society of Medicine, Vol. 75, pp. 588-597, 1982.

[63] Ang, K. C., Das De, S., Goh, J. C. H., *Periprosthetic Bone Remodeling After Cementless Total Hip Replacement*, Journal of Bone & Joint Surgery (Br), Vol. 79-B, pp. 675-679, 1997.

[64] Museru, L.M., Tay, B. K., Balachandran, N., *Isoelastic Cementless Total Hip Replacement Preliminary Results of 24 Replacements*, Singapore Medical Journal, Vol. 29, No. 4, pp. 361-366, 1988.

[65] Niinimaki, T. J., Puranen, J.P., Jalovaara, P K., *Total Hip Arthroplasty Using Isoelastic Femoral Stems: A Seven- to Nine-Year Follow-Up in 108 Patients*, Journal of Bone & Joint Surgery (Br), Vol. 76-B, pp. 413-418, 1994.

[66] Matricali, G A. Thibaut, H. Hendrickx, M. Thibaut, R., *Revision of Total Hip Arthroplasty Using the R.M. Isoelastic Prosthesis*, Acta Orthopaedica Belgica, Vol.59, Suppl. 1, pp. 374-376, 1993.

[67] Ali, M.S., Kumar, A., *Isoelastic femoral component in primary cementless total hip arthroplasty*, International Orthopaedics, Vol. 26, pp. 243-246, 2002.

[68] Jakim, I., Barlin, C., Sweet, M.B.E., *RM Isoelastic Total Hip Arthroplasty: A Review of 34 Cases*, Journal of Arthroplasty, Vol. 3, No. 3, pp. 191-199, 1988.

[69] Schmidt, J., Hackenbroch, M. H., *The Cenos hollow stem in total hip arthroplasty: first experiences in a prospective study*, Archives of Orthopaedic and Trauma Surgery, Vol. 113, No. 3, pp. 117-120, 1994.

[70] Viceconti, M., Toni, A., Giunti, A., *Effects of some technological aspects on the fatigue strength of a cementless hip stem*, Journal of Biomedical Materials Research, Vol. 29, pp. 875-881,. 1995.

[71] Engelhardt, J.A., Saha, S., *Effect of femoral component section modulus on the stress distribution in the proximal human femur*, Medical & Biological Engineering & Computing, Vol. 26, pp. 38-45, 1988.

[72] Täger, K.H., *The New Spongiosa-Hip-Joint-Endoprosthesis (SHEP)*, Acta Ortopaedica Belgica, Vol. 59, Suppl. 1, pp. 351-353, 1993.

[73] Butel, J. Robb, J E., *The isoelastic hip prosthesis followed for 5 years*, Acta Orthopaedica Scandinavica, Vol. 59, No. 3, pp. 258-262, 1988.

[74] Jacobsson, S-A., Djerf, K., Gillquist, J., et al., *A Prospective Comparison of Butel and PCA Hip Arthroplasty*, Journal of Bone & Joint Surgery (Br), Vol. 75-B, pp. 624-629, 1993.

[75] Akhavan, S., Matthiesen, M., Schulte, L., et al., *Clinical and Histologic Results Related to a Low-modulus Composite Total Hip Replacement Stem*, Journal of Bone and Joint Surgery, Vol. 88-A, No. 6, pp. 1308-1314, 2006.

[76] Simões, J.A., Marques, A.T., Jeronimidis, G., *Design of a controlled-stiffness composite proximal femoral prosthesis*, Composites Science and Technology, Vol. 60, pp. 559-567, 2000.

[77] Hollister, S.J., Fyhrie, D.P., Jepsen, K.J., Goldstein, S.A., *Application of Homogenization Theory to the Study of Trabecular Bone Mechanics*, Journal of Biomechanics, Vol. 24, No. 9, pp. 825-839, 1991.

[78] Simões, J.A.O., Taylor, M., Marques, A.T., Jeronimidis, G., *Preliminary investigation of a novel controlled stiffness proximal femoral prosthesis*, Proceedings of the Institution of Mechanical Engineers, Vol. 212, Part H, pp. 165-175, 1998.

[79] Spector, M., *Chapter 19: Low Modulus Porous Systems*, Non-Cemented Total Hip Arthroplasty, edited by R. Fitzgerald, Raven Press, Ltd., New York, NY, pp. 227-241, 1988.

[80] Lembert, E. Galante, J., Rostoker, W., *Fixation of Skeletal Replacement by Fiber Metal Composites*, Clinical Orthopaedics and Related Research, Vol. 87, pp. 303-310, 1972.

[81] Tensi, H.M., Gese, H., Ascherl, R., *Non-linear three-dimensional finite element analysis of a cementless hip endoprosthesis*, Proceedings of the Institution of Mechanical Engineers: Journal of Engineering in Medicine, Vol. 203, Part H, pp. 215-222, 1989.

[82] Mukherjee, D., Saha, S., *The Application of New Composite Materials for Total Joint Arthroplasty*, Journal of Long-Term Effects of Medical Implants, Vol. 3, No. 2, pp. 131-141, 1993.

3. Review of porosity-mechanical property relationships

In a study by Ryan *et al.* [1], the authors noted that while the use of titanium (Ti) in implants reduces the extent of stress shielding as compared to that of cobalt-chromium (CoCr), the stiffness mismatch is still substantial. To overcome this mismatch, Ryan *et al.* suggest the use of porous materials in implants. Their work and that of Li *et al.* [2] note that **mechanical properties of porous materials can be altered and optimized by controlling pore size and shape as well as pore distribution**. This is a useful perspective as long as relationships between the porous structure and the resulting mechanical properties are known.

As it is time- and cost-prohibitive to determine the effective mechanical properties of each porous material experimentally, semi-analytical and theoretical relationships have been proposed to describe the dependence of mechanical properties on porosity. The physical meaning of these relationships is often unclear as most theoretical models are based on some idealized physical microstructure (e.g., uniform cubic, cylindrical or spherical pores arranged in a cubic array), and the resulting correlations often cannot be extended to real materials and potential clinical applications [3].

The majority of the theoretical equations for moduli have been derived by treating a representative volume of a porous solid as a special case of two-phase materials, evaluating them mathematically or empirically, and extending the conclusions to the continuum material [4]. In his comparative review of these equations, Ramakrishnan [5] noted that all of these methods involve two steps: to establish the stress and strain distributions for a simple two-phase geometry and then to modify the distributions, taking into account the interaction between the inclusion phases.

O'Kelly *et al.* [6] characterize these theoretical methods into three main approaches: composite theory, cellular solids and minimum solid area (MSA). "The first approach assumes a two-phase material, with one phase having zero stiffness; the latter two assume a single phase permeated with voids". Herakovich *et al.* [7] take a broader view and observe that there are two fundamentally different approaches to the study of porous media: those of the mechanics community and those of the materials community. The mechanics community has tended to consider a specific shape pore (often spherical) and then develop analytical solutions for mechanical properties as a function of pore volume fraction. In contrast, the materials community has tended to obtain experimental results for mechanical properties as a function of porosity and then find the "best-fit" curve where the parameters are associated with the pore geometry or method of fabrication. These different approaches yield divergent results and, in certain instances, formulas which are sometimes in direct contradiction [8].

3.1 Linear equations

Dewey [9] derived the elastic constants of materials containing non-rigid fillers using a method first applied by Einstein to the calculation of the viscosity of a fluid loaded with small, rigid spheres. Per Rice [10], algebraic errors in Dewey's analysis preclude its accurate use in the as-published form. However, others conclude that her basic derivation is valid for low porosities, leading to the equation:

$$E_p = E_0 (1 - aP) \tag{1}$$

where E_p is Young's modulus of the porous body, E_0 is the modulus of a non-porous body of the same material, a is a constant dependent upon the nature of the pores, and P is the volume porosity.

Fryxell *et al.* [11] compared their experimental results for sintered beryllium oxide and found that the Dewey equation "describes the data well enough for most practical purposes", at least up to about 17% porosity. In their study of glass with spherical inclusions, Hasselman *et al.* [12] demonstrated the validity of the Dewey equation up to 2.5% porosity and derived a theoretical value for the constant a as function of v_0, the Poisson's ratio of the nonporous material:

$$a = 3(9+5v_0)(1-v_0)/2(7-5v_0) \quad (2)$$

Their empirical data showed that "good [visual] agreement between theory and experiment existed". Rossi [13] later derived the same relationship for the parameter a and expanded the theoretical applicability of the Dewey equation up to 10% porosity but cautioned that his approach is "nonrigorous and is intended only as an engineering solution to the problem" of predicting the elastic moduli of porous constructs.

3.2 Power relationships

Bert [14] expanded Rossi's work to include stress concentration factors for different void geometries and added an exponent for the maximum porosity possible, Q, given a specific pore arrangement:

$$E_p = E_0 [1-(P/Q)]^{KQ} \quad (3)$$

where $$K = 0.75 +(1.25b/c) \quad (4)$$

In this equation, c is the void length parallel to the loading direction and b is the void width perpendicular to the loading direction. Bert maintains that when applied to solids with spherical pores, his equation (3) is more accurate than existing equations up to 20% porosity.

Along with Dewey, MacKenzie [15] was one of few who studied the elastic properties of porous solids using spherical inclusions, assuming that the real material is homogeneous and isotropic and contains isolated voids distributed at random throughout the volume of the material. Chung [16] expands on this and notes that MacKenzie's analyses assumed that all of the pores were spherical and of the same size. Per Chung and Wagh *et al.* [17], MacKenzie's semi-empirical equation has the form:

$$E_p = E_0 (1-dP+gP^2) \tag{5}$$

where the constants d and g are slope constants "which depend upon the shape and concentration of the pores, assuming that all of the pores are closed pores." Chung notes one of the problems with this equation as "the significance of the slope constants… is somewhat difficult to comprehend, but may be related to the distribution of stress around the pores." A 1963 paper by Spinner *et al*. [18] confirmed the validity of this equation for polycrystalline thoria with porosity up to 40%. Although the MacKenzie equation (5) includes an exponent, at low porosities, "the range of interest in most practical applications", this relationship is equivalent to the linear Dewey equation (1) [18].

In a study of sintered copper, Bal'shin [19] concluded that the strength of a brittle porous specimen can be described with an equation of the form:

$$S_p = S_0 (1-P)^h \tag{6}$$

where S_p is the fracture strength of the porous body, S_0 is the strength of the non-porous material, h is an empirical constant, and P is specimen porosity. Bal'shin also noted that the value of the constant h ranged from 6 to 3 depending on the "characteristics" of the original material and the time and temperature of sintering but did not include data on the variation of the value of h [20].

In evaluating the properties of sintered ferrous alloys with porosities up to 40%, McAdam [21] determined that his empirical data for Young's modulus fit an equation of the same form:

$$E_p = E_0 (1\text{-}jP)^i \qquad (7)$$

with the value of the empirically-determined exponent, *i*, equal to 3.4 and *j* equal to 1.

Phani *et al.* [22, 23, 24, 25, 26] also compared empirical results for porous materials, including thoria, uranium dioxide, gypsum, alumina and silicon nitride, to the value of Young's modulus predicted by this equation. These authors concluded that the value of *i* "possibly lies between 2 and 3 for a relatively ordered and less open pore structures", such as closed spherical pores. In their research, the constant *j* is the reciprocal of the critical porosity, the porosity at which the structure becomes unstable and Young's modulus goes to zero. Phani *et al.* maintains that changes in the value of *i* for different materials can only be attributed to inherent differences in their structures and the value of *i* increases as the pores depart from being spherical and become more interconnected. These authors add that the value of *i* depends on "pore geometry, grain size and the interconnection of grains" and the resulting equation is valid up to at least 40% porosity. Wagh *et al.* [17] in their studies of the fracture and mechanical properties of ceramics arrived at similar conclusions, adding that the exponent *i* depends on the "tortuosity of the [pore] structure" [27]. Maitra *et al.* [28] extended the earlier work of Phani and concluded that *i* equals 2 for closed spherical pores, *i* equals 4 for a random orientation of pores, and supports these conclusions with data on the effective moduli for 12 polycrystalline materials.

Others have correlated the value of the exponent *i* to the type and extent of stress concentrations that develop around pores [29]. Ji *et al.* [3] proposed a similar equation which describes the mechanical properties of porous materials so long as the value of the exponent, which depends on the "geometrical shape, spatial arrangement, orientation and size distribution of

pores", can be determined from experimental data. Accordingly, this limits any predictive capability, except by comparison to previous empirical determinations. In most cases, these data are obtained graphically and values for *i* are fit visually [7].

3.3 Exponential equations

One of the most widely used equations to describe the effects of porosity on mechanical properties [25, 3] is based on the studies by Ryshkewitch [53] showing that strength varies logarithmically with porosity in sintered alumina. Duckworth [30] generalized this relationship as:

$$S_p = S_0 \, exp(-kP) \tag{8}$$

with *k* as a material-dependent constant and other variables as defined previously. He noted that *k* "has a value of about 7 for all experimental data on hand…[it] also appears to be independent of pore size" but this equation is only valid up to "about 50%" porosity. Knudsen [20] also noted that the Ryshkewitch equation (8) is "very similar to the relation proposed by Bal'shin" (6) for slight alterations in the ratio of *k* to *h*. His research assumed that strength was proportional to the contact or load-bearing area for different grain packing arrangements and showed that strength could be expressed by this exponential relationship with values of *k* ranging from 6 to 9 for different structures [10].

In later studies on aluminum oxide, Spriggs [31] extended the Duckworth/Ryshkewitch equation (8) to the effect of porosity on the modulus of elasticity. His research indicated that a valid equation for the determination of Young's modulus is similar:

$$E_p = E_0 \, exp(-mP) \tag{9}$$

and presented supporting data with the value of *m* varying from 2.7 to 4.3 for porosity values ranging from 0 to 37%, results consistent with later work by Knudsen [32]. While deviation from calculated values for Young's modulus became significant once porosity exceeded 17%, Spriggs demonstrated that the constant *m* depends upon differences in processing techniques, and "perhaps the type of materials and method of modulus measurement".

This suggests that there is a connection between effective moduli, pore shape and volume fraction, as well as fabrication method [7]. However, this equation does not satisfy the boundary condition that E_p should equal zero when P is equal to 1, the condition that exists when the matrix material is completely displaced by the voids in the material. Consequently, this equation is not valid over the full range of porosity. As noted by Hasselman [33], "not satisfying the boundary conditions will affect the actual values of E_p and m obtained from the experimental data" and "any conclusions based on the result obtained from the Spriggs equation cannot be regarded as entirely valid." Work by Phani *et al.* [26] confirmed that this relationship shows large disagreement with experimental data at higher porosities (P > 60%). Despite that limitation, a study by Herakovich *et al.* [7] on the effect of pore geometry on elastic properties noted that this relationship provides a "good approximation for effective properties up to 40% porosity."

Because of boundary condition issues with the Spriggs equation (9), Hasselman [33] proposed a general relationship based on work done by Hashin [8] by setting the properties of the second phase equal to zero. If voids are considered to be the dispersed phase, Hashin's general equation can be written in simplified form as:

$$E_p = E_0 \, (1+[AP/(1-AP-P)]) \qquad (10)$$

where the factor *A* is determined statistically from the experimental data. Hasselman states that the advantage of this proposed equation is that it can be used by selecting a value for the constant *A* appropriate for any porosity interval.

Wang [34] later confirmed that the Hashin-Hasselman equation (10) is valid for isolated closed pores up to about 20% porosity. To extend its applicability, Wang [35] proposed a variation on the Spriggs relationship:

$$E_p = E_0 \, exp[-(nP+qP^2)] \qquad (11)$$

where *n* and *q* are "nonnegative numbers dictated by the shape of the theoretical curves". Wang presents data that suggest that this relationship is applicable to both open and closed pores over a wider porosity range, up to 30% porosity. Research by Panakkal *et al.* [36] confirmed the validity of this equation for predicting Young's modulus of sintered iron up to 22% porosity. For higher porosities, Wang [35] suggested the inclusion of additional higher-order terms in the exponent. Phani [22] notes that the use of such equations becomes cumbersome and the material constants lose their physical significance. It may be argued that, irrespective of the equation, the physical significance of any of these terms is difficult to perceive. Because neither the Spriggs (9) nor the Wang equation (11) satisfy the boundary condition that E_p is equal to zero at 100% porosity, use of these equations to evaluate elastic moduli by extrapolation from fitted experimental data often results in large discrepancies (~one order of magnitude) between the extrapolated and observed values [28].

While Rice [10] acknowledges the mathematical limitations inherent in the Spriggs equation (9) noted by Hasselman and others, he considers this criticism misplaced because different pore or particle packing arrangements result in a critical porosity (i.e., the transition from isolated and closed to an open and interconnected porous structure), and thus complete loss

of strength, well before 100% porosity is attained. Thus, the fact that the Spriggs equation (9) does not satisfy the boundary conditions makes this mathematical requirement moot. For simple cubic stacking of pores, the critical porosity occurs when $P \geq 0.52$. For other arrangements of spherical pores, as shown in Figure 2.1, this transition from closed cells to an interconnected structure occurs at different porosity levels. For orthorhombic stacking, the critical porosity value is $P \geq 0.60$; for a rhombohedral pore structure, the critical porosity is $P \geq 0.74$.

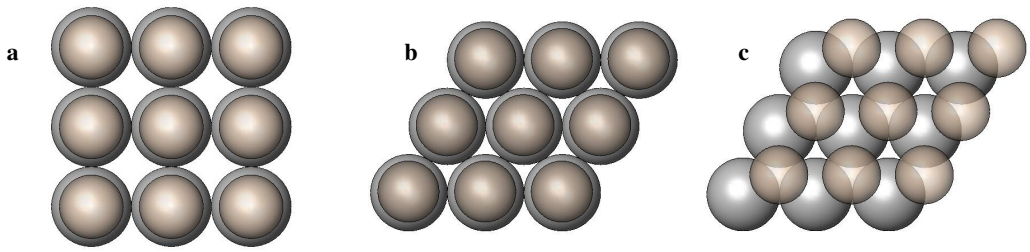

Figure 3.1: Regular arrangements of spherical porosity; **a**) cubic, **b**) orthorhombic, and **c**) rhombohedral. [Top layer of pores intentionally shown smaller for clarity]

For porosity levels beyond the applicable range of the Spriggs (9) equation (i.e., porosity > 40%), Rice [38] recognized that the role of pores and matrix material can be reversed leading to a theoretical equation applicable to larger values of porosity:

$$E_p = E_0 [1 - exp(-r\{1-P\})] \qquad (12)$$

where r is empirically determined to have a value of approximately 0.5. Rice notes that this function is a continuation of the relationship for a simple cubic array of nonintersecting pores in a solid matrix as first derived by Eudier [37] in 1962:

$$E_p = E_0 [1 - \pi (3P/4\pi)^{2/3}] = E_0 (1 - 1.21 P^{2/3}) \qquad (13)$$

These two functions are equivalent at $P = \pi/6 \approx 0.52$ if r is assumed to equal 0.5. The determination of r is again based on a particular set of empirical data and the literature does not describe or quantify the relationship between m in the original Spriggs equation (9) and r in the equation proposed by Rice (13).

The Eudier equation predates similar relationships noted by Martin *et al.* [39] as well as the more recent theoretical work by Herakovich *et al.* [7] which concluded that for cubic packing of spherical pores:

$$E_p = E_0 (1 - 1.15\, P^{2/3}) \tag{14}$$

This equation is consistent with recent studies by Rice where he proposes that the ratio of the effective moduli to the solid (non-porous) moduli is directly proportional to the ratio of the minimum contact area to the total cross-sectional area of periodic structures, often termed the minimum solid area (MSA) model [3]. However, Roberts *et al.* [40] are critical of the MSA model as this method uses "purely geometrical reasoning" to predict the elastic moduli based upon the weakest points within the structure. These authors maintain that the microstructure that corresponds to the MSA predictions "is not exactly known" and that "the MSA models do not provide quantitative agreement" with the moduli of the microstructures they studied. "Semiempirical relations generally provide a reasonable means of describing data, extrapolating results, and comparing data among materials. However, because they lack a rigorous connection with microstructure, these results offer neither predictive nor interpretive power". As described in their finite element (FE) analyses, Roberts *et al.* maintain that Young's modulus is related to the porosity through the equation:

$$E_p = E_0 [1 - (P/t)]^s \tag{15}$$

where the constants *s* and *t* are "empirical correlation parameters" dependent on the microstructure of the solid material. With appropriate correlation parameters, this equation is applicable to the morphology of porous ceramics including randomly placed spherical pores, solid spheres and ellipsoidal pores and may be extended to analyses of microstructures with non-overlapping porous spheres [41].

3.4 Additional property-porosity relationships

In a 1960 paper, Paul [42] noted that the simplest relationship that satisfies the boundary conditions is when it is assumed that both materials contribute to the stiffness of the composite in proportion to their own moduli and fractional volume. This is frequently termed the "rule of mixtures" and takes the form:

$$E_p = E_1 P + E_2 (1-P) \tag{16}$$

where E_1 and E_2 are the Young's moduli of the respective composite materials. When the inclusion is a void, that is, $E_1 = 0$, the equation reduces to:

$$E_p = E_0 (1-P) \tag{17}$$

or the Dewey equation (1). The Paul equation (16) provides an upper bound on the elastic modulus E_p in those cases where both constituent materials (phases) have the same value of Poisson's ratio. Paul also proposed a lower bound for the elastic moduli of a heterogeneous material with the equation:

$$E_p \geq (E_1 E_2)/(E_1 P + E_2[1-P]) \tag{18}$$

which produces no result when one of the phases is a void and E_1 or E_2 is zero. In addition to these bounds, Paul also derived an approximate solution for E_p based upon a model of a cube-shaped inclusion at whose boundary a normal uniform stress is applied:

$$E_p = E_0 (1-P^{2/3})/(1-P^{2/3}+P) \quad (19)$$

He concludes that this equation "seems to correlate [visually] the experimental data [pertaining to cobalt inclusions] quite well". Ishai *et al.* [43] used the same model and solved for a uniform normal displacement at the boundary to obtain:

$$E_p = E_0 (1-P^{2/3}) \quad (20)$$

which described experimental data for porous epoxies up to about 30% volume porosity. Martin *et al.* [39] further modified this relationship to include a factor *u*, a constant dependent upon "the average void properties of the model (variable for different types of porosity)":

$$E_p = E_0 (1-uP^{2/3}) \quad (21)$$

Using experimental data for alumina, bone and gypsum, these authors found this relationship to be "very convincingly confirmed [visually]" with values of *u* between 1.3 and 2.5, but Martin *et al.* also acknowledge that this empirically-derived equation is a "blind alley… in regard to the insight it gives the user…"

Hashin [8] recognized that while the bounds proposed by Paul have the advantage of being exact, they are generally too broadly separated to give a good estimate of the effective Young's modulus, defined as E_{porous}/E_{solid}, of most composite materials. Assuming a spherical shape for the inclusions, he derived another relationship involving only the stresses and strains

inside the inclusions. Both Rice [10] and Boccaccini [44] attribute the equation for the upper bound:

$$E_p = E_0 (1-P)/(1+wP) \quad (22)$$

where $$w = [(1+v_0)(13-15v_0)]/2(7-5v_0) \quad (23)$$

to the analyses detailed in Hashin's 1962 paper. Rice notes that this equation is applicable to a "high concentration of uniformly dispersed spherical pores". Hashin also proposed an equation for a lower bound on the effective modulus but acknowledged that "in such extreme cases as empty cavities,… [these] bounds are not close enough to give a good estimate of the effective moduli" since the gap between the bounds increases with the difference in the elastic properties of the two phases. In his 1983 paper, Hashin [45] notes that his bounds are of practical value only up to a phase stiffness ratio of about 10 and can obviously not provide good estimates for extreme differences in stiffness such as an empty phase (i.e., a porous medium). Ramakrishnan *et al.* [5] also noted that the theoretical model used by Hashin, an assemblage of individual composite spheres consisting of matrix material which enclose another concentric spherical phase or inclusion, is not valid when the difference between the elastic properties of the phases is large [46]. In response to these concerns, Ramakrishnan *et al.* used the equations developed by Hashin *et al.* [47], modified some of the original assumptions, and proposed an alternative relationship:

$$E_p = E_0 (1-P)^2/(1+yP) \quad (24)$$

where $$y = 2 - 3v_0 \quad (25)$$

Ramakrishnan *et al.* [5] compared the predictions of this equation to a large set of experimental data with porosity values ranging from 5 to 40% and predicted the moduli with an

error of about 20%. These authors note that the scatter in the experimental data itself is on the order of 20% and thus "this equation can be considered accurate enough." Later work by Mondal *et al*. [48] extended the applicability of this equation (24) to closed-cell aluminum foam with porosities ranging from 30 to 80%. Their data showed that this equation demonstrated close agreement with the experimental data over the entire range of porosity with a maximum variation of approximately10% at 30% porosity.

Wang *et al*. [4], extended the Hashin equations (22 and 23) by considering the interaction effects between pores, something not included in the Hashin model. The resulting equation is a complicated second-order function of the bulk modulus, Poisson's ratio, shear modulus, and *P* that predicts values for Young's modulus between the upper bound of the Hashin model and the Ramakrishnan model and shows good visual agreement with experimental data up to ~40% porosity.

To assess the effect of pore variables on mechanical properties, Boccaccini derived an equation for Young's modulus of a porous body from the pore content, shape and orientation. The equation was based on an analytical model originally developed for composite materials by Mazilu *et al.* [49]. Extension of that equation to the full porosity range led to the relationship:

$$E_p = E_0 \left(1 - P^{2/3}\right)^{1.21S} \tag{26}$$

where

$$S = (z/x)^{1/3} \sqrt{1 + [(z/x)^{-2} - 1]\cos^2 \varphi} \tag{27}$$

In this equation, z/x is the mean axial ratio (minor axis/major axis) of the spheroidal pores, φ is the angle between the rotational axis of the spheroids and the stress direction, and $\cos^2 \varphi$ is an orientation factor. The ratio z/x equals 1 for spheres and as the ratio approaches zero, oblate

spheroids become disc-shaped and prolate spheroids become needle-shaped [50]. This equation was proposed to be valid across the entire porosity range. However, according to Boccaccini [51], the equation has not been verified experimentally for porosities greater than 40%.

These various equations that attempt to quantify or predict mechanical properties (e.g., Young's modulus) as a function of porosity are summarized in Table 3.1. Aside from the studies by Rossi [13] and Boccaccini [50] on the effect of pore shape, the task of quantifying the influence of pore structure and arrangement within the matrix material on effective moduli has been largely neglected in prior research.

Table 3.1: Summary of relationships for Young's moduli of porous materials

General equation form	Researcher	Year	Ref	% P	Comment
LINEAR EQUATIONS					
1-mP	Dewey	1947	9		
	Gatto	1950	10		with m = 2.36 or 2.636
	Fryxell & Chandler	1963	11	2-17	"describes the data well enough for most practical purposes"
	Hasselman	1964	12	< 2.5	attributes calculation of m to Dewey, MacKenzie and Hashin; $m = 3(9+5\nu_0)(1-\nu_0)/2(7-5\nu_0)$
	Rossi	1968	13	≤ 10	same as the Hashin eqn at low porosity; equals Dewey eqn where $m = (1-\nu)(27+15\nu)/\{2(7-5\nu)\}$
POWER EQUATIONS					
$(1-pP)^q$	Bal'shin	1949	19	unk	only if p =1 (and q goes from 3 to 6); for strength not modulus
	McAdam	1951	21	0-40	if p = 1 and q = 3.4
	Phani	1988	22 -26	5-40	$p = 1/P_{cr}$ where P_{cr} is the porosity at which the modulus goes to zero
	Wagh	1993	27	0-60	p =1
	Maitra	1994	28	0-65	restates Phani; p = 1 and q ranges from 3 to 4
$1-aP^{2/3}$	Eudier	1962	37	0-50	only if a = 1.21
	Ishai	1967	43	0-30	only if a = 1
	Martin	1971	39	0-50	a varies from 1.3 to 2.5

$[1-(P/Q)]^{KQ}$	Bert	1985	14	0-20	K is the stress concentration factor and Q is the maximum porosity possible
$(1-P^{2/3})^{1.21S}$ $S = (z/x)^{1/3} (1 + [(z/x)^{-2} -1] \cos 2\varphi)^{1/2}$	Boccaccini	1997 1999	44 50	0-40	z/x is the mean axial ratio (minor axis/major axis) of the spheroidal pores
$(1-P^{2/3})/(1-P^{2/3}+P)$	Paul	1960	42	-	for inclusions (cobalt) of cubic shape; not voids
$(1-bP+cP^2)$	MacKenzie	1950	15	-	
	Chung	1963	16	-	cites MacKenzie/Gatto as source for this eqn
	Spinner & Knudsen	1963	18	5-40	
$[1-(P/P_0)]^n$	Roberts & Garboczi	2000	40	0-50	n and P_0 are "empirical correlation parameters"
EXPONENTIAL EQUATIONS					
$\exp^{(-bP)}$	Duckworth/ Ryshkewitch	1953	53 30	0-50	b "has a value of about 7 for all experimental data on hand… appears to be independent of pore size"; for strength not modulus
	Knudsen	1959	20	5-31	for strength not modulus
	Spriggs	1961	31	0-37	for open and closed pores
	Knudsen	1962	32	0-40	presents data to support b = 3.95
	Rice	1977	10	0-40	restates Knudsen
1-(exp^[-b'(1-P)])	Rice	1976	38	>40	for pores
$\exp^{(-(bP+cP^2))}$	Wang, J.C.	1984	34 35	0-30	
	Panakkal	1990	36	0-22	
OTHER EQUATIONS					
$(1-P)/(1+k_1P)$ $k_1 = [(1+\nu_0)(13-15\nu_0)]/2(7-5\nu_0)$	Hashin	1962	8	-	if $k_1 = A - 1$, gives same result as Hasselman eqn below
	Wang, L. & Tseng	2003	4	0-50	same eqn as Hashin if inter-pore interaction is neglected
$1- \{AP/[1+(A-1)P]\}$	Hasselman	1962	33	0-16	A = empirical constant; if A = 2, gives same result as Hashin eqn
$(1-P)^2/(1+k_EP)$ $k_E = 2-3\nu_0$	Ramakrishnan	1993	5 46	5-40	
	Mondal	2007	48	< 80	for closed-cell foams

A graphical comparison of these equations is included in Appendix A. The values used to plot these equations are those of the respective researcher with supplemental curves shown for those relationships that specify a range of values for the various input variables.

3.5 Concluding perspectives

Despite the extensive body of research represented by these porosity-property relationships, most lack predictive ability. Rice [10] is critical of much of the prior work as "few investigators studying the dependence of elastic properties on porosity present anything more than density, i.e., average porosity data" when pore shape anisotropy can significantly alter these relationships and invalidate the results. Boccaccini [50] added that most experimental studies in the open literature dealing with porous materials do not supply accurate quantitative descriptions of the porosity structure and cannot be considered for rigorous verification of theoretical approaches. In a 1994 paper [52], he summarized the broader situation: **The utility of a microstructure-property correlation is directly related to its ability to predict the property from microstructural measurements and thus to be used for design purposes.**

The need to proactively address the concerns of stress shielding and the resulting bone resorption requires the use of **validated predictive equations** for Young's modulus and Poisson's ratio over a porosity range of 20-50%. This review of current data and porosity-property relationships indicates that such predictive equations do not yet exist for the application of engineered porosity to the design of clinically-relevant orthopaedic implants.

3.6 References

[1] Ryan, G., Pandit, A., Apatsidis, D.P., *Fabrication methods of porous metals for use in orthopaedic applications*, Biomaterials, Vol. 27, No. 13, pp. 2651-2670, 2006.

[2] Li, C., Zhu, Z., *Dynamic Young's modulus of open-porosity titanium measured by the electromagnetic acoustic resonance method*, Journal of Porous Materials, Vol. 13, pp. 21-26, 2006.

[3] Ji, S., Gu, Q., Xia, B., *Porosity dependence of mechanical properties of solid materials*, Journal of Materials Science, Vol. 41, pp. 1757-1769, 2006.

[4] Wang, L., Tseng, K.K., *A multi-scale framework for effective elastic properties of porous materials*, Journal of Materials Science, Vol. 38, pp. 3019-3027, 2003.

[5] Ramakrishnan, N., *Effective Elastic Moduli of Porous Ceramic Materials*, Journal of the American Ceramic Society, Vol. 76, No. 11, pp. 2745-2752, 1993.

[6] O'Kelly, K.U., Carr, A.J., McCormack, B.A.O., *Minimum solid area models applied to the prediction of Young's modulus for cancellous bone*, Journal of Materials Science: Materials in Medicine, Vol. 14, pp. 379-384, 2003.

[7] Herakovich, C.T., Baxter, S.C., *Influence of pore geometry on the effective response of porous media*, Journal of Materials Science, Vol. 34, No. 7, pp. 1595-1609, 1999.

[8] Hashin, Z, *The Elastic Moduli of Heterogeneous Materials,* Journal of Applied Mechanics, Vol. 29, pp.143-150, 1962

[9] Dewey, J.M., *The Elastic Constants of Materials Loaded with Non-Rigid Fillers*, Journal of Applied Physics, Vol. 18, pp. 578-581, 1947.

[10] Rice, R.W., *Microstructure Dependence of Mechanical Behavior of Ceramics*, Treatise on Material Science, Vol. 11, pp. 199-381, Academic Press, New York, 1977.

[11] Fryxell, R.E., Chandler, B.A., *Creep, Strength, Expansion and Elastic Moduli of Sintered BeO as a Function of Grain Size, Porosity, and Grain Orientation,* Journal of The American Ceramic Society, Vol. 47, No. 6, pp. 283-291, 1964

[12] Hassselman, D.P.H., Fulrath, R.M., *Effect of Small Fraction of Spherical Porosity on Elastic Moduli of Glass*, Journal of The American Ceramic Society, Vol. 47, No. 1, pp. 52-53, 1964.

[13] Rossi, R.C., *Prediction of the Elastic Moduli of Composites*, Journal of The American Ceramic Society, Vol. 51, No. 8, pp. 433-439, 1968.

[14] Bert, C.W., *Prediction of elastic moduli of solids with oriented porosity,* Journal of Materials Science, Vol. 20, pp. 2220-2224, 1985.

[15] MacKenzie, J.K., *The Elastic Constants of a Solid containing Spherical Holes*, Proceedings of the Physical Society, Section B, Vol. 63, pp 2-11, 1950.

[16] Chung, D-H, *Elastic Moduli of Single Crystal and Polycrystalline MgO*, Philosophical Magazine, Vol. 8, pp. 833-841, 1963.

[17] Wagh, A.S., Poeppel, R.B., Singh, J.P., *Open pore description of mechanical properties of ceramics*, Journal of Materials Science, Vol. 26, pp. 3862-3868, 1991.

[18] Spinner, S., Knudsen, F.P., Stone, L., *Elastic Constant-Porosity Relations for Polycrystalline Thoria*, Journal of Research of the National Bureau of Standards - C, Vol. 67C, pp. 39-46, 1963

[19] Bal'shin, M.Y., *Relation of mechanical properties of powder metals and their porosity and the ultimate properties of porous metal-ceramic materials*, Doklady Akademii Nauk SSSR, Vol. 67, No. 5, pp. 831-834, 1949.

[20] Knudsen, F.P., D*ependence of Mechanical Strength of Brittle Polycrystalline Specimens on Porosity and Grain Size*, Journal of The American Ceramic Society, Vol.; 42, No. 8, pp. 376-387, 1959.

[21] McAdam, G.D., *Some Relations of Powder Characteristics to the Elastic Modulus and Shrinkage of Sintered Ferrous Compacts*, Journal of the Iron and Steel Institute, pp. 346-358, 1951.

[22] Phani, K.K., *Elastic-constant-porosity relations for polycrystalline thoria*, Journal of Materials Science Letters, Vol. 5, pp. 747-750, 1986

[23] Phani, K.K., Niyogi, S.K., *Porosity dependence of ultrasonic velocity and elastic modulus in sintered uranium dioxide*, Journal of Materials Science Letters, Vol. 5, pp. 427-430, 1986

[24] Phani, K.K., *Young's Modulus-Porosity Relation in Gypsum Systems*, American Ceramic Society Bulletin, Vol. 65, No.12, pp. 1584-1586, 1986.

[25] Phani, K.K., Niyogi, S.K., *Young's modulus of porous brittle solids,* Journal of Materials Science, Vol. 22, No. 1, pp. 257-263, 1987.

[26] Phani, K.K., Niyogi, S.K., De, A.K., *Porosity dependence of fracture mechanical properties of reaction sintered S3N4*, Journal of Materials Science Letters, Vol. 7, pp. 1253-1256, 1988.

[27] Wagh, A.S., Singh, J.P., Poeppel, R.B., *Dependence of ceramic fracture properties on porosity*, Journal of Materials Science, Vol. 28, pp. 3589-3593, 1993.

[28] Maitra, A.K., Phani, K.K. *Ultrasonic evaluation of elastic parameters of sintered powder compacts*, Journal of Materials Science, Vol. 29, pp. 4415-4419, 1994.

[29] Paskaramoorthy, R., Meguid, S.A., *On the dynamic behavior of porous materials*, International Journal of Solids and Structures, Vol. 37, pp. 2341-2358, 2000.

[30] Duckworth, W., *Discussion of Ryshkewitch Paper*, Journal of the American Ceramic Society, Vol. 36, No. 2, p. 68, 1953.

[31] Spriggs, R.M., *Expression for Effect of Porosity on Elastic Modulus of Polycrystalline Refractory Materials, Particularly Aluminum Oxide*, Journal of the American Ceramic Society – Discussions and Notes, pp. 628-629, December, 1961.

[32] Knudsen, F.P., *Effect of Porosity on Young's Modulus of Alumina*, Journal of The American Ceramic Society, Vol.; 45, No. 2, pp. 94-95, 1962.

[33] Hassselman, D.P.H., *On the Porosity Dependence of the Elastic Moduli of Polycrystalline Refractory Materials*, Journal of The American Ceramic Society, Vol. 45, No. 9, pp. 452-453, 1962.

[34] Wang, J.C., Young's modulus of porous materials – Part 2: Young's modulus of porous alumina with changing pore structure, Journal of Materials Science, Vol. 19, No. 3, pp. 809-814, 1984.

[35] Wang, J.C., *Young's modulus of porous materials – Part 1: Theoretical derivation of modulus-porosity correlation*, Journal of Materials Science, Vol. 19, No. 3, pp. 801-808, 1984.

[36] Panakkal, J.P., Willems, H., Arnold, W., Nondestructive evaluation of elastic parameters of sintered iron powder compacts, Journal of Materials Science, Vol. 25, pp. 1397-1402, 1990.

[37] Eudier, M., *The Mechanical Properties of Sintered Low-Alloy Steels*, Powder Metallurgy, No. 9, pp. 278-290, 1962.

[38] Rice, R.W., *Extension of the Exponential Porosity Dependence of Strength and Elastic Moduli*, Journal of the American Ceramic Society – Discussions and Notes, Vol. 59, No. 11-12, pp. 536-537, 1976.

[39] Martin, R.B., Haynes, R.R., *Confirmation of Theoretical Relation Between Stiffness and Porosity in Ceramics*, Journal of The American Ceramic Society, Vol. 54, No. 8, pp. 410-411, 1971.

[40] Roberts, A.P., Garboczi, E.J., *Elastic Properties of Model Porous Ceramics*, Journal of The American Ceramic Society, Vol. 83, No. 12, pp. 3041-3048, 2000.

[41] Roberts, A.P., Garboczi, E.J., *Elastic properties of model random three-dimensional open-cell solids*, Journal of the Mechanics of Physics of Solids, Vol. 50, No. 1, pp. 33-55, 2002.

[42] Paul, B., *Prediction of Elastic Constants of Multiphase Materials*, Transactions of the Metallurgical Society of AIME, Vol. 218, pp. 36-41, 1960.

[43] Ishai, O., Cohen, L.J., *Elastic Properties of Filled and Porous Epoxy Composites*, International Journal of Mechanical Sciences, Vol. 9, pp. 539-546, 1967.

[44] Boccaccini, A.R., Fan, Z., *A New Approach for the Young's Modulus-Porosity Correlation of Ceramic Materials*, Ceramics International, Vol. 23, pp. 239-245, 1997.

[45] Hashin, Z., *Analysis of Composite Materials- A Survey*, Transactions of the ASME, Vol. 50, pp. 481505, 1983.

[46] Ramakrishnan, N., Arunachalam, V.S., *Effective Elastic Moduli of Porous Solids*, Journal of Materials Science, Vol. 25, pp. 3930-3937, 1990.

[47] Hashin, Z., Shtrikman, S., *A Variational Approach to the Theory of the Elastic Behaviour of Multiphase Materials*, Journal of Mechanics and Physics of Solids, Vol. 11, pp. 127-140, 1963.

[48] Mondal, D.P., Ramakrishnan, N., Suresh, K.S., Das, S., *On the moduli of closed-cell aluminum foam*, Scripta Materialia, Vol. 57, pp. 929-932, 2007.

[49] Mazilu, P., Ondracek, G., *Thermal effects in fracture of multiphase materials*, Proceedings of Euromech Colloquium, p. 214, Springer Verlag, Berlin, 1989.

[50] Boccaccini, A. R., *Fabrication, Microstructural Characterization and Mechanical Properties of Glass Compacts Containing Controlled Porosity of Spheroidal Shape*, Journal of Porous Materials, Vol. 6, pp. 369-379, 1999.

[51] Personal communication with A.R. Boccaccini, March 13, 2011.

[52] Boccaccini, A.R., *Comment on "Dependence of ceramic fracture properties on porosity"*, Journal of Materials Science Letters, Vol. 13, pp. 1035-1037, 1994.

[53] Ryshkewitch, E., *Compression Strength of Porous Sintered Alumina and Zirconia*, Journal of The American Ceramic Society, Vol. 36, No. 2, pp. 65-68, 1953.

4. Finite Element Modeling of Representative Volume Elements

4.1 Introduction

In a 1996 paper on physical property-porosity models, Rice [1] notes that the use of spherical particles or pores in the three basic close packings (cubic, orthorhombic and rhombohedral) has not been adequately evaluated and "isotropy has apparently not been considered before" as the presumption is that the mechanical properties of porous structures are isotropic. He further adds that Knudsen's original calculations as detailed in his 1959 paper [2], one of few describing the effect of defined porosity on mechanical properties, were of three different sphere stackings, but only for one [loading] direction for each of these [pore] stackings".

The focus of the finite element (FE) analyses detailed in this study is to first, evaluate specific porous microstructures to assess their effect on effective moduli, secondly, assess the isotropy (or anisotropy) of these structures, and thirdly, to optimize the structure parameters to obtain a desired combination of mechanical properties, notably a predictable reduction in the modulus of elasticity. Specific design parameters (i.e., pore size, center-to-center pore dimension and stacking arrangement) are evaluated for their effect on porosity and effective moduli and the microstructure that offers optimal potential for clinical application is identified. The design procedure used in these analyses permits global manipulation of porosity design parameters. Due to the current limits of practical fabrication technology for the production of well-defined pores, these microstructures are defined as having feature sizes, such as pore radii and pore separation, in the range of ~200 to 2000 μm. The resulting physical constructs which incorporate this "designed" porosity are useful as model systems to verify the accuracy of the theoretical and numerical approaches that intend to describe the properties of porous materials [3].

The FE analyses in this chapter are part of a larger effort to determine if engineered porosity can predictably modify the effective moduli, specifically Young's modulus and Poisson's ratio, of an orthopaedic implant to reduce the effect of stress-shielding on host bone.

4.2 Methodology

This research involves the development of a series of representative volume elements (RVEs) consisting of unit cells that incorporate regular arrangements [i.e., cubic, orthorhombic, tetragonal and rhombohedral ordering] of spherical pores as shown in Figure 4.1.

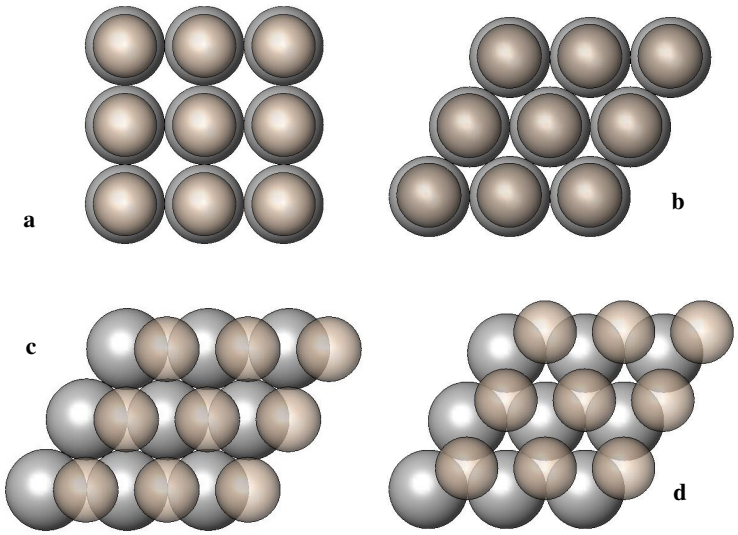

Figure 4.1: Regular arrangements of spherical porosity; **a**) cubic, **b**) orthorhombic, **c**) tetragonal-spenoidal, and **d**) rhombohedral. Top layer of pores intentionally shown smaller for clarity.

The response of these RVEs to an applied load was simulated using FE methods to estimate the average internal stress and lateral/axial strain such that effective moduli can be calculated. The direction of the applied load on these unit cells was changed to assess the anisotropy of the resulting porous structure. Through the use of a design of experiments (DoE)

procedure, a dominant design parameter or combination of parameters was identified that leads to predictable modification in the effective moduli of a physical construct that incorporates those design parameters. The specific methodology for this study is summarized in the process flow chart depicted in Figure 4.2.

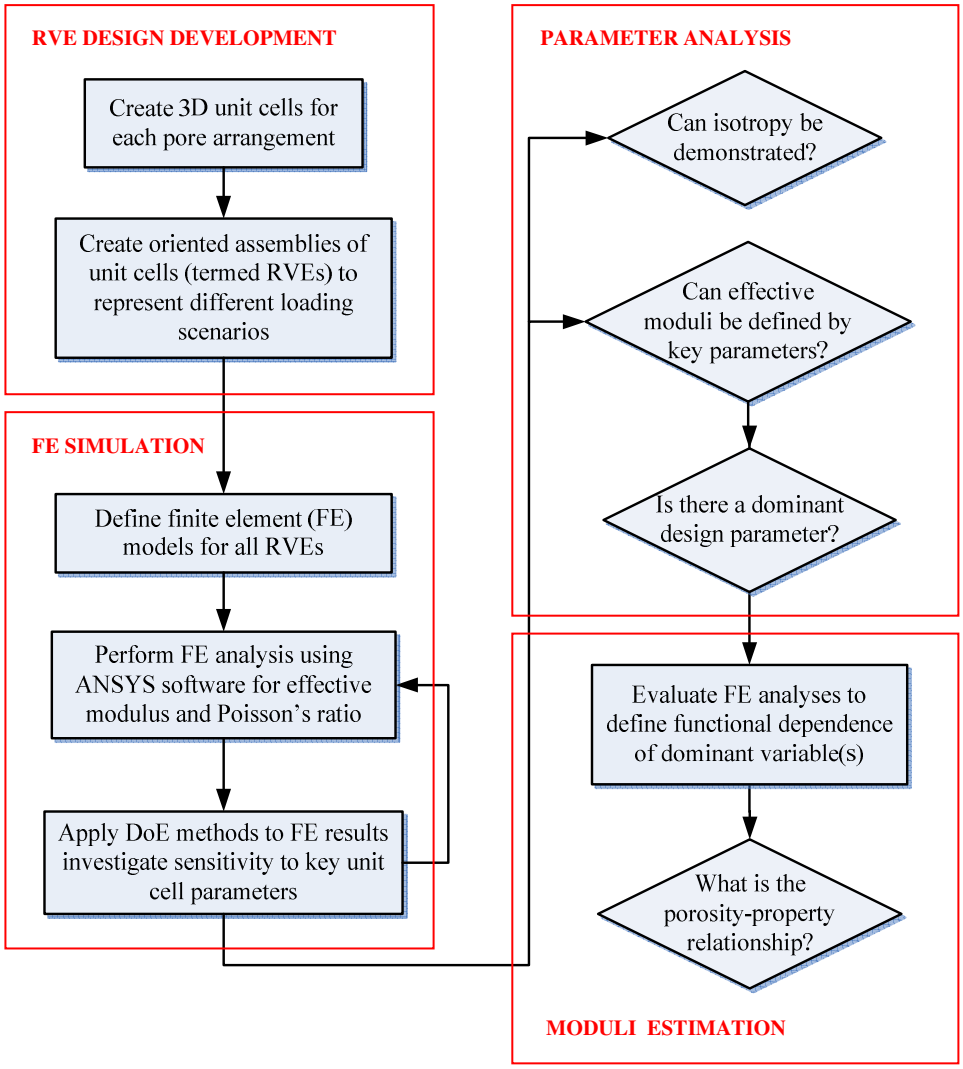

Figure 4.2: Schematic diagram describing FE modeling methodology.

4.2.1 RVE design

The development of accurate representations of RVEs under differing loading scenarios first requires a determination of **possible regular arrangements of spherical pores** and the **creation of unit cells that result from those pore arrangements**. In this study, the unit cells are the Boolean inverse of the pore arrangements described in this section.

Unit cells

To visualize the generation of a unit cell from a specific pore arrangement, a rhombohedral or hexagonal close-packed (HCP) pore structure is shown in Figure 4.3a. Given this arrangement of spherical pores, the resulting structure represented by the material between the pores can be described in terms of the variable parameters of pore size, pore separation, *s*, or center-to-center pore dimension, *L*, and pore orientation or stacking arrangement. Figure 4.3b represents the Boolean inverse of this pore model and shows the resulting unit cell and parameters used to form the RVE.

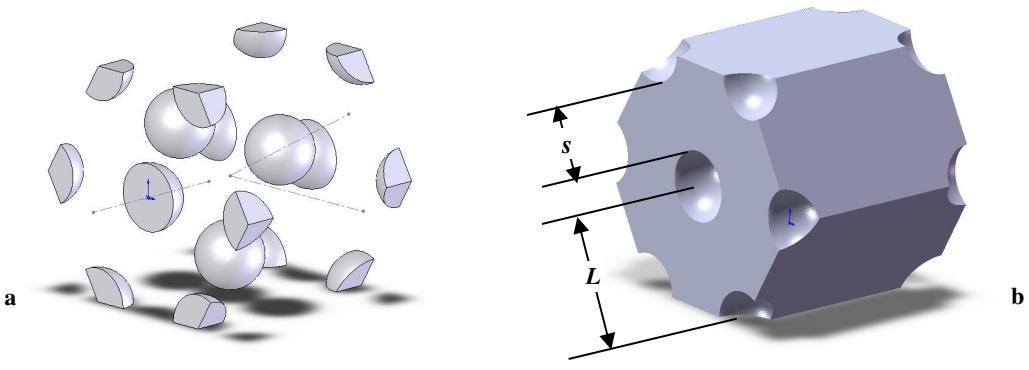

Figure 4.3: HCP model; **a**) pore arrangement, **b**) Boolean inverse representing the solid structure or unit cell.

Regular close-packed arrangements, characterized by pores that are in contact with all adjacent pores at maximum porosity, are generated from the stacking and subsequent realignment

of consecutive layers that incorporate rows of individual spherical pores. One additional non-close-packed pore model, the body-centered cubic (BCC) arrangement, is included in the study for subsequent comparison to the results associated with those of close-packed porous microstructures.

Two fundamental types of porous layers of close-packed pores are shown in Figure 4.4 and depict the limiting arrangement of 90° and 60° for those respective angles of intersection.

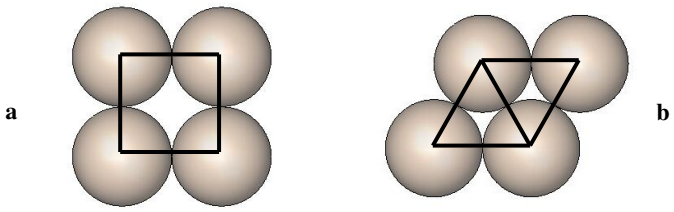

Figure 4.4: Fundamental arrangements of porous layers; **a**) square layer (90 deg) and **b**) rhombic or triangular layer (60 deg).

Three geometrically simplistic methods of arranging either type of porous layer are possible by stacking directly atop and aligned with the layer below, or offset in a single orthogonal direction or offset in two orthogonal directions. This implies that there are a total of six possible close-packed arrangements. However, two arrangements of square layers are identical to two of the three possible stacking arrangements for the rhombic layers. Thus, there are only four unique regular pore arrangements given the assumptions of close packing and the aforementioned angles of intersection. These pore arrangements are generally described as cubic, orthorhombic, tetragonal (or tetragonal-spenoidal), and rhombohedral as noted in Figure 4.1[4].

The Boolean inverse of the stacking variations of consecutive **square layers** of pores, as shown in Figure 4.5, results in the generation of simple cubic (SC), hexagonal prismatic (HP) or face-centered cubic (FCC) unit cells.

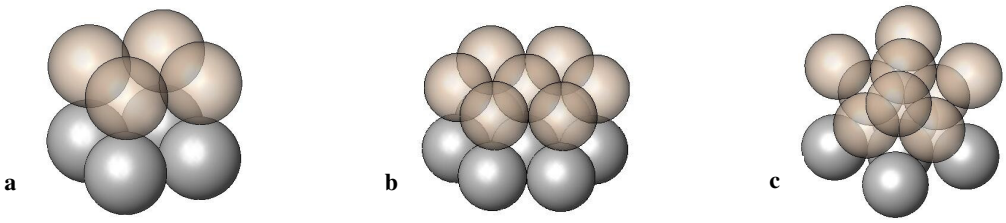

Figure 4.5: Square layer pore arrangements; **a**) simple cubic (SC), **b**) hexagonal prismatic (HP) and **c**) face-centered cubic (FCC).

Starting with a square layer of pores, all layers can be stacked without offset in one orthogonal direction. The resulting SC unit cell represents the solid material between the pores and has a single pore at each corner of the cube. The total number of partial pores in the SC unit cell is eight and the orientation of the faces is coincident with all three orthogonal planes.

The porosity parameters of the SC unit cell, as well as those of the other unit cells detailed in this section, are summarized in Table 4.1. The variable r is the pore radius, L is the resulting pore dimension between the nearest adjacent pores for a given unit cell structure, and ψ is the ratio of r/L. The maximum porosity of each unit cell occurs when the ratio ψ equals 0.5.

Table 4.1: Summary of porosity for modeled unit cells.

	Unit cell	Figure	Porosity relationship as function of r, L and ψ ratio		Maximum porosity
Square close-packed layers (Figure 4.4a)	SC	4.5a	$[4(⅓)\pi r^3] / L^3$	$4.18879\ (\psi)^3$	52.4%
	HP	4.5b	$(4\pi r^3) / 1.5\sqrt{3}\ L^3$	$4.83679\ (\psi)^3$	60.5%
	FCC	4.5c	$[16(⅓)\pi r^3] / (\sqrt{2})^3\ L^3$	$5.92379\ (\psi)^3$	74.1%
Rhombic close-packed layers (Figure 4.4b)	HP	4.5b	$(4\pi r^3) / 1.5\sqrt{3}\ L^3$	$4.83679\ (\psi)^3$	60.5%
	Tetragonal-sphenoidal	4.6c	N/A		
	HCP	4.6a	$(8\pi r^3) / \sqrt{18}\ L^3$	$5.92384\ (\psi)^3$	60.5%
	FCC	4.6b	$[16(⅓)\pi r^3] / (\sqrt{2})^3\ L^3$	$5.92379\ (\psi)^3$	74.1%
Non-close packed	BCC	4.7	$(\sqrt{3})\ \pi r^3 / L^3$	$5.44141\ (\psi)^3$	68.0%

If the second and subsequent square layers of pores are each offset by a distance *r* in one orthogonal direction, the resulting arrangement is termed an **orthorhombic** or cubical-tetrahedral packing. The resulting unit cell consisting of the solid material between the pores of this arrangement takes the form of a HP, with 7 pores on each hexagonal face.

Offsetting the second and subsequent square layers of pores by a distance *r* in two orthogonal directions results in a pyramidal, cubic close-packed or **rhombohedral** packing. The solid material between the pores in a rhombohedral packing creates a FCC unit cell. Note that at maximum porosity, the pores along any face diagonal are in contact, while the pores at the respective corners of the FCC unit cell are separated by solid material with a thickness:

$$x_{FCC} = 2[L(cos\ 45°) - r]$$

The stacking of consecutive **rhombic or triangular layers** of pores, as shown in Figure 4.6, and their Boolean inverse leads to the development of tetragonal prismatic, HCP and FCC unit cells, as well as the HP cell described previously.

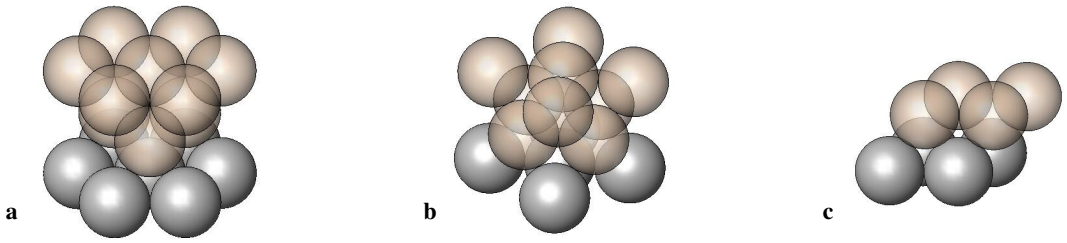

Figure 4.6: Rhombic layer pore arrangements; **a**) hexagonal close-packed (HCP), **b**) FCC, and **c**) tetragonal-spenoidal.

If the second and all subsequent rhombic layers of pores are stacked without offset in one orthogonal direction, the resulting arrangement again forms an **orthorhombic** structure. The solid material between the pores takes the form of a HP unit cell, as described previously.

Offsetting the second and subsequent layers of pores a distance *r* in one orthogonal direction generates a tetragonal-sphenoidal (TS) pore arrangement. The unit cell formed from this pore arrangement has four faces, two of which are non-standard rhombi with an included angle of 79.5°. Due to the intrinsic geometric complexity of the Boolean inverse of the TS pore arrangement, this unit cell is not included in this study.

If the second layer rhombic layer of pores is offset in **two** orthogonal directions, two **rhombohedral** structures are possible, depending upon the placement of the **third** layer. If the first and third layers are aligned in all three orthogonal planes, the solid material between the pores creates an HCP unit cell. The total number of partial pores in a single HCP cell is seventeen, which includes 3 pores in the plane between the 2 hexagonal faces. Note that the 3 pores in the plane between the hexagonal faces extend beyond the surface of the prismatic unit cell if:

$$r > 0.5(\tan 30°)L$$

However, in any situation where the pore radius exceeds this value, the pore volume outside the unit cell is exactly equal to the pore volume introduced into the unit cell by adjacent prismatic elements with the same shape and pore size/length relationships.

If the first and third pore layers are offset relative to each other due to the alternate placement of the pores on the second layer, the solid material between the pores create an FCC unit cell, with parameters as detailed previously. Although the HCP and FCC unit cells have the same volume porosity, the opportunity to investigate the response of these two unit cells to different loading conditions led to the incorporation of the HCP unit cell in this study and became the basis for an additional set of RVEs.

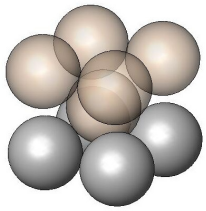

Figure 4.7: Body-centered cubic (BCC) pore arrangement

For purposes of comparison, one non-close packed pore arrangement, the Boolean inverse of which is a body-centered cubic (BCC) unit cell, is also considered in this study. As the BCC unit cell does not result from variations in the stacking of close-packed spheres, a description of its origination is not included. Note that only the pores along the lines connecting diagonally-opposite corners of the cubic solid are in contact with each other at maximum porosity. At any porosity, the pores on the corners of the BCC unit cell are separated by solid material with a thickness:

$$x_{BCC} = 2[(L/\sqrt{3}) - r]$$

Rather than attempt to evaluate each pore structure under different loading conditions, those pore arrangements most likely to be of clinical relevance to the design of orthopaedic implants were identified. The goal of this study is not only to determine if these porous structures exhibit isotropic mechanical properties but also to find those structures and/or loading conditions that will produce the most significant reduction in effective moduli as a means of more nearly approximating the mechanical properties of the host bone.

It is well established that, irrespective of pore arrangement, increases in volume porosity result in decreases in Young's modulus [1, 5]. Figure 4.8 shows the relative changes in volume porosity as a function of pore radius/minimum center-to-center pore dimension, ψ (r/L), for various unit cells. Note that the FCC and HCP pore arrangements exhibit the same volume porosity relationship with variations in ψ. The significance of these data is that for a given porosity design (i.e., specification of pore size and minimum center-to center dimension), the FCC, HCP and BCC unit cells yield the largest volume porosity and offer the greatest potential

reduction in effective Young's modulus, defined as E_{porous}/E_{solid}. The subsequent FE analyses and isotropy assessment accordingly focuses on these three unit cells.

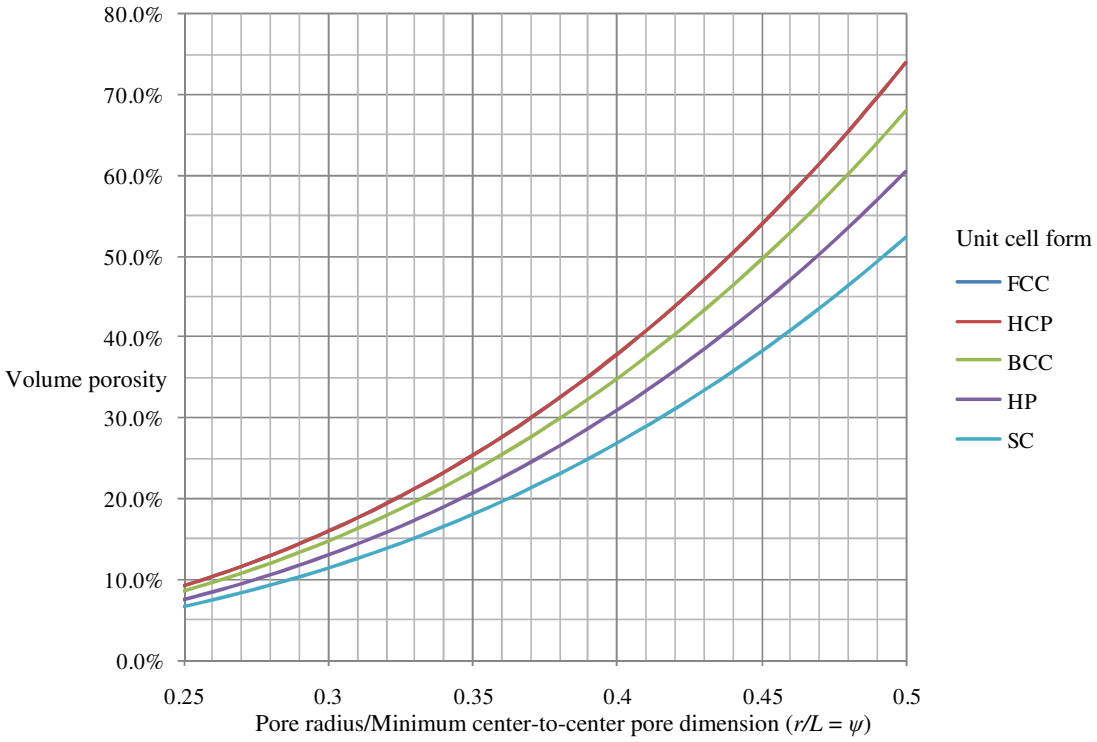

Figure 4.8: Porosity versus ψ for different unit cells. Note that FCC and HCP unit cells have the same porosity for a given ψ.

Loading conditions

Few researchers have investigated the effect of loading direction on moduli since the ability to create desired microstructures with well-defined pore arrangements has been limited to approximations created by gas injection or the decomposition of foaming agents in a molten media, both of which produce random pore distributions [6]. Development of additive manufacturing (AM) processes allows the accurate replication and fabrication of porous microstructures for potential clinical applications. An assessment of the response to different loading conditions is needed to predict mechanical properties and in-use performance.

Given that the unit cells that result from the previously described pore arrangements have either a cubic or hexagonal prismatic shape, only a limited number of practical symmetric loading configurations exist. In the instance of those with a cubic shape (FCC or BCC unit cells), loads can be applied to **opposing parallel faces** of the unit cell (load condition 1), a loading scenario analogous to a < 010 > crystallographic orientation using Miller indices [13]. Similarly, load can be applied to **diagonally opposite edges** of the regular cubic structure (load condition 2) or a < 110 > orientation. It is also conceivable that load can be applied to the **diagonally opposite corners** of these cubic unit cells (load condition 3) or a < 111 > orientation. Figure 4.9 shows these representative loading conditions on the FCC unit cell.

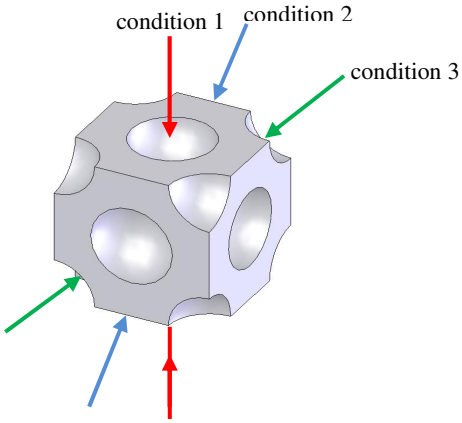

Figure 4.9: Visualization of representative loading conditions for FCC unit cell; <010>: condition 1, <110>: condition 2, and <111>: condition 3

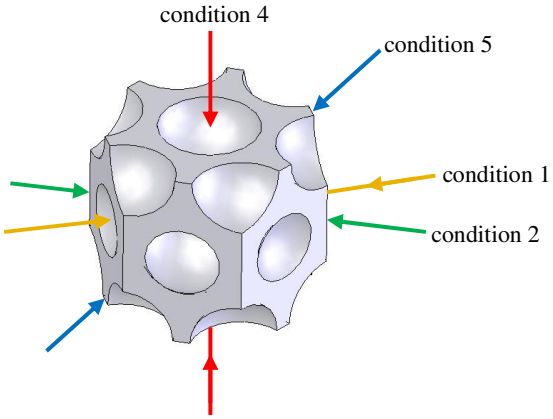

Figure 4.10: Visualization of representative loading conditions for HCP unit cell; condition 1, condition 2, condition 4 and condition 5

In the case of unit cells that have the shape of a hexagonal prism, such as HCP unit cells, load can be applied to the **opposing parallel rectangular faces** of the prism (load condition 1) or to the **opposing parallel hexagonal faces** (load condition 4). It is also possible for the unit cell to be oriented such that load is applied along the **diagonally opposite edges of the hexagonal**

faces (load condition 5) or the **opposing parallel edges of the rectangular** sides of the hexagonal prism (load condition 2). Due to geometric complexity, loading of the diagonally opposing corners of the HCP unit cell was not considered in this analysis. Figure 4.10 shows the representative loading conditions on the HCP unit cell. Note that each vector in Figures 4.9 and 4.10 represents the resultant force over the corresponding surface, edge or corner of the unit cell.

Solid models representing each loading condition are created from a large assemblage of individual unit cells using computer-aided design (CAD) software. Planes are inserted at critical locations through the assembly so as to create and isolate an RVE that represents the desired loading orientation on a specific microstructure. Figure 4.11 depicts the development of two example RVEs using this procedure.

Figure 4.12 shows the RVE assemblies of multiple individual unit cells and the various loading conditions applied to the respective edges and faces of each unit cell investigated in this study. Each RVE assembly has a cubic shape such that FE methods can be used to simulate a uniform displacement of the top face; the resulting internal stress distribution and deformation of the non-loaded faces are then evaluated to determine the effective Young's modulus and Poisson's ratio associated with a given loading condition. The notation used to describe the orthogonal directions and respective faces of all RVEs is also shown in Figure 4.12.

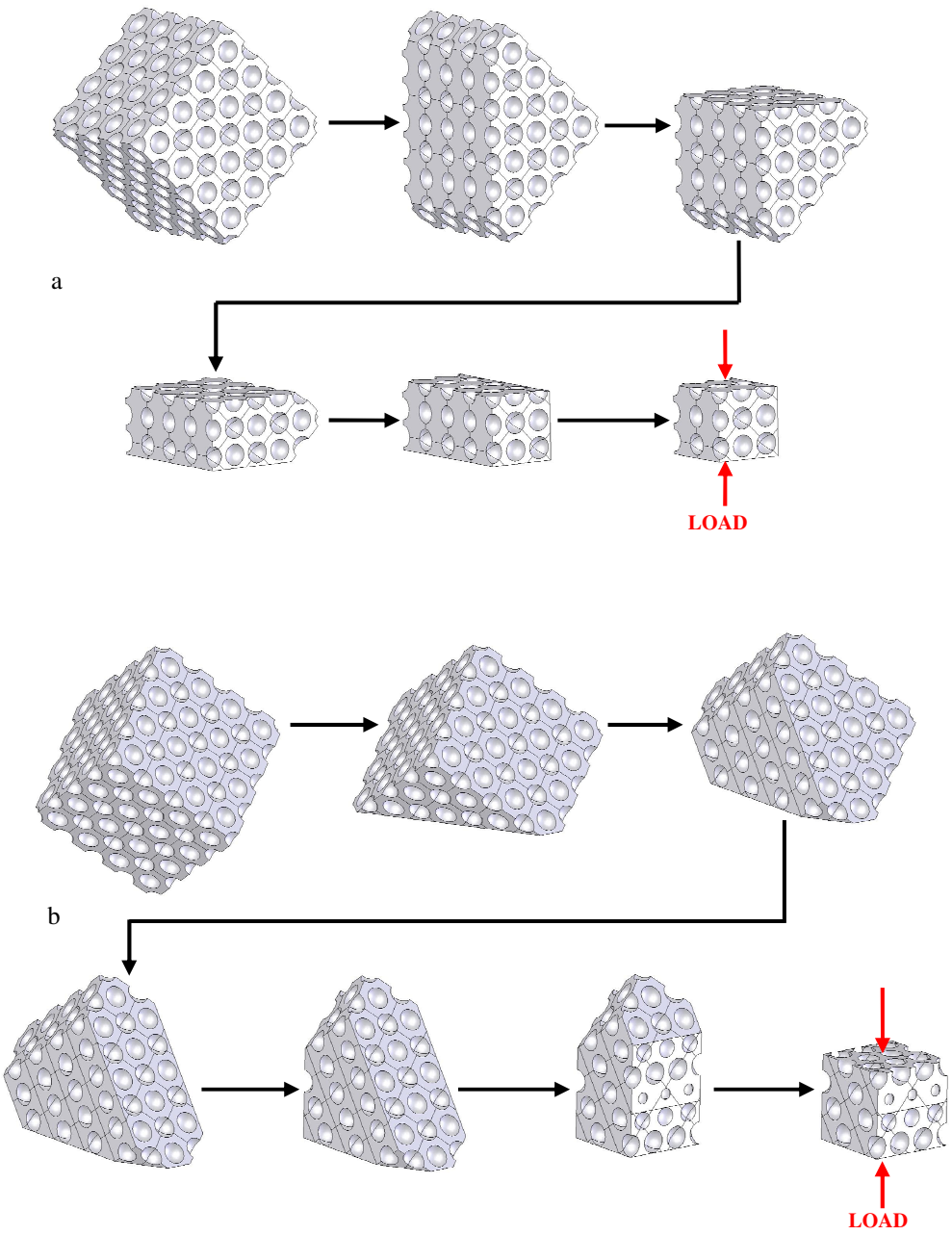

Figure 4.11: Progression of solid model development from large assembly of unit cells with appropriate load orientation to final RVE for FE simulation; **a**) RVE for loading applied to the opposing edges of the FCC unit cell (load condition 2): **A2**; **b**) RVE for loading applied to the opposing corners of the FCC unit cell (load condition 3): **A3**.

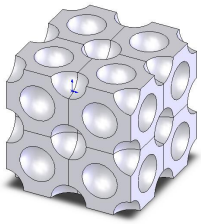

A1: FCC; load condition 1

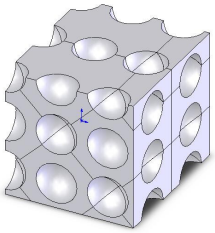

A2: FCC; load condition 2

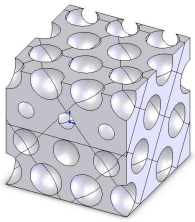

A3: FCC; load condition 3

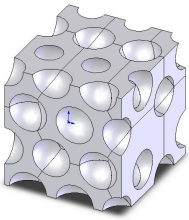

B1a: HCP; load condition 1

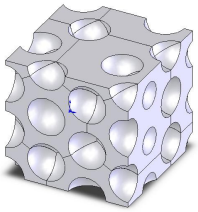

B2a: HCP; load condition 2

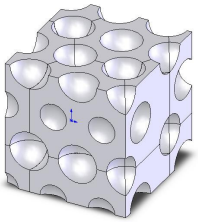

B4a: HCP; load condition 4

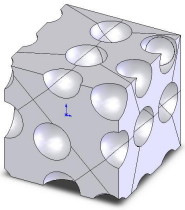

B5a: HCP; load condition 5

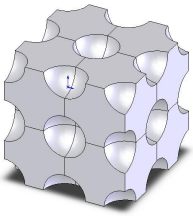

C1: BCC; load condition 1

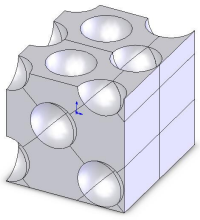

C2: BCC: load condition 2

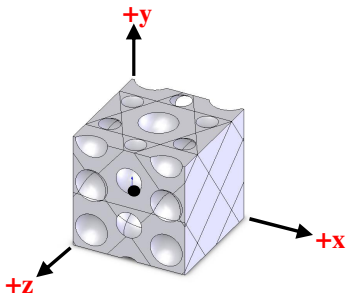

C3: BCC; load condition 3

Figure 4.12: RVE assemblies of unit cells for FE analysis. Cell orientation within RVE is dependent upon specific loading direction. Simulated displacement is applied to top face of all RVEs in the –y direction. Axes and coordinate origin for all RVEs are as indicated for C3.

4.2.2 FE simulation

As noted by Huiskes *et al.*[7], the stresses within an implant structure depend on the magnitudes and directions of the external loads, the elastic moduli of the materials, the shape of the individual structures (implant and bone), and their fixation characteristics. If these four characteristics can be described quantitatively, then the stress patterns can be estimated using FE methods.

To gain a better understanding of changes in the effective moduli as a function of loading, a FE model corresponding to each RVE was defined in terms of element selection, material properties, mesh design, applied loads, boundary conditions and model size/scaling factors. Ideally, the number of unit cells within the FE model can be deemed sufficiently large once periodicity in the response is observed within a central sub-domain of the RVE, both in the direction of the load and across a plane perpendicular to the applied load. This issue is addressed in the development of the appropriate boundary conditions for the subsequent FE modeling.

The ten RVE models consisting of assemblies of individual unit cells as shown in Figure 4.12 were created using SolidWorks® software (2005 SP3.1) and exported as SAT (Standard ACIS Text) files for subsequent FE analysis. FE modeling was conducted using ANSYS® finite element analysis software (version 12.0.1). Importing the RVE geometry as SAT (Standard ACIS Text) files accurately reproduces the as-designed internal porous structure.

Element selection

Each RVE was modeled using ten-node tetrahedral elements with 3 translational degrees of freedom and quadratic displacement behavior (element 187 SOLID). This element type facilitates the analysis of these complex porous structures and the resulting

irregular meshes. In some instances, the geometry of the porous construct required the removal of mid-side nodes which results in linear displacement along that edge.

Material properties

As the porous construct for physical testing (Chapter 5) was to be fabricated in Ti6Al4V, a Young's modulus of 113.8 GPa and a Poisson's ratio of 0.342 [8] were assigned to all elements prior to meshing.

Mesh design

Use was made of ANSYS' SmartSize meshing option to generate elements with minimal shape distortion and optimal aspect ratios. A qualitative comparison of the differences in mesh quality as a function of the SmartSize size level setting is shown in Figure 4.13. Note that the value of the SmartSize setting has no quantitative relationship to the resulting element size or mesh density.

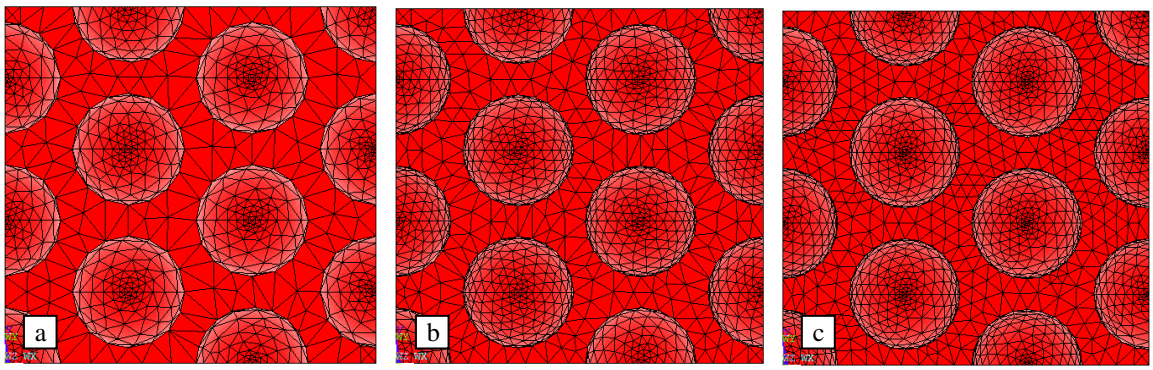

Figure 4.13: SmartSize comparison; **a**) **level 4**: 50,635 elements/77,751 nodes, **b**) **level 3**: 107, 561 elements/159,001 nodes, **c**) **level 2**: 154, 662 elements/226,335 nodes.

An iterative process was used for mesh refinement. The average stress across a given plane through the RVE perpendicular to the applied deformation at a specific SmartSize level was calculated. The SmartSize level was reduced, resulting in a finer mesh, and the average stress calculation was repeated. This procedure continued until the average stresses across the given plane for consecutive iterations converged and differed by less than 0.02%.

Applied loads and boundary conditions

Initial analyses demonstrated that having sufficient constraints, independent of the applied load, are required for unique solution. Thus, although these structures were only subject to unidirectional loads, a combination of translational and rotational constraints was necessary to avoid rigid body motion.

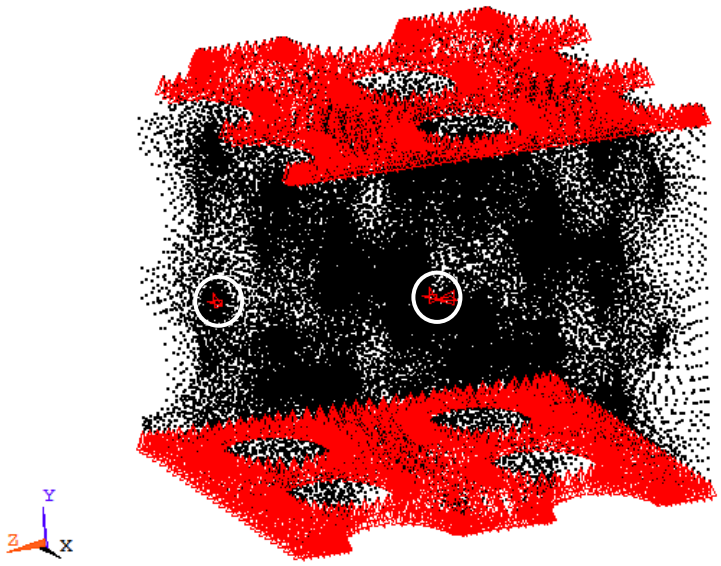

Figure 4.14: Representative RVE with coordinate system, translational constraints and applied loads/constraints. Nodal constraints to rigid body motion are circled for clarity.

As depicted in Figure 4.14, rigid body motion was controlled by applying translational constraints ($u_x = u_z = 0$) to a node on a line parallel to the y-axis and passing through the

approximate center of the RVE. To prevent rotation, a node midway across either z-face was constrained such that $u_x = 0$. Each RVE was subject to a simulated displacement in the (–) y-direction (u_y) equal to 1% of the y-dimension, y_{max}, of the RVE. The dimensions for all RVEs are noted in Appendix C.

Additional boundary conditions were applied as detailed by Shen and Brinson such that the modeled RVE approximates the continuum of the periodic microstructure [9]. To obtain an accurate estimation of elastic constants, the results of two numerical analyses are averaged. These analyses include a "free" or laterally unconstrained boundary condition (BC1) and a "continuum" boundary condition (BC2). BC1 imposes uniform displacements corresponding to 1% uniaxial strain on the faces of the RVE perpendicular to the loading direction without friction; the (unloaded) faces parallel to the loading direction are traction free. BC2 imposes the same conditions on the faces perpendicular to the loading direction as shown in Table 4.2. However, the faces parallel to the loading direction are constrained to remain planar and parallel during deformation, thereby applying traction to the planar faces and simulating an interior domain "compatible with the surrounding material". This requires that resultant forces on the constrained faces must vanish such that $\int_0^a \int_0^a \sigma_z(x, y, a)dxdy = 0$ and $\int_0^a \int_0^a \sigma_x(a, y, z)dydz = 0$ where $a = y_{max}$.

Table 4.2: Summary of applied boundary conditions; Δ_x and Δ_z are unspecified lateral displacements determined by integral equations.

RVE face	**Boundary Condition 1 (BC1)**		**Boundary Condition 2 (BC2)**	
Top ($y = y_{max}$)	$u_y = -0.01(y_{max})$	$\tau_{xy} = \tau_{yz} = 0$	$u_y = -0.01(y_{max})$	$\tau_{xy} = \tau_{yz} = 0$
Bottom ($y = 0$)	$u_y = 0$	$\tau_{xy} = \tau_{yz} = 0$	$u_y = 0$	$\tau_{xy} = \tau_{yz} = 0$
Left ($x = 0$)	-	$\sigma_x = \tau_{xy} = \tau_{xz} = 0$	$u_x = +(\Delta_x)/2$	$\tau_{xy} = \tau_{xz} = 0$
Right ($x = x_{max}$)	-	$\sigma_x = \tau_{xy} = \tau_{xz} = 0$	$u_x = -(\Delta_x)/2$	$\tau_{xy} = \tau_{xz} = 0$
Front ($z = z_{max}$)	-	$\sigma_z = \tau_{xz} = \tau_{yz} = 0$	$u_z = +(\Delta_z)/2$	$\tau_{xz} = \tau_{yz} = 0$
Back ($z = 0$)	-	$\sigma_z = \tau_{xz} = \tau_{yz} = 0$	$u_z = -(\Delta_z)/2$	$\tau_{xz} = \tau_{yz} = 0$
Pore surfaces	Traction free: $t_x = t_y = t_z = 0$		Traction free: $t_x = t_y = t_z = 0$	

Model size/scaling factors

In their investigation of RVE size, Shen and Brinson demonstrated that it is possible to obtain accurate estimations of elastic constants for small RVEs with periodic microstructure and non-overlapping spherical inclusions. These researchers note that "…the effective moduli obtained by a finite size domain of over a length of only two sphere diameters can be close to those obtained by a domain of infinite length, within a few percent of error, even in cases of void inclusions." These minimal errors result from a proper selection of boundary conditions, BC1 and BC2, as well as the requirement that the microstructure is periodic. Figure 4.12 shows the periodicity of these RVEs and all RVE dimensions exceed the noted two-sphere limitation, validating the extension of the Shen and Brinson methodology to the current study.

The Shen and Brinson study concluded that these boundary conditions provide oppositely biased responses and that the mean of the individual simulations under these two boundary conditions approximate the continuum such that "a number of small models can obtain convergent results equivalent to larger models."

4.2.3 Selection of parameter values

The purpose of this study is to determine the optimal combination of unit cell parameters (pore radius and separation) to achieve a desired combination of mechanical properties, notably a predictable reduction in Young's modulus. While pore arrangements and loading conditions have been defined, an infinite number of combinations of pore size and separation dimension remain. Figure 4.8 shows that for a given r/L ratio (ψ), the largest value of volume porosity, and thus the greatest potential reduction in Young's modulus, is obtained with the FCC, HCP and BCC unit cell arrangements. As the minimum center-to-center pore dimension, $L = 2r + s$, depends on the thickness of the solid material separating the pores (i.e., pore separation, s), a minimum pore

separation of 500 µm was selected as current AM processes cannot consistently reproduce smaller geometric features. The desired porosity range was determined by estimating the effective modulus (E_{porous}/E_{solid}) needed for a Ti6Al4V implant to approximate the Young's modulus of cortical bone (~20 GPa). Given a Young's modulus for Ti alloy (E ~ 114 GPa), this effective modulus is approximately 0.20. Existing mechanical property-porosity relationships (Chapter 3 and Appendix A) suggest that the porosity needed for an effective modulus of 0.20 is in the range of 20-50%. While this effective modulus does not consider tensile or fatigue strength concerns, this porosity range is sufficient to define the limits of the study.

A minimum pore separation of 500 µm and pore radii of 1000 and 1800 µm yields microstructures with volume porosity values of 35-50%. Increasing the pore separation to 1000 µm while retaining the pore radii at 1000 and 1800 µm, expands the analysis to include microstructures with volume porosities of 20-35% and defines the subset of design parameter values for the FE study, as depicted in Figure 4.15.

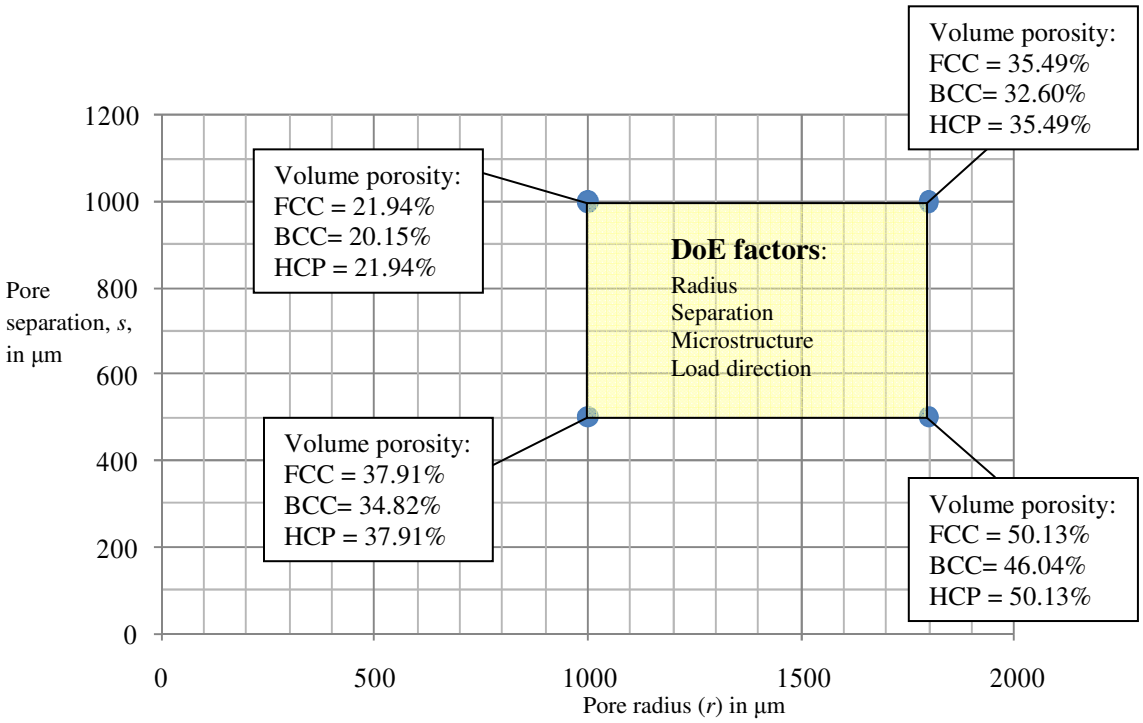

Figure 4.15: Details of design space for FE analyses

Given these pore size and fabrication constraints, the CAD models for each of the **three RVE designs** and the respective **loading conditions** were modified accordingly. The resulting pore size/separation combinations included 3 different pore arrangements (FCC, BCC, and HCP) and 3 different loading conditions for the cubic structures. The HCP unit cell structure was subject to 4 different loading conditions. These pore arrangements, size/separation parameters, and load orientations yielded a total of 40 FE simulations as summarized in Appendices B and C.

4.2.4 Estimation of moduli

As the desired output was as estimation of Young' modulus and Poison's ratio for the 40 RVEs, the FE method simulated a macroscopic stress condition in response to an applied strain of 1%. Mean values for internal stress and lateral displacement were derived from the FE analyses and used to calculate these mechanical properties.

The FE simulation applied a uniaxial y-displacement to the nodes of the top surface (at $y = y_{max}$) of the respective RVEs, assemblies of unit cells that incorporate a large number of spherical voids. The resulting stress distribution is macroscopically uniform. In the immediate vicinity of spherical pore, however, stresses are not uniform as indicated in Figure 4.16, the stress distribution at mid-plane ($y = y_{max}/2$) for a representative RVE model. The mean normal stress over a sufficiently large area, in this instance, across the mid-plane or the quarter plane ($y = y_{max}/4$) of the RVE, approximates the macroscopic uniform stress. Similarly, the strain distribution is nonuniform at the sub-RVE level but essentially uniform macroscopically. The normal strain component (parallel to the axis of applied displacement, ε_{yy}), averaged over a sufficiently large area, again approximates the macroscopic longitudinal strain. This strain, along with the calculation of the mean lateral strain (ε_{xx} and ε_{zz}) from the displacement of the nodes of the non-loaded faces ($x = 0$ and $x = x_{max}$, $z = 0$ and $z = z_{max}$) allows the calculation of a representative value for Poisson's ratio.

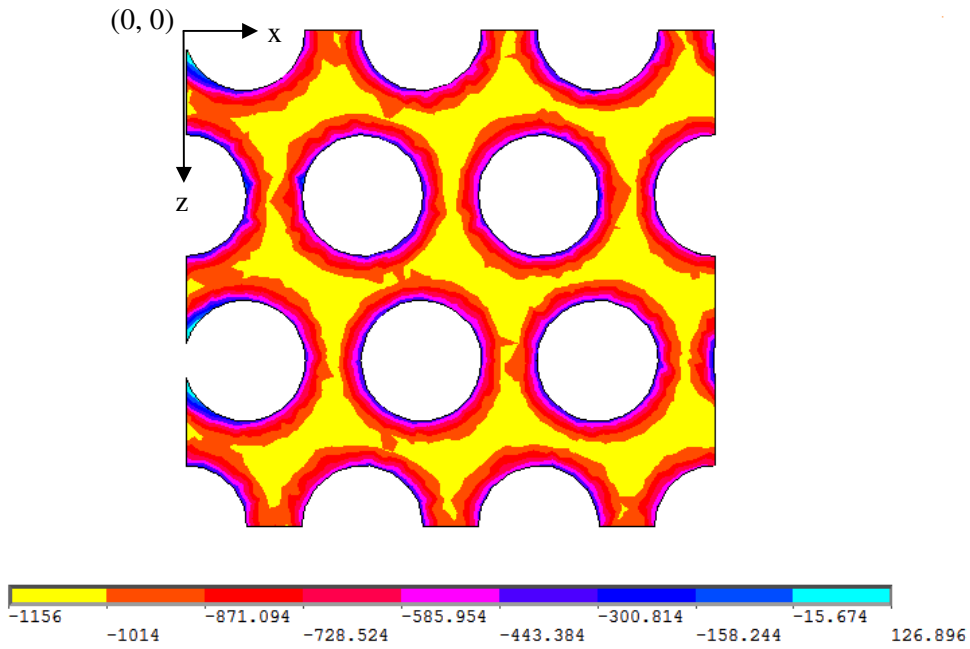

Figure 4.16: Representative RVE mid-plane ($y = y_{max}/2$) stress distribution (MPa) [1810B2a with BC1applied to RVE]

A comparison of the resulting values for Young's modulus and Poisson's ratio for different loading condition within a group of the same unit cell type (FCC, HCP or BCC) allows a confirmation of isotropy for a given microstructure.

In response to a simulated compressive strain, the average normal stress across both the mid- and quarter-planes of each RVE were determined and normalized for the differences in cross-sectional area. The ratio of average stresses across any two given planes perpendicular to the applied displacement is inversely proportional to the ratio of the corresponding area of those planes. As the applied strain for all RVEs was 1%, the mean normal stress values for the two planes was averaged and used to calculate the effective Young's modulus for a given RVE.

Displacements of the non-loaded (x and z) faces were obtained after those faces were constrained to remain planar as a result of the application of BC2 and the use of the

Coupling/Ceqn function within ANSYS. Lateral strain was calculated by summing the displacement of the respective non-loaded faces of the RVE and converting to strain by dividing by the initial RVE dimension, x_{max} or z_{max}. The ratio of the mean lateral strain and the longitudinal strain magnitudes were used to calculate the effective Poisson's ratio for each RVE.

4.2.5 Sensitivity of effective properties

Design of experiments (DoE) methods were applied to the FE results to investigate sensitivity of the effective mechanical properties to changes in microstructure and porosity. Minitab® 15 software (version 15.1.0.0, Minitab Inc., State College, Pennsylvania) was used for statistical analyses. An analysis of variance (ANOVA) procedure assessed the relative significance of the independent variables or factors (pore radius, separation, structure and load condition) on the effective Young's modulus and Poisson's ratio.

The alpha level for this statistical evaluation was set at 0.05, meaning that the probability of finding an effect that does not really exist is only 5%. Since the number and type of loading conditions on the cubic RVE structures (FCC and BCC) differed from those on the hexagonal prism (HCP) as noted in Appendix B, two separate ANOVA calculations were required.

The initial study design specified pore radii/separation parameters that were realistic in terms of current AM capabilities and bracketed the volume porosity range (20-50%) most likely to be of clinical significance. To assess the effect of these variables between these limits, variations in parameter values within the initial design space were considered. While typical DoE procedures would select parameter values at the center of the previously defined design space, i.e., a pore radius of 1400 μm and a pore separation of 750 μm, any pore separation in excess of the minimum achievable pore spacing reduces porosity and increases the effective Young's

moduli. Accordingly, study refinements focused on the effect of changes in microstructure and pore radius on Young's modulus and Poisson's ratio at the minimum pore spacing of 500 μm.

To determine which pore arrangement yields the lowest modulus for a given porosity, the pore radii required to produce a volume porosity of 42 and 44 % were calculated for each of the three pore arrangements (FCC, BCC and HCP). The previous 40 FE analyses compared different microstructures at the same ψ ratio, not at the same porosity level. Analyses at these mid-range values of 42 and 44% volume porosity also augmented the available data as previous FE simulations had pore radii that yielded porosities of either $< 38\%$ or $> 46\%$. For each pore arrangement, the loading condition that resulted in minimum values for Young's moduli in the previous 40 simulations was applied. This included loading on the faces of the cubic structures (FCC and BCC) and loading on the hexagonal edge of the HCP structure. Due to the geometric similarities between the FCC and HCP unit cells, as described in 4.2.1, loading on the hexagonal edge of the HCP unit cell is approximately equivalent to face loading on the FCC unit cell.

The design parameters of these six prescribed porosity models, all with a uniform pore separation of 500 μm, are summarized in Table 4.3. RVE designations are noted for reference to the FE results summarized in Appendix D.

Table 4.3: Design parameters for specific porosity values

RVE designation	Pore radius (μm)	Separation distance (μm)	Volume porosity	r/L (ψ)	Pore arrangement
1205A1	1200	500	42.0%	0.4138	FCC
1325A1	1320	500	44.0%	0.4204	FCC
1445C1	1440	500	42.1%	0.4260	BCC
1605C1	1600	500	44.0%	0.4324	BCC
1205B5a	1200	500	42.0%	0.4138	HCP
1325B5a	1320	500	44.0%	0.4204	HCP

While these analyses at 42 and 44% volume porosity expanded the data for a fixed pore separation of 500 μm, an additional seven FE simulations were conducted to obtain stress and strain values for an expanded range of ψ ratios, as noted in Table 4.4. These additional FE analyses further defined the functional dependence of the dominant variable(s) for a given microstructure and facilitated quantification of the sensitivity of the effective mechanical properties to changes in those variables.

Table 4.4: Design parameters for varying values of ψ
(* included in the initial set of FE analyses)

RVE designation	Pore radius (μm)	Separation distance (μm)	Volume porosity	r/L (ψ)	Pore arrangement
7925A1	792	500	32.5%	0.3800	FCC
8865A1	886	500	35.1%	0.3900	FCC
105A1*	1000	500	37.9%	0.4000	FCC
1145A1	1140	500	40.8%	0.4101	FCC
1325A1	1320	500	44.0%	0.4204	FCC
1545A1	1536	500	47.1%	0.4300	FCC
185A1*	1800	500	50.1%	0.4390	FCC
2255A1	2250	500	54.0%	0.4500	FCC
2875A1	2875	500	57.7%	0.4600	FCC

4.3 Results

The effective Young's moduli (normalized with respect to that for solid T16Al4V) for the initial 40 FE analyses and the supplemental 13 porosity models are summarized as a function of ψ and volume porosity in Figures 4.17 and 4.18. All regression lines for Young's modulus as a function of ψ fall within the band defined by those of RVEs *A1* and *C1* in Figure 4.17. The results for Poisson's ratio shown in Figure 4.18 are banded by the regression lines for RVEs *A1* and *C3*.

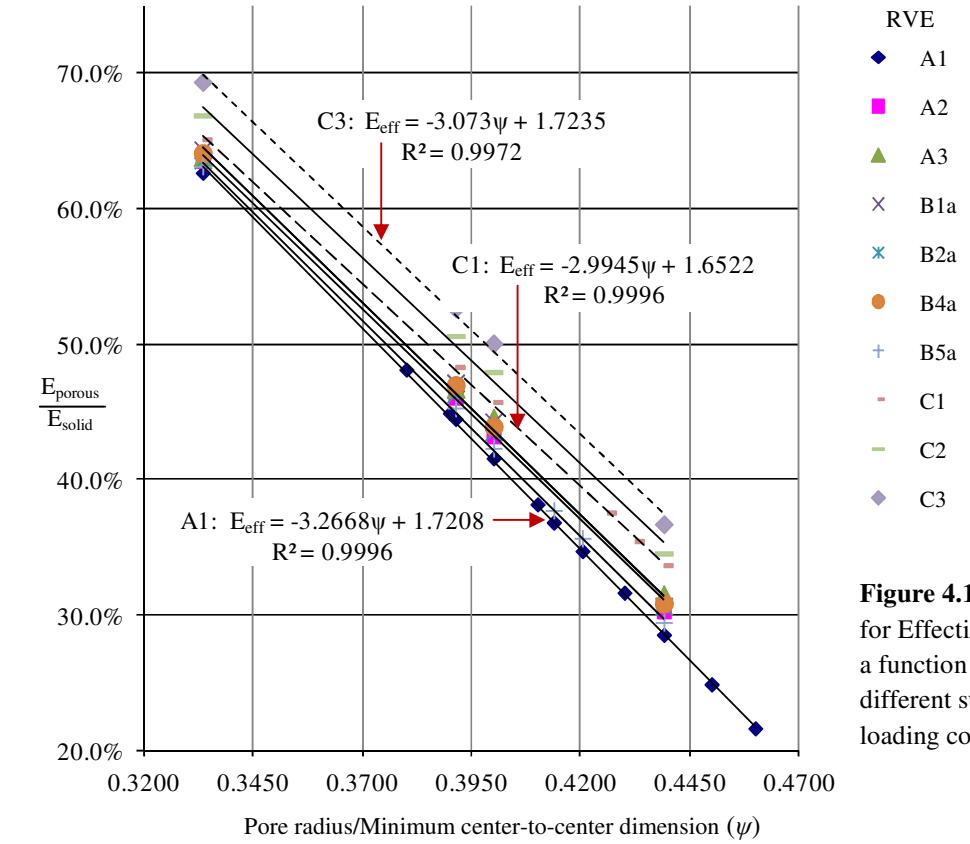

Figure 4.17: FEA Data for Effective Modulus as a function of ψ for different structures and loading conditions

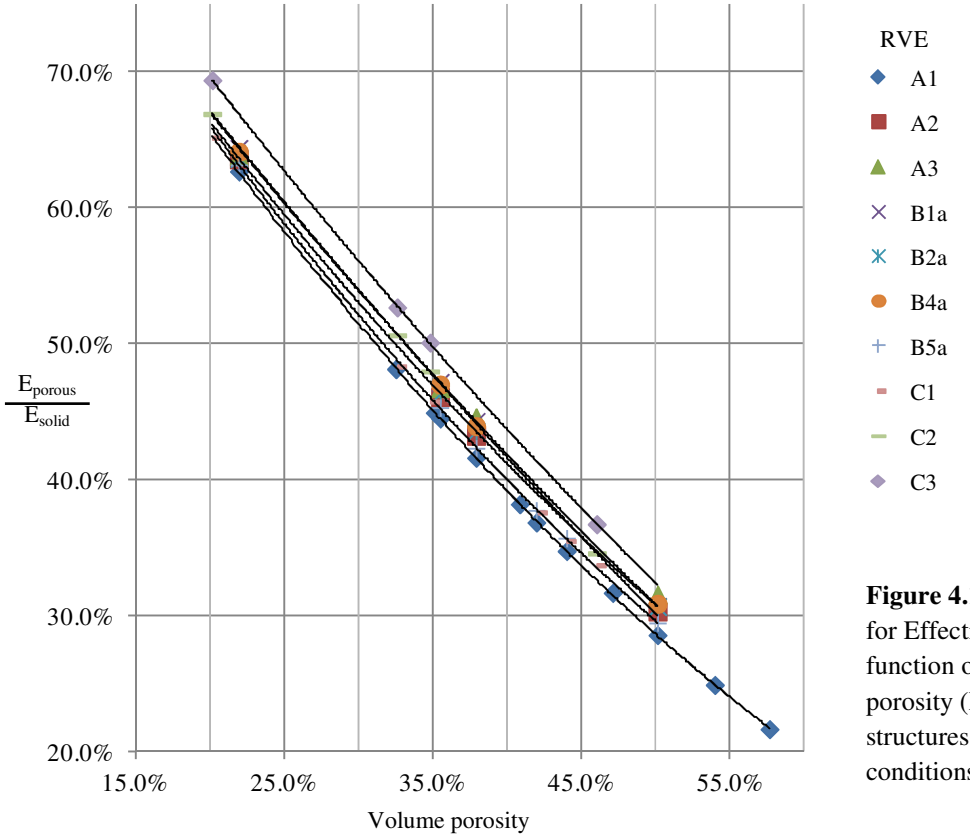

Figure 4.18: FEA Data for Effective Modulus a function of volume porosity (P) for different structures and loading conditions

As seen in these figures, the effective Young's modulus varies linearly with ψ. The data designation *A* refers to the FCC unit cell, *B* to the HCP unit cell and *C*, the BCC unit cell in all figures. The numerical designation refers to the loading conditions described in section 4.2.1 and the resulting RVEs shown in Figure 4.12.

An analysis of variance (ANOVA) creates a meta-model of the relationship between all factors that have a statistically significant ($P \leq 0.05$) effect on the estimation of Young's modulus and provides an indication of the coherence of the data. The FE data and the general linear ANOVA model for effective Young's modulus are compared in Figure 4.19, with the ANOVA results indicated by the *AA* and *AC* designation. *AA* refers to the ANOVA results for the FCC unit cell; *AC* denotes the ANOVA results for the BCC unit cell.

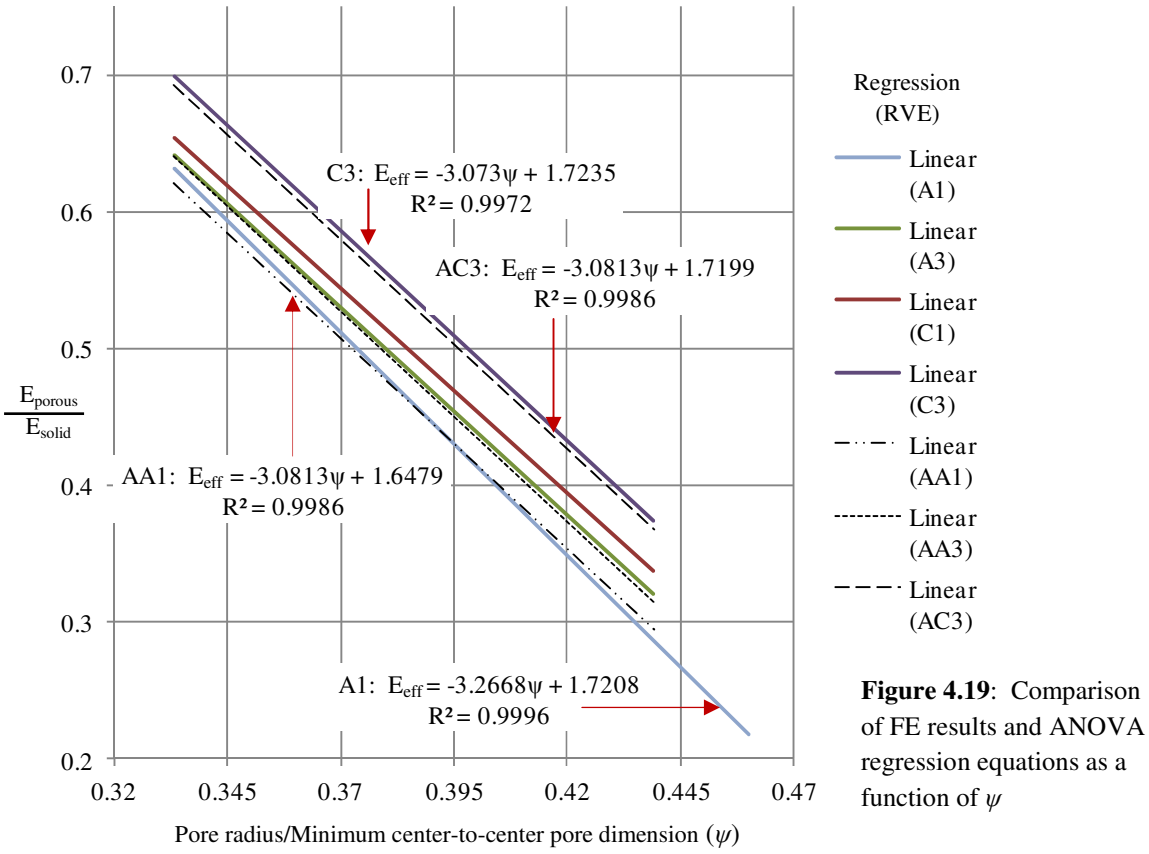

Figure 4.19: Comparison of FE results and ANOVA regression equations as a function of ψ

All four factors (radius, pore separation, structure and load direction) have significant effects ($P < 0.05$) on Young's modulus for the cubic (FCC and BCC) unit cells. As radius and pore separation have the largest values for the F-statistic ($F_{radius} = 6368.1$, $F_{separation} = 8781.0$, $F_{structure} = 585.3$, $F_{load} = 93.8$), they have the greatest effect on Young's modulus. ANOVA results for the hexagonal structure (HCP) indicate that radius, separation and load condition have significant ($P < 0.05$) effects on Young's modulus, although load, due to its small F-statistic value ($F_{radius} = 5738.5$, $F_{separation} = 8103.6$, $F_{load} = 20.5$), has a lesser effect than the other two factors.

The Poisson's ratio data for the initial 40 FE analyses and supplemental 13 porosity models are summarized as function of ψ and volume porosity in Figures 4.20 and 4.21.

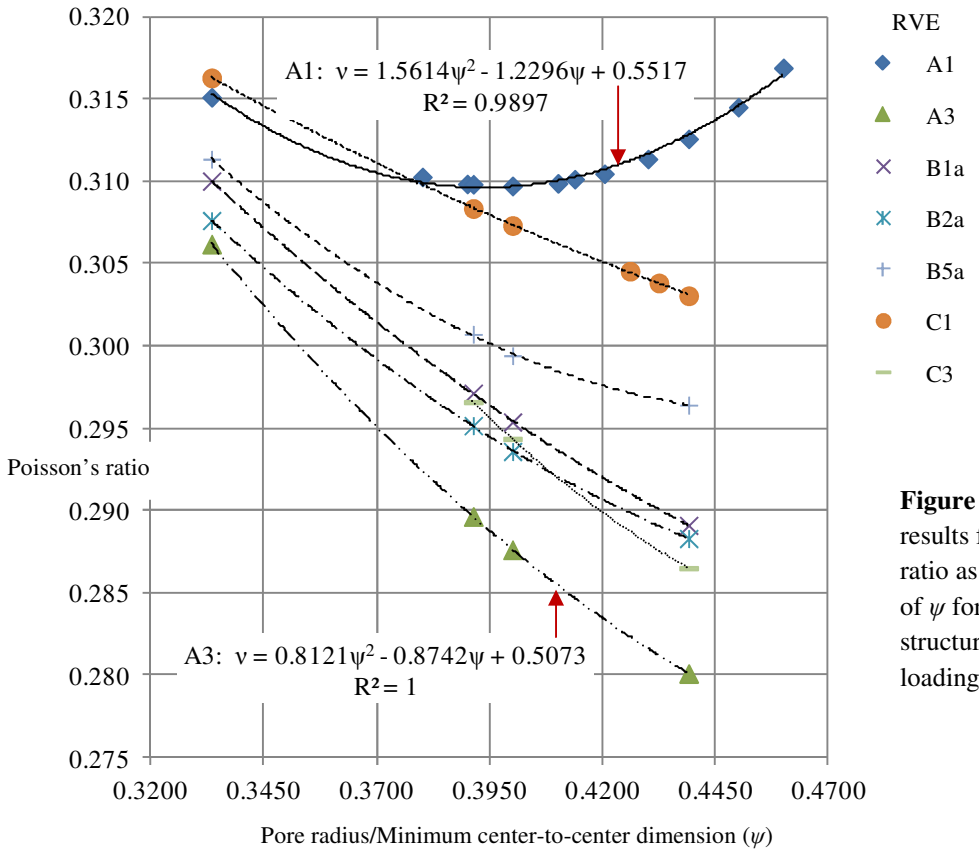

Figure 4.20: FE results for Poisson's ratio as a function of ψ for different structures and loading conditions

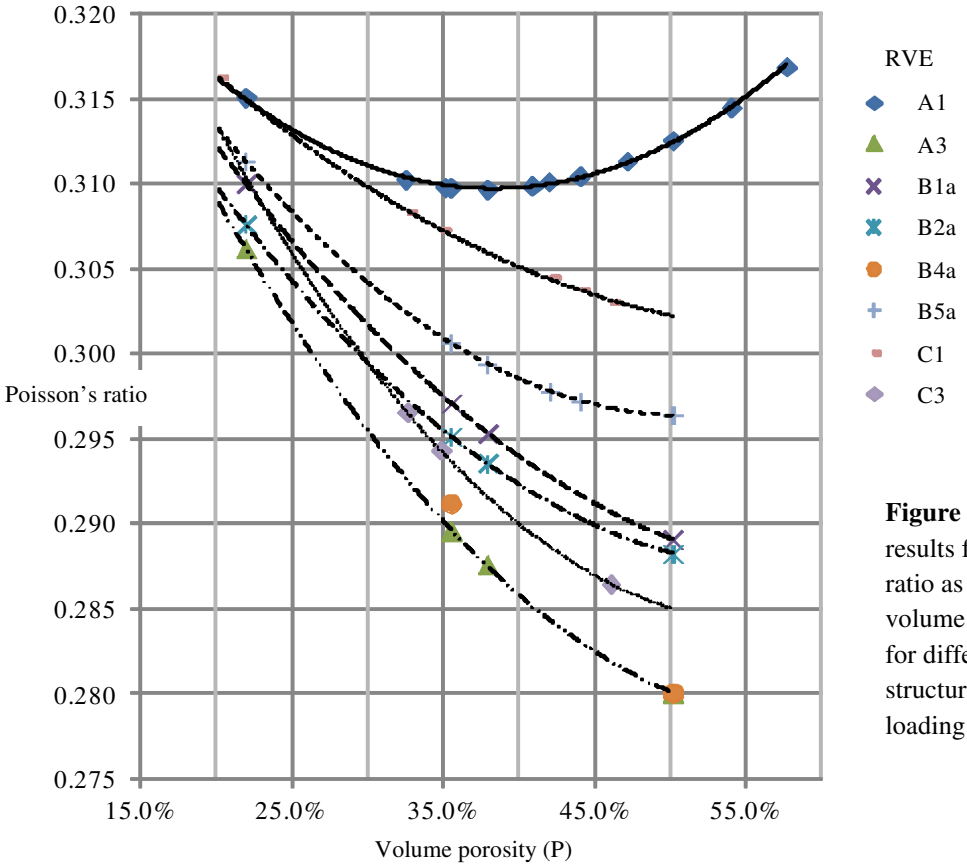

Figure 4.21: FE results for Poisson's ratio as a function of volume porosity (P) for different structures and loading conditions

In this study, the relationship between Poisson's ratio and ψ and volume porosity appears second order. The regression equations for RVEs *A1* and *A3* represent the upper and lower bounds of the relationship with the results for both the BCC cubic structure (*C1*, *C2* and *C3*) and the HCP structure (*B1a*, *B2a* and *B5a*) falling between these bounds.

The data shown in Figures 4.17 and 4.18 suggest that the microstructures evaluated in this study do not exhibit isotropic behavior, as would be evident if Young's modulus for a given porous structure could be represented by a single equation for all loading conditions. These data show that the response of a specific microstructure changes as the direction of the applied load is varied.

Tables 4.5, 4.6 and 4.7 summarize the effective Young's modulus determined by the regression equations for the FE data. For a given ψ ratio, the variation in effective Young's modulus, Δ, is the difference between the largest and smallest values of effective modulus divided by the smallest value for that ψ and pore structure.

Table 4.5: Comparison of effective Young's modulus vs. load direction for **FCC** unit cells

		Effective Modulus for a given Load Condition for FCC (A) Structure			
ψ ratio	**Porosity**	**Load Condition 1**	**Load Condition 2**	**Load Condition 3**	**Δ**
0.333	21.9%	63.2%	63.9%	64.2%	1.6%
0.391	35.5%	44.3%	45.7%	46.6%	5.2%
0.400	37.9%	41.4%	42.9%	43.9%	6.0%
0.439	50.1%	28.7%	30.7%	32.1%	11.8%

Table 4.6: Comparison of effective Young's modulus vs. load direction for **BCC** unit cells

		Effective Modulus for a given Load Condition for BCC (C) Structure			
ψ ratio	**Porosity**	**Load Condition 1**	**Load Condition 2**	**Load Condition 3**	**Δ**
0.333	20.2%	65.4%	69.9%	69.9%	6.9%
0.391	32.6%	48.0%	52.1%	52.1%	8.5%
0.400	34.8%	45.4%	49.4%	49.4%	8.8%
0.439	46.0%	33.8%	37.4%	37.4%	10.7%

Table 4.7: Comparison of effective Young's modulus vs. load direction for HCP unit cells

		Effective Modulus for a given Load Condition for HCP (B) Structure			
ψ ratio	**Porosity**	**Load Condition 1a**	**Load Condition 2a**	**Load Condition 5a**	**Δ**
0.333	21.9%	64.9%	64.0%	63.4%	2.4%
0.391	35.5%	46.5%	45.9%	44.9%	3.6%
0.400	37.9%	43.8%	43.2%	42.2%	3.8%
0.439	50.1%	31.4%	31.1%	29.7%	5.7%

The aforementioned anisotropic behavior relative to effective Young's moduli is also evident in the data for Poisson's ratio as shown in Tables 4.8, 4.9 and 4.10. The variation in effective Poisson's ratio, Δ, is the difference between the largest and smallest values of Poisson's ratio for a given ψ divided by the smallest value for that ψ and pore structure.

Table 4.8: Comparison of Poisson's ratio vs. load condition for FCC unit cells

		Poisson's Ratio for a given Load Condition for FCC (A) Structure			
ψ ratio	**Porosity**	**Load Condition 1**	**Load Condition 2**	**Load Condition 3**	**Δ**
0.333	21.9%	0.315	0.310	0.306	2.9%
0.391	35.5%	0.310	0.298	0.290	6.9%
0.400	37.9%	0.310	0.297	0.288	7.1%
0.439	50.1%	0.313	0.293	0.280	10.5%

Table 4.9: Comparison of Poisson's ratio vs. load condition for BCC unit cells

		Poisson's Ratio for a given Load Condition for BCC (C) Structure			
ψ ratio	**Porosity**	**Load Condition 1**	**Load Condition 2**	**Load Condition 3**	**Δ**
0.333	20.2%	0.316	0.311	0.316	1.7%
0.391	32.6%	0.308	0.299	0.297	3.8%
0.400	34.8%	0.307	0.298	0.294	4.2%
0.439	46.0%	0.303	0.293	0.286	5.5%

Table 4.10: Comparison of Poisson's ratio vs. load condition for HCP unit cells

		Poisson's Ratio for a given Load Condition for HCP (B) Structure			
ψ ratio	**Porosity**	**Load Condition 1a**	**Load Condition 2a**	**Load Condition 5a**	**Δ**
0.333	21.9%	0.310	0.308	0.311	1.2%
0.391	35.5%	0.297	0.295	0.301	1.8%
0.400	37.9%	0.295	0.294	0.299	2.0%
0.439	50.1%	0.289	0.288	0.296	2.7%

The equations resulting from the regression analysis of the FE data for Young's modulus and Poisson's ratio are summarized in Table 4.11.

Table 4.11: Equations for effective moduli as a function of ψ

Structure	$E_{eff} = f(\psi)$	$\nu = f(\psi)$ for Ti6Al4V	Porosity = $f(\psi)$
A1	$-3.267\psi + 1.721$	$1.561\psi^2 - 1.230\psi + 0.552$	$5.924\ \psi^3$
A2	$-3.141\psi + 1.686$	$0.860\psi^2 - 0.826\psi + 0.490$	$5.924\ \psi^3$
A3	$-3.039\psi + 1.655$	$0.812\psi^2 - 0.874\psi + 0.507$	$5.924\ \psi^3$
B1a	$-3.173\psi + 1.707$	$0.531\psi^2 - 0.608\psi + 0.454$	$5.924\ \psi^3$
B2a	$-3.112\psi + 1.677$	$0.689\psi^2 - 0.715\psi + 0.469$	$5.924\ \psi^3$
B4a	insufficient data	insufficient data	$5.924\ \psi^3$
B5a	$-3.185\psi + 1.696$	$0.921\psi^2 - 0.853\psi + 0.493$	$5.924\ \psi^3$
C1	$-2.995\psi + 1.652$	$0.250\psi^2 - 0.318\psi + 0.394$	$5.441\ \psi^3$
C2	$-3.039\psi + 1.688$	$0.929\psi^2 - 0.884\psi + 0.503$	$5.441\ \psi^3$
C3	$-3.073\psi + 1.724$	$1.168\psi^2 - 1.182\psi + 0.580$	$5.441\ \psi^3$

4.4 Discussion

The initial phase of this FE study considered three different microstructures with a common set of ψ ratios and their response to a uniform compressive strain of 1%. Two different global boundary conditions (BC1 and BC2) were applied and the results averaged to obtain an approximation of Young's modulus and Poisson's ratio for a continuum of porous material with a given microstructure.

Convergence testing of the FE results involved varying the SmartSize level setting in ANSYS' Mechanical APDL until visual discontinuities between elements became small and a comparison of nodal versus element data for calculated stresses showed approximately equal values. A comparison of values for average stress across quarter- and mid-planes within the RVEs perpendicular to the applied deformation showed a difference of less than 0.02% between

the results obtained at SmartSize level 3 compared to those for a finer mesh, SmartSize level 2. The percentage difference between calculated stresses with a coarser mesh, SmartSize level 4, versus those obtained for a finer mesh, SmartSize level 3, was 1.1%. As these data confirmed convergence of the calculated stress levels, a SmartSize level setting of 3 was used for all FE analyses, unless otherwise noted.

While the FE software allows the import of CAD files in various formats, efforts to import the solid geometry of some RVEs were hindered by the apparent inability of ANSYS' Mechanical APDL (version 12.0.1) to read files saved in IGES version 5.3, the most recent format. Furthermore, this version of ANSYS was unable to import some RVE geometries due to an inability to properly recognize features created in SolidWorks through the use of Boolean operations. The difference may be inconsequential in other situations, but several combinations of pore radius, separation and load condition could not be imported accurately.

Young's Modulus

The FE analyses confirm the inverse relationship between Young's modulus and the ratio ψ and volume porosity, a third-order function of ψ. The relationship with ψ is well described ($R^2 > 0.99$) by linear regression equations for each of the three unit cell types. As noted in Figure 4.17, these best-fit lines for effective Young's modulus as a function of ψ for each unit cell type have similar, but not identical slopes, and differ primarily in their y-intercept. The regression lines are tightly grouped for the FCC (A) and HCP (B) unit cells, reflecting their similar geometric structures. As the BCC (C) structure has a lesser volume porosity for a given value of ψ, the regression equations for this structure predict larger values for Young's modulus than either the FCC or HCP structures at that same ψ ratio.

The *A1* data in Figure 4.18 (FCC: load condition 1) suggest that a second order equation may approximate the results for Young's modulus as function of volume porsity. Substitution of the third-order equation for porsity as a function of ψ (Table 4.11) does yield a curve that can be represented by a second-order function of *P* over the porosity range (20-50%) covered in this study. However, from the prespective of potential applications to orthopaedic implant design, the physical significance of the ratio ψ may be more useful.

If each of these structures (FCC, HCP and BCC) exhibited isotropic behavior, it would be expected that the mechanical property data, irrespective of load condition, would fall onto one of three regression lines represented by the three different structures considered in this study. The results show that there is a variation in the FE prediction of Young's modulus for each structure due to changes in the load direction. These differences in effective Young's moduli calculated from the regression equations as the load direction varied is summarized in Table 4.5for the **FCC** microstructure. This variation in the effective Young's modulus with load was apparent at all ψ levels and values of volume porosity. These data indicate that the **determination of Young's modulus is affected by direction of applied load** and that porous microstructures of the type evaluated in this study are not isotropic. The results summarized in Table 4.5 further demonstrate that for these microstructures, the anisotropic behavior of the porous material appears to become more pronounced as values of the ψ ratio or volume porosity increase.

The **BCC** structure shows similar anisotropic behavior with load direction (Table 4.6), although the increase in anisotropy as ψ increases is not as great as that of the FCC structure. However, as the FE software was unable to mesh the BCC structure at the lowest porosity or ψ level, this assessment requires further investigation.

Young's modulus also varied with load direction for the **HCP** structure (Table 4.7), with the anisotropy again increasing with larger values of ψ. However, this anisotropy is not as large

as that observed for the cubic unit cells. In that geometric similarities exist between the FCC and HCP structure, greater anisotropy was anticipated. Further analysis of the HCP structure over an expanded range of volume porosity and ψ values is needed to evaluate this non-intuitive result.

All data indicate that, regardless of a specific ψ value or the volume porosity of the microstructure, **loading on the face of the FCC structure (load condition 1) consistently yields the lowest value for Young's modulus**. This result suggests that the fabrication of prototypical implant segment should utilize this loading orientation and microstructure to obtain moduli that offer the greatest potential for reduction in bone resorption.

The FE data and the resulting regression equations allow the comparison of Young's moduli so as to evaluate the effect of microstructural differences on mechanical properties. Recall that porosity is a third-order function of ψ (Table 4.11), itself a ratio of two independent variables, pore radius and pore separation. Both of these variables were determined to have a statistically significant effect on moduli when considered individually. Because these variables are now combined in a single variable, ψ, their earlier statistical significance is no longer valid. To minimize the interaction of loading direction on differences due to microstructure, only the regressions associated with load condition 1(loading on the faces of the FCC and BCC units cells) and load condition 5a (loading on the hexagonal edge of the HCP unit cell) are compared. Similarities in pore arrangement and orientation between the FCC and HCP unit cells under these two loading conditions allow a valid comparison of these two structures.

To illustrate the microstructural differences in mechanical properties, the second-order regression equations for the above models and given load conditions are contrasted in Figure 4.22. The data indicate that **the differences in predicted Young's moduli with changes in microstructure are small, with an average difference of approximately 2.5% across a range of 20-50% volume porosity**. Table 4.12 summarizes the results and shows that using either a

first- or second-order regression for a comparison of effective modulus has little effect on this result. The difference in Young's moduli prediction between first- and second-order equations, using the same data, is small (0.6% at 30% porosity for the FCC structure).

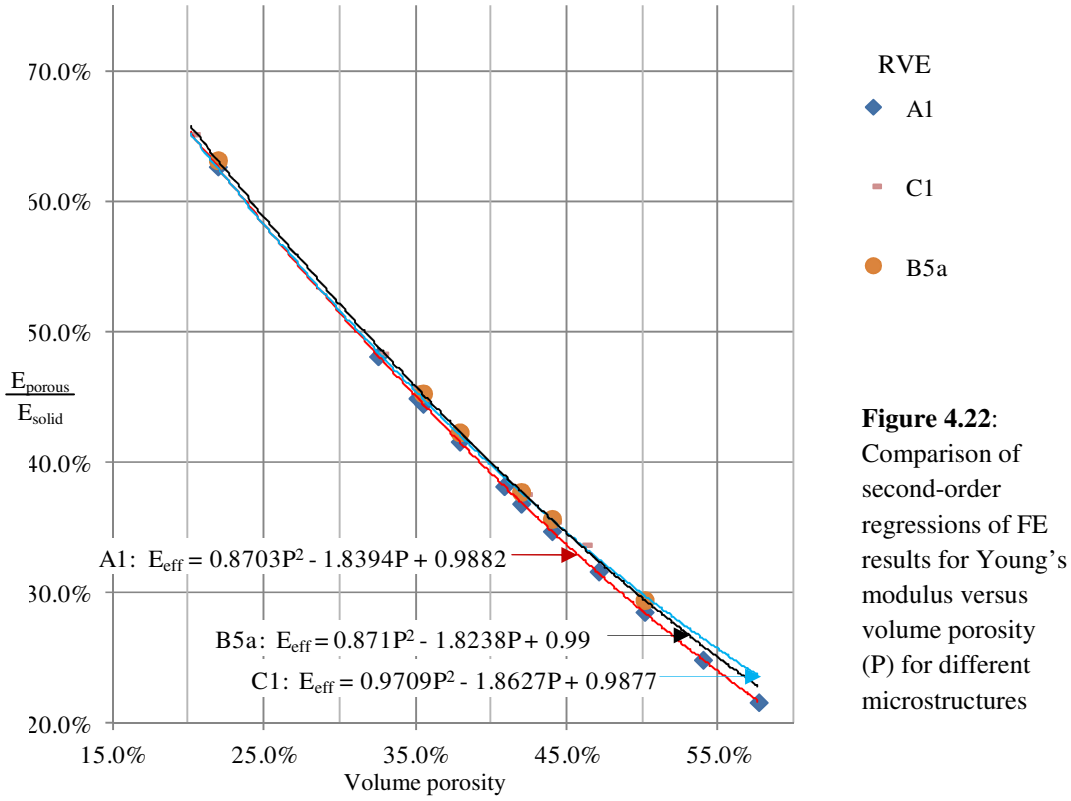

Figure 4.22: Comparison of second-order regressions of FE results for Young's modulus versus volume porosity (P) for different microstructures

Table 4.12: Differences in effective Young's modulus with microstructure (FCC, BCC and HCP)

Regression		**Young's Modulus versus Porosity for different microstructures**			
	Porosity	**FCC (A1)**	**BCC (C1)**	**HCP (B5a)**	**Δ**
First-order Equation	20.0%	62.6%	64.6%	64.7%	3.37%
	35.0%	45.6%	46.3%	46.6%	2.16%
	50.0%	28.6%	28.1%	28.5%	2.10%
Second-order Equation	20.0%	65.5%	65.4%	66.0%	0.93%
	35.0%	45.1%	45.5%	45.8%	1.63%
	50.0%	28.6%	29.9%	29.6%	4.54%
				Average	2.46%

Comparing the effects of loading condition 2 on FCC and BCC microstructures showed similar small differences (less than 2.5 %) in effective Young's modulus. As a consequence, **these results suggest that microstructure (FCC, HCP or BCC) has little effect on the resulting Young's modulus** over a porosity range of 20-50%.

Poisson's Ratio

Poisson's ratio for all RVEs was determined by applying BC2, constraining all non-loaded faces to remain planar and parallel during deformation. For a given RVE axis, the absolute value of transverse displacement for each non-loaded face was summed and used to calculate the transverse strain along that axis. Transverse strain for the second non-loaded RVE axis was similarly evaluated. The mean transverse strain was then used to calculate Poisson's ratio for the given RVE. The FE analyses simulated use of Ti6Al4V (Poisson's ratio of 0.342) and all FE results (y-axis of Figures 4.20, 4.21 and 4.23) reflect this material property assignment.

It is important to note that the FE results and the use of the associated regression equations for *A2* (FCC structure, load condition 2) and *C2* (BCC structure, load condition 2) are applied with some caution as the transverse strain values used to estimate the Poisson's ratio, as listed in Appendix D, differed by more than 20% and that while the resulting Poisson's ratios fell into the appropriate range, further investigation is needed to confirm the accuracy of these estimates. The large differences in transverse strain were due to the geometric asymmetry of the RVE resulting from loading along the diametrically opposing edges of the FCC and BCC unit cells. Additional FE analyses utilizing larger RVEs, which necessarily incorporate more unit cells and reduce the effect of this asymmetry, may reduce the differences in transverse strain between the non-loaded faces of the RVE for this loading condition.

As the effect of porosity on Poisson's ratio has not been studied as extensively as that of Young's modulus and presenting data as a normalized or effective Poisson's ratio (i.e., ν_{porous}/ν_{solid}), as done for the effective Young's modulus, may be misleading, the results for Poisson's ratio may only be valid for Ti6Al4V or related titanium alloys.

As noted in Figures 4.20 and 4.21, the FE data show that Poisson's ratio changes as porosity or ψ values increase. Second-order regressions adequately describe the relationship between ψ and Poisson's ratio as the regression equations account for more than 98% of the variation in the analysis. As in the case of Young's modulus, substitution of the third-order equations for porsity as a function of ψ (Table 4.11) yields curves that can be represented by a second-order function of *P* over the porosity range (20-50%) covered in this study.

Tables 4.7, 4.8 and 4.9 summarize the results for Poisson's ratio for the FCC, BCC and HCP microstructures and indicate the extent of anisotropy in a given microstructure as a function of load condition. While the change in Poisson's ratio for the **BCC** structure was only about half that of the FCC structure for the same ψ ratio, the FE software was unable to mesh the BCC structure at the lowest porosity or ψ level indicating that this observation requires further investigation.

The resulting variation in Poisson's ratio for the **HCP** structure is much smaller than either that of the FCC or BCC structures. While this result is similar to the variability of Young's modulus for same structure, geometric similarities suggest that changes in Poisson's ratio with porosity for the HCP structure should be comparable to that of the FCC structure. This again suggests that further analysis of the HCP structure over an expanded ψ or porosity range is needed.

The effect of microstructure on Poisson's ratio is characterized by a large variation in the respective values for Poisson's ratio at all values of porosity for a given structure, a sensitivity to change as porosity or ψ values increase and the apparent development of a local minimum as porosity increases. As shown in Figures 4.20 and 4.21, the porosity at which this minimum occurs is clearly dependent upon the particular microstructure.

To better illustrate changes in mechanical properties with microstructure, second-order regression equations for Poisson's ratio as a function of volume porosity are contrasted in Figure 4.23. As in the analysis of Young's modulus, only the regressions associated with load condition 1 (loading on the faces of the FCC and BCC units cells) were compared along with load condition 5a (loading on the hexagonal edge of the HCP unit cell). These FE models and data facilitate the comparison and minimize the dependence of loading direction. As before, the intrinsic geometric similarities between the FCC and HCP unit cells under these two loading conditions allows a valid comparison Poisson's ratio data for of all three structures.

Since initial FE results suggested that the FCC (A) structure had the greatest potential for manipulating the effective modulus to achieve a desired clinical result, additional analyses were conducted to expand the porosity range for this microstructure (*A1*) as noted in Figures 4.20, 4.21 and 4.23). These additional data helped identify the minimum in Poisson's ratio at approximately 37% porosity.

The regression equations describing the other two microstructures (HCP and BCC) also reflect potential minima. The regression equation for the HCP structure (*B5a*) suggests a minimum value for Poisson's ratio occurring at approximately 50% porosity.

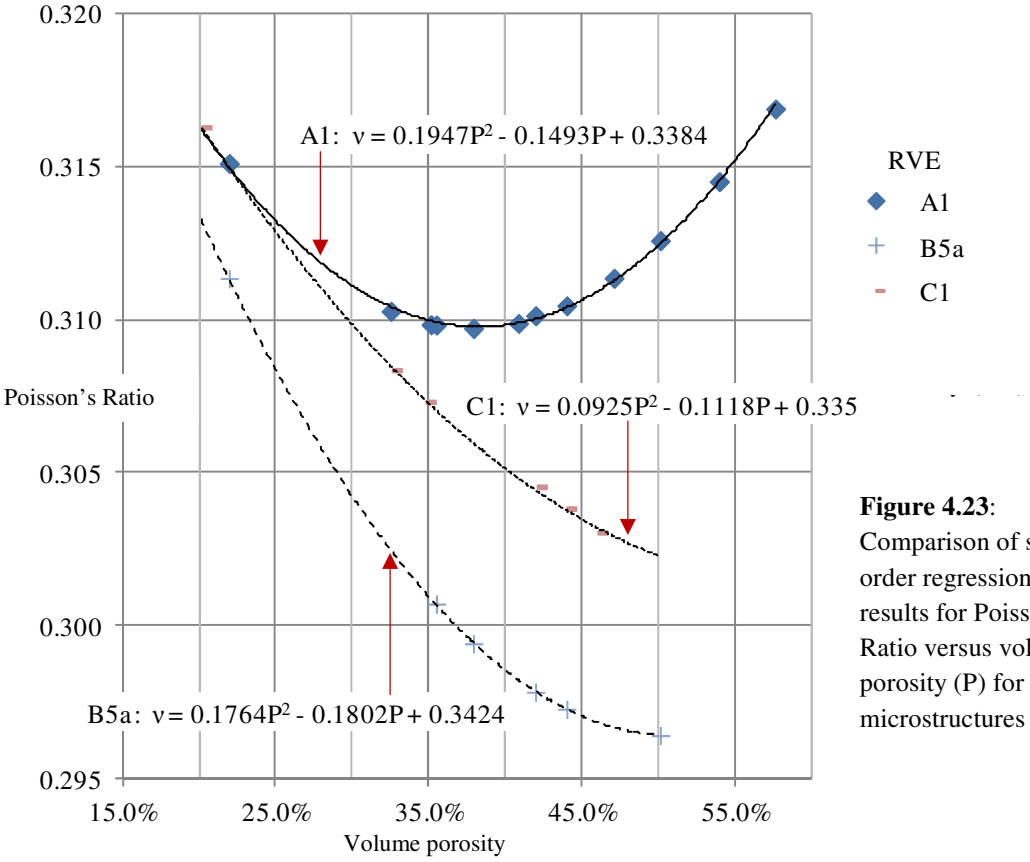

Figure 4.23: Comparison of second-order regressions of FE results for Poisson's Ratio versus volume porosity (P) for different microstructures

To place this variability in local minima between FCC and HCP microstructures in context, minimum and maximum (and variation, Δ) in Poisson's ratios predicted by the FE model results for the various microstructures are summarized in Table 4.13. In comparison to the Poisson's ratio for Ti6Al4V (ν = 0.342), Poisson's ratio is reduced to about 90 ± 3% of that of the non-porous material and the value of Poisson's ratio varies no more than about 5% across a range of 20-50% volume porosity. Further investigation is needed to confirm whether a minimum Poisson's ratio exists for the HCP and BCC microstructures.

Table 4.13: Variation in effective Poisson's ratio (PR) vs. microstructure (re: Ti6Al4V)

Structure	Minimum PR	% Ti6Al4V	Maximum PR	% Ti6Al4V	Δ
A1 (FCC)	0.309	90.4%	0.317	92.7%	2.3%
B5a (HCP)	0.2965	86.7%	0.313	91.5%	4.8%
C1 (BCC)	0.3025	88.5%	0.316	92.4%	3.9%

4.5 Conclusions

In summary, these results show that porous structures do not exhibit isotropic behavior and the degree of anisotropy is a function of porosity, becoming increasing anisotropic as the porosity or ψ value increases. This change in anisotropic behavior as ψ or porosity increases is evident for both Young's modulus and Poisson' ratio.

The data also show that the selection of microstructure (FCC, HCP, or BCC) has only a minimal effect on the resulting Young's modulus. However, different microstructures subjected to identical loading conditions yield measurably different results for Poisson's ratio.

This study also demonstrated that the FCC structure consistently yields the lowest value for Young' modulus irrespective of loading conditions or porosity level and that a linear relationship exists between ψ and the effective Young's modulus for a given microstructure. These linear relationships differ primarily in their intercept rather than their slope and show that the mechanical properties of porous constructs can be tailored with the appropriate selection of orientation to the applied load, microstructure (in the case of Poisson's ratio only) and porosity or ψ level.

The linear relationship between the effective Young's modulus and ψ is robust, with all of the respective microstructures described by regression equations having a coefficient of determination (R^2) greater than 0.99. A second order equation defines the relationship between ψ and Poisson's ratio for a given microstructure but the variation in Poisson's ratio as porosity and ψ increase for structures other than the FCC requires further investigation.

Finally, the data indicate that a prototypical structure incorporating 30% engineered porosity and appropriate load orientation can attain approximately a 50% reduction in effective Young's modulus. These results suggest that an appreciable reduction in flexural rigidity can be

achieved and application of these concepts and equations (once validated) is relevant to the design of orthopaedic implants.

4.6 References

[1] Rice, R.W., *Evaluation and extension of physical property-porosity models based on minimum solid area*, Journal of Materials Science, Vol. 31, pp. 102-118, 1996.

[2] Knudsen, F.P., D*ependence of Mechanical Strength of Brittle Polycrystalline Specimens on Porosity and Grain Size*, Journal of The American Ceramic Society, Vol.; 42, No. 8, pp. 376-387, 1959.

[3] Cannillo, V., Leonelli, C., Manfredini, T., Montorsi, M., Boccaccini, A.R., *Computational Simulations for the Assessment of the Mechanical Properties of Glass with Controlled Porosity*, Journal of Porous Materials, Vol. 10, pp.189-200, 2003.

[4] Cumberland, D.J., Crawford, R.J., *The Packing of Particles*, pp. 9-19, Elsevier, Amsterdam, 1987.

[5] Rice, R.W., *Microstructure Dependence of Mechanical Behavior of Ceramics*, Treatise on Material Science, Vol. 11, pp. 199-381, Academic Press, New York, 1977.

[6] Ryan, G., Pandit, A., Apatsidis, D.P., *Fabrication methods of porous metals for use in orthopaedic applications*, Biomaterials, Vol. 27, No. 13, pp. 2651-2670, 2006.

[7] Huiskes, R., Weinans, H., Dalstra, M., *Adaptive Bone Remodeling and Biomechanical Design Considerations for Noncemented Total Hip Arthroplasty*, Orthopedics, Vol. 12, No. 9, pp. 1255-1267, 1989.

[8] Collins, E.W., *Materials Properties Handbook: Titanium Alloys*, ASM International, December, 1995.

[9] Shen, H., Brinson, L.C., *A Numerical Investigation of the Effect of Boundary Conditions and Representative Volume Element Size for Porous Titanium*, Journal of Mechanics of Materials and Structures, Vol. 1, No. 7, pp. 1179-1204, 2006.

[10] Bobyn, Mortimer, Glassman, Engh, et al., *Producing and Avoiding Stress Shielding*, Clinical Orthopaedics and Related Research, Vol. 274, pp. 79-96, 1992

[11] Knudsen, F.P., *Effect of Porosity on Young's Modulus of Alumina*, Journal of The American Ceramic Society, Vol.; 45, No. 2, pp. 94-95, 1962.

[12] Spriggs, R.M., Brissette, L.A., *Expressions for Shear Modulus and Poisson's Ratio of Porous Refractory Oxides*, Journal of The American Ceramic Society, Vol. 45, No. 4, pp. 198-199, 1962.

5. Prototype Development and Testing

5.1 Introduction

In a 2000 paper by Simões *et al.* [1], the authors note that the development of a controlled-stiffness implant is limited by currently available materials or fabrication processes. As such, "this remains a theoretical solution since it is difficult to manufacture a device with a very highly differentiated modulus" [2]. Research suggests that flexural rigidity should vary along the length of the prosthesis, using "anisotropic" materials with a defined structure to allow a "distribution of elastic properties inside the stem" for total hip arthroplasty (THA) applications [3, 4, 5]. In their 1992 report, Bobyn *et al.* [6] concluded that only with the use of composite structures might it be possible to adequately address the stiffness mismatch for all stem sizes, especially in the metaphysis. "Hopefully, the next decade will witness innovations in design and materials that will permit the realization of these objectives."

Consistent with that perspective, Glassman *et al.* [7] and Harvey *et al.* [8] recognized the potential advantage of carbon fiber composites as they offer a combination of high fatigue strength and elastic moduli closer to bone than that of metal alloys. Composite structures can be fabricated to be nonhomogeneous and nonisotropic so the structural stiffness can be varied within different implant regions. However, despite perceived advantages, the clinical success of carbon fiber femoral implants has been limited by disappointing fixation at the polymer-bone interface or problems with stem fracture [9]. More significantly, carbon fiber composite implants cannot be fabricated with conventional porous coatings or other bone ingrowth surfaces and thus lack the ability for osseointegration [7]. These complications recall an earlier observation by Tensi *et al.* [4], "…probably anisotropic materials, such as unidirectional solidified metal alloys, are a possible solution", suggesting a need for further research into innovative fabrication methods for

metallic implants. While these observations focused on bone resorption associated with stress shielding and THA, these concerns are equally valid for other orthopaedic implants.

There are distinct advantages in keeping any implant entirely metallic, including biocompatibility, ease of fabrication, a proven history of use and existing FDA approval considerations [10]. However, although implant manufacturers have long promoted some alloys as a "less stiff" material [11], metal alloys used for implant applications have elastic moduli seven to fourteen times greater than that of cortical bone and 200 to 400 times greater than that of cancellous bone, as noted in Table 5.1 [12].

Table 5.1: Elastic moduli of common implant materials and bone

Material	Young's Modulus (MPa)
CoCr alloy	240,000 [23]
Ti-6Al-4V alloy	114,000 [21]
Polymethylmethacrylate	3,000 [24]
Cortical bone	~20,000 [24]
Cancellous bone	~1000 [25]

Because of their mechanical properties and established biocompatibility, orthopaedic applications of porous metals are typically associated with the development of bone ingrowth surfaces on solid implants. This has led to the majority of research interest to be focused on the development of open-cell metallic porosity although arguably greater potential lies with the use of closed-cell porous metals for orthopaedic implant applications. "In such cases, bone ingrowth would not be the major interest, but rather the reduction in material stiffness that has been linked to early loosening following processes of bone loss due to stress shielding" [13].

To overcome this substantial mismatch in stiffness, Ryan *et al.* [13] suggested that engineered pore distributions to match the mechanical properties of bone are the next major

improvement in porous materials**.** Their work and that of Li *et al.* [14] note that mechanical properties of porous materials can be altered and optimized by controlling pore size and shape as well as pore distribution [15]. While a variety of different processes for the production of open-cell porous metals exist, the production of closed-cell porous materials is limited to gas injection or the decomposition of foaming agents in molten metal, both of which produce random pore distributions. Additionally, the size and shape of the resulting pores in the matrix varies depending on the parameters of the manufacturing process. While these methods are commonly used to produce aluminum, zinc and magnesium foams, they are not suitable for the production of closed-cell titanium because of the high melting temperatures involved and the associated reactivity of titanium with oxygen in the melt. Accurate control over production processes for closed-cell metals is readily attained only through additive manufacturing (AM) techniques which use layer-by-layer fabrication technologies.

Aside from manufacturing concerns, the design of closed-cell structures that incorporate an engineered distribution of internal pores is further complicated by the absence of robust correlations between specific porous microstructures and the resulting moduli. The literature is replete with equations that claim to describe the relationship between porosity and mechanical properties (Chapter 3). Many of these relationships are entirely theoretical and those that have an empirical basis are typically limited to a particular material. As noted by Boccaccini [16], “the utility of a microstructure-property correlation is directly related to its ability to predict the property from microstructural measurements and thus to be used for design purposes”.

While earlier efforts to design implants for reduced bone resorption have been limited by biomaterial incompatibilities and/or practical manufacturing complications, AM processes, including the laser sintering and electron beam melting of titanium and cobalt-chrome powders,

can fabricate closed-cell porous constructs as a practical means of reducing implant stiffness and subsequent bone resorption.

The goal of this work is to use the predictive equations developed through earlier finite element (FE) simulations in Chapter 4 to design a prototype implant with a known microstructure, fabricate the resulting design, and test the physical prototype using accepted procedures for 3-point bending. The resulting load-displacement data is to be compared to an Euler-Bernoulli calculation for the deflection of a simply-supported beam (as in 3-point bending) to determine the validity of the original predictive equations.

5.2 Methodology

This research was initiated with the development of a series of representative volume elements (RVEs) of unit cells that incorporate regular arrangements of spherical porosity (Chapter 4). The direction of the applied load on these unit cells was systematically changed to assess the isotropy of the resulting porous structure using FE methods. Relationships between key design parameters (i.e., pore size, pore separation and stacking arrangement) led to a series of equations that correlate physical modifications of the porous structure to the effective moduli of the resulting construct.

All FE data indicate that, regardless of the volume porosity, one porous structure and loading condition consistently yields the lowest value for Young's modulus, suggesting that the design of prototypical implant segment should utilize this loading orientation and microstructure to obtain moduli that have the greatest clinical potential. Application of this structure and the subsequent fabrication, testing and evaluation of a porous construct are further detailed in the process flow depiction in Figure 5.1.

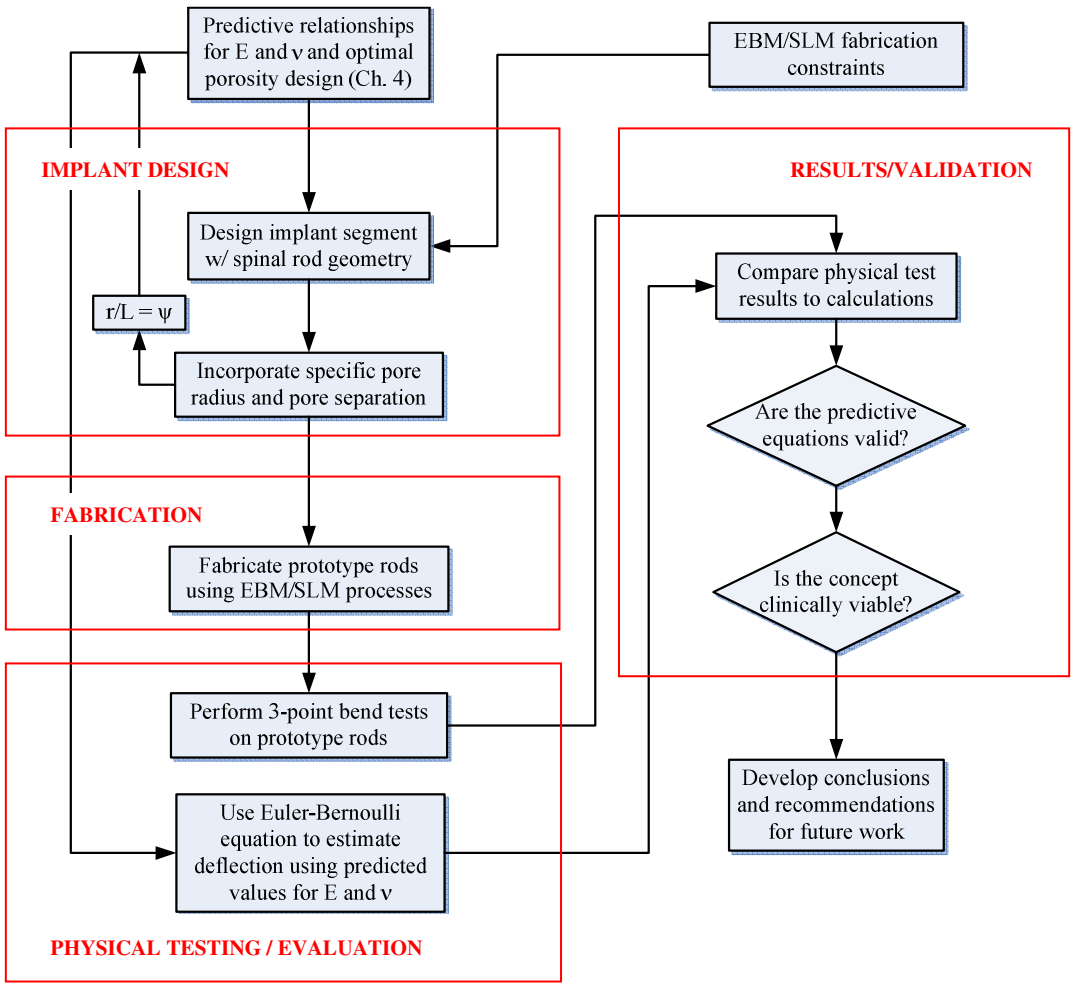

Figure 5.1: Schematic describing prototype development and testing methodology

5.2.1 Implant design

As FE computational results for the RVE assemblies (Chapter 4) correspond to specific microstructures, the desired effective moduli can be defined in terms of specific geometric parameters that describe the porosity. Comparison of computational results with the physical testing of designs that incorporate this engineered porosity can be used to validate the FE model and serve as a useful interpretive tool.

The three porous microstructures evaluated in Chapter 4, face-centered cubic (FCC), hexagonal close-packed (HCP), and body-centered cubic (BCC), were subject to simulated loading conditions that varied the direction of load application on the respective unit cells. These FE analyses led to a set of structure-specific equations that predicted Young's modulus and Poisson's ratio. In general, these results were consistent with existing research on the mechanical properties of porous materials showing that Young's modulus has an inverse relationship with increases in porosity [17]. Since the metallic alloys used in implant applications have significantly larger Young's moduli than cortical bone, those pore arrangements that yielded the largest reduction in modulus at a given porosity have the greatest potential clinical relevance to orthopaedic implant design.

The FE results indicated that for any given ψ, the ratio of pore radius to the center-to-center pore dimension, or volume porosity, the FCC structure with face-centric loading predicted the greatest reduction in Young's modulus over a porosity range of 20-50%. As such, porous constructs for fabrication and subsequent physical testing incorporate the FCC pore arrangement with unit cells oriented such that tensile and/or compressive loads are applied normal to the faces of the cells.

To design the porous prototype, the desired Young's modulus and Poison's ratio must be identified. As shown in Chapter 4, the effective Young's modulus (E_{eff}) and Poisson's ratio (v_{eff}) for an FCC structure with loading normal to the faces of the unit cells is predicted by the following equations:

$$(E_{porous}/E_{solid}) = E_{eff} = -3.267\psi + 1.721 \quad (1)$$

$$v_{eff} = 1.561\psi^2 - 1.230\psi + 0.552 \quad (2)$$

where ψ is the ratio of pore radius, r, to the center-to-center pore dimension, L. These equations are applicable to a ψ range of 0.3333 to 0.4600 and ν assumes the use of a titanium alloy with ν_{Ti} of 0.342. The balance of this study focuses on the design, fabrication and testing of a physical prototype to confirm or refute the aforementioned theoretical conclusions and assess the validity of these predictive equations.

Design development

Design parameters associated with the development of this implant segment are constrained by the geometry of the prototypical implant as well as the practical limits of current AM technology, including feature resolution and achievable accuracy. Once those constraints were incorporated in the design of the implant, a set of 10 implant segments with the optimal porosity structure were fabricated in titanium alloy (Ti6Al4V) using laser and electron beam melting processes.

Cost and fabrication time limitations dictated that the volume of this porous construct be relatively small and capable of being built in a horizontal orientation, with the smallest dimension in the vertical direction, to minimize build time using any AM process. In addition to fabrication size limits, the constructs had to be large enough to permit flexure testing, applying both tensile and compressive loads to the porous construct. As spinal rods have a uniform cylindrical cross section and are typically available in sizes from 4.5 through 6.35 mm in diameter [23], a prototypical 6.35 mm diameter spinal rod was selected for design and fabrication. A construct of this size offers sufficient cross-sectional area and volume to provide a discernable difference in flexural rigidity when tested and compared to solid rods of the same material and physical dimension. This diameter also allowed the inclusion of internal pores that were large enough to be accurately produced by commercially available AM processes.

The planned physical testing procedure also added constraints to the design of the prototype. Testing equipment availability dictated the use of a 3-point bend test which produces a maximum bending moment at the point of load. Accordingly, the use of a fully porous construct could potentially result in a stress concentration associated with a surface pore near the point of load and may result in unrepresentative test data.

To avoid this possibility, a solid exterior or superficial metallic layer was included in the design of the prototypical rod. Accordingly, a 0.5 mm solid layer, a practical AM limit based on examination of representative photomicrographs, was incorporated in the design, leaving a 5.35 mm diameter inner cylindrical section for the porous structure. To achieve maximum porosity within these geometric constraints, a 0.725 mm pore radius was an optimal pore size for the inner core of the rod. This dimension allowed a pore separation (solid material between pores) of 0.5 mm and resulted in a center-to-center pore dimension, L, of 1.95 mm. These pore size and center-to-center pore dimensions for the FCC structure correspond to $\psi = r/L = 0.3718$ and a calculated volume porosity of 29.5% for the porous core.

Substitution of this value for ψ in the predictive equations (1) and (2) for effective Young's modulus and Poisson's ratio yields:

$$(E_{porous}/E_{solid}) = E_{eff} = 0.506$$

and

$$E_{porous} = 0.506\, E_{Ti6Al4V} = 57.6\ GPa \qquad (3)$$

where Young's modulus of solid Ti6Al4V, $E_{Ti6Al4V}$, is 113.8 GPa,

and

$$\nu_{eff} = 0.311 \qquad (4)$$

Figure 5.2 shows the cross-sectional view of the basic porous structure along with key dimensions of the porous core and the resulting rod.

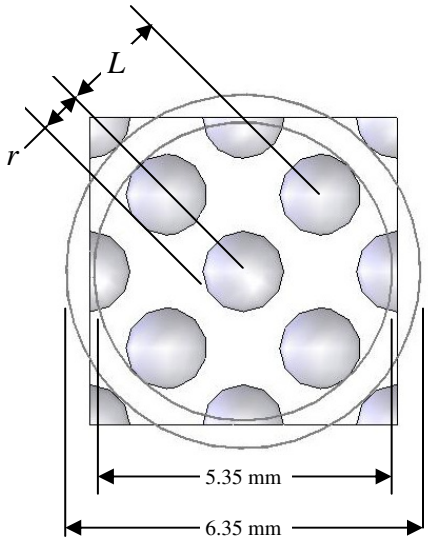

Figure 5.2: End view of rod with inner and outer diameters of the prototype rod shown superimposed on the FCC porous structure

Forty-eight FCC unit cells with a side length of 2.76 mm were combined and oriented along the long axis of the rod, resulting in a porous construct 132.4 mm in length. Figure 5.3 shows the detail of the final solid model including the fully porous structure and after extrusion and incorporation of the porous core within the solid outer layer.

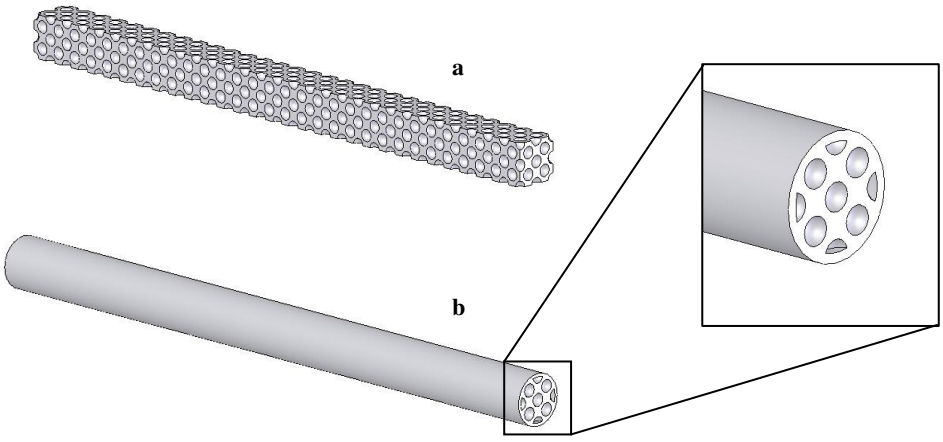

Figure 5.3: Solid model of porous spinal rod; **a**) basic porous inner structure, **b**) final geometry (bottom and inset) after extrusion and addition of the solid outer layer

5.2.2 Prototype fabrication

Fabrication of any regular porous structure has been limited in the past by the lack of commercially-viable technologies that are capable of replicating pores of a defined size and shape and the ability to place those pores in a defined and predictable orientation.

AM, also termed rapid prototyping (RP), allows the production of complex geometries because all AM processes involve a layered manufacturing technology. A three-dimensional solid model of the desired geometry is created using computer-aided design (CAD) software. The resulting design file, saved in an STL format, becomes the input to the AM machine which decomposes the three-dimensional object into a stack of two-dimensional layers with a nominal thickness of 20-100 µm (depending on the AM system), a process analogous to the generation of a computed tomography (CT) scan in a clinical setting.

In the production of a metallic component, titanium or other metal powders with diametrical size of 10 – 100 µm is spread across a build surface and a CO_2 laser or electron beam is focused onto the powder layer and selectively melts the material, fusing it into a solid sheet. The next powder layer is laid down over the previous, and the process is repeated, creating a solid object with all of the features present in the original CAD file. Because the process proceeds in layer-wise manner, the complexity and detail of the resulting component is limited only by the thickness of the powder layer, the average size of the metal particles and the accuracy and resolution limitations of the machine, typically in the range of ± 20-200 µm.

Of greater concern in this study is the ability of these systems to generate, within the resolution limits noted, geometrically precise structures as opposed to creating an undefined void within the solid body by a momentary interruption of the laser or electron beam. While this creates a porous material, the resulting microstructure is dependent on the operational

characteristics of the machine (e.g., laser or electron beam power, scan spacing and layer thickness) rather than the geometry of a given microstructure. Further, the resulting porous bodies cannot be quantified for potential implant applications except for an estimation of macroscopic bulk properties. Relevant research on the achievable size of well-defined pores [18, 19, 20] indicate that diameters within the range of 200 to 700 µm can be produced by selective laser melting (SLM), direct metal laser sintering (DMLS), and electron beam melting (EBM)..

Manufacturers of AM systems provided samples of titanium fabrications representing the minimum achievable feature dimensions (i.e., pore diameter and pore separation dimension). Figure 5.4 shows photomicrographic images of those samples, confirming that the thickness of the material separating the pores (~500 µm) is within the practical limits of these technologies and that these AM processes are capable of precise pore design and positioning.

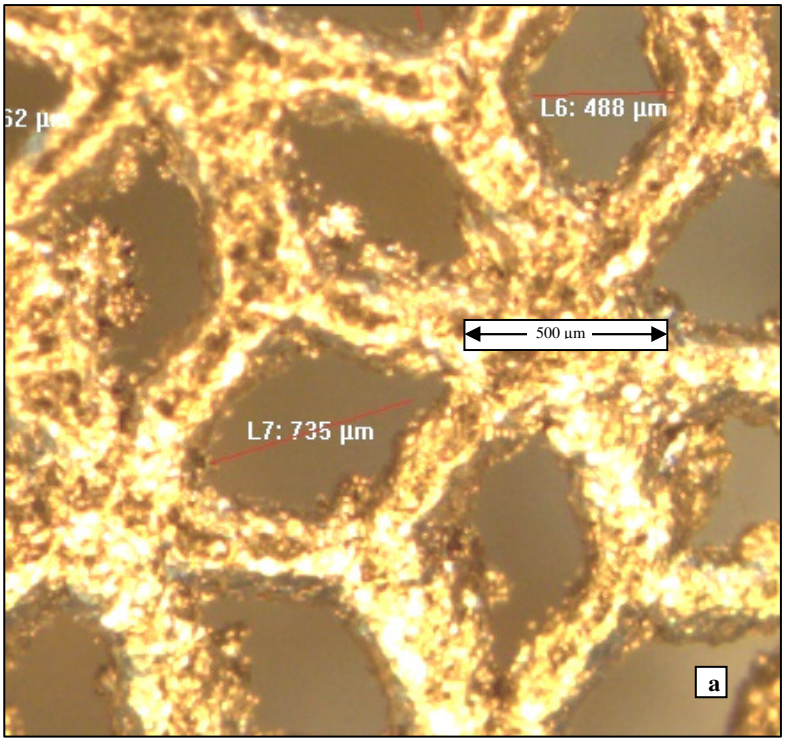

Figure 5.4: Photomicrographs of structure showing dimensional limits; **a**) DMLS

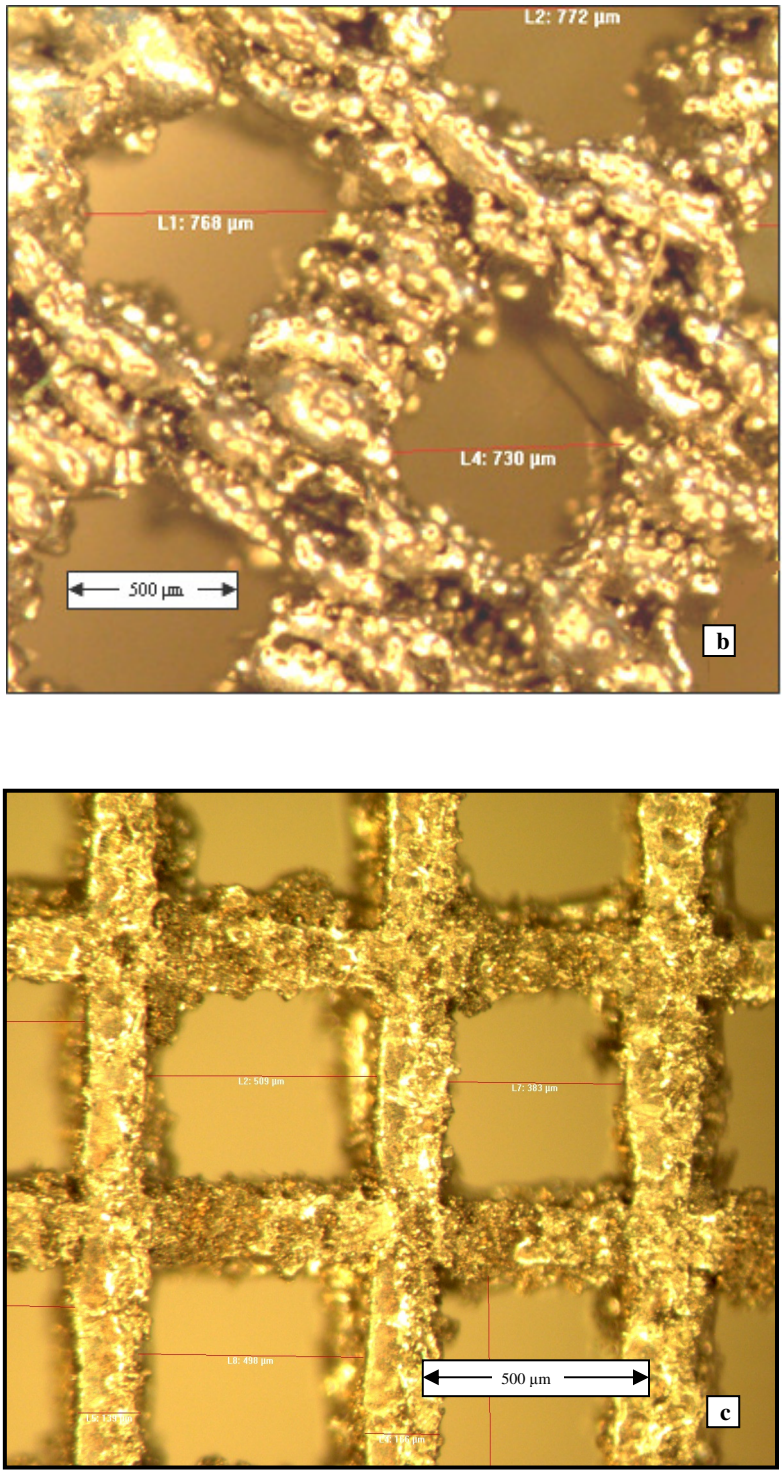

Figure 5.4 (continued): Photomicrographs of structure showing dimensional limits; **b**) EBM and **c**) SLM AM processes.

Production of the as-designed porous constructs was completed by Arcam AB in Göteborg, Sweden, and by SLM Solutions GmbH in Lübeck, Germany. All rods were fabricated with Ti6Al4V powder with machine parameters (electron beam or laser power, scan speed, layer thickness and scan spacing) set by the manufacturer. Figure 5.5 shows the resulting porous constructs, partially sectioned to show internal detail, produced by both processes.

A total of 20 spinal rods were produced, 10 for each of the two processes, EBM and SLM. Within each group of 10 rods, 5 were produced with a porous inner core and 5 were solid rods with the same external dimensions. Sets of porous and solid rods were produced at the same time with the same process parameter settings for subsequent comparative analysis.

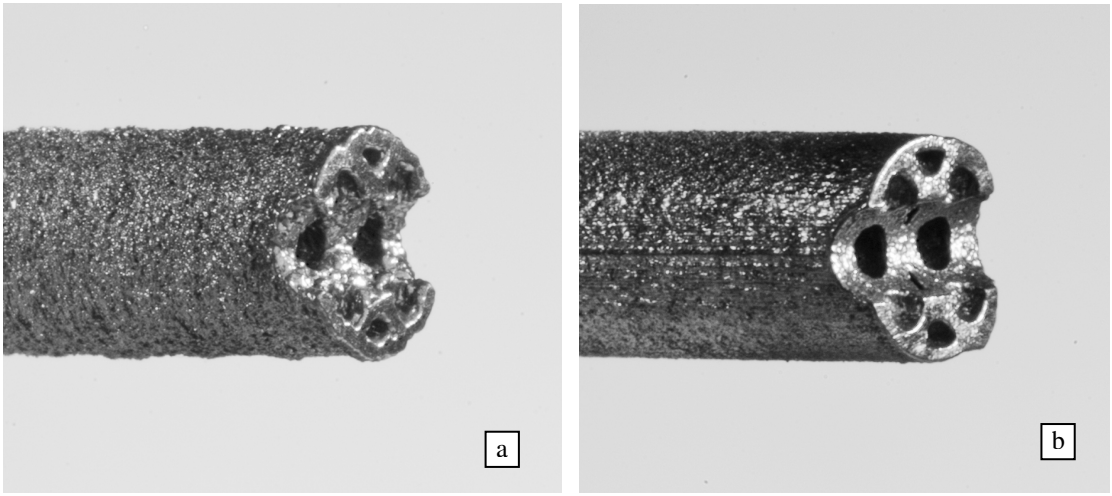

Figure 5.5: Photos of prototypical Ti6Al4V spinal rods; **a**) EBM, and **b**) SLM.

5.2.3 Physical testing/experimental loading

Testing consisted of a 3-point bend test using an MTS Alliance RT/50 electro-mechanical test machine with a 50 kN load cell (MTS Systems Corporation, Eden Prairie, Minnesota) that was calibrated before each test run. The test setup used a CU-LF-13 adjustable bend test fixture (Wyoming Test Fixtures Inc., Salt Lake City, Utah) with 12.7 mm (0.5 in) diameter hardened

steel rollers at points of contact with the test specimen. The span between the lower support rollers was 101.6 mm (4 in). Machine crosshead speed was 5mm/min and the sampling rate was 10 Hz. Data were recorded via TestWorks® 4 software (version 4.10A, MTS Systems Corporation) and load-displacement results were tabulated and transferred to an Excel spreadsheet for subsequent analysis.

Although no specific ASTM or ISO standard applied to the testing of these prototype rods, guidance on crosshead speed (< 25 mm/min) and sample size (N ≥ 5 samples) as noted in ASTM F1717-04: *Standard Test Methods for Spinal Implant Constructs in a Vertebrectomy Model* were observed. As noted in this standard, examination of each load-displacement curve revealed a laxity (see data in Figure 5.7) in the test fixture due to surface irregularities at the interface between the support rollers and the test specimen, as shown in Figure 5.6.

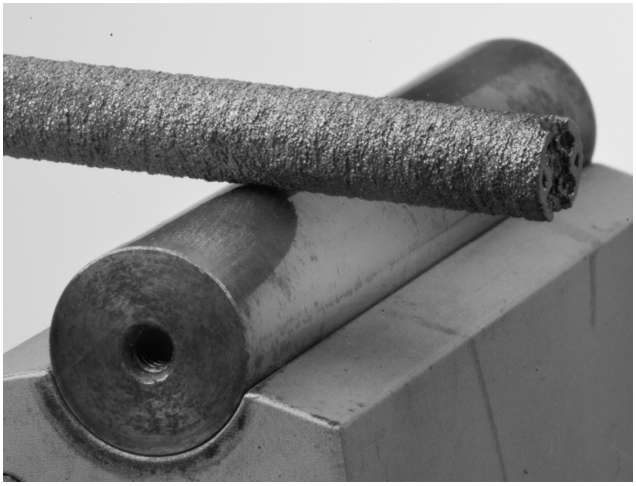

Figure 5.6: Surface irregularities at test roller-specimen

The linear portion of the curve (beyond the laxity region) was used to define the slope of the linear elastic portion of the load-displacement curves, as shown in Figure 5.7, and estimate the flexural rigidity of the prototype rods.

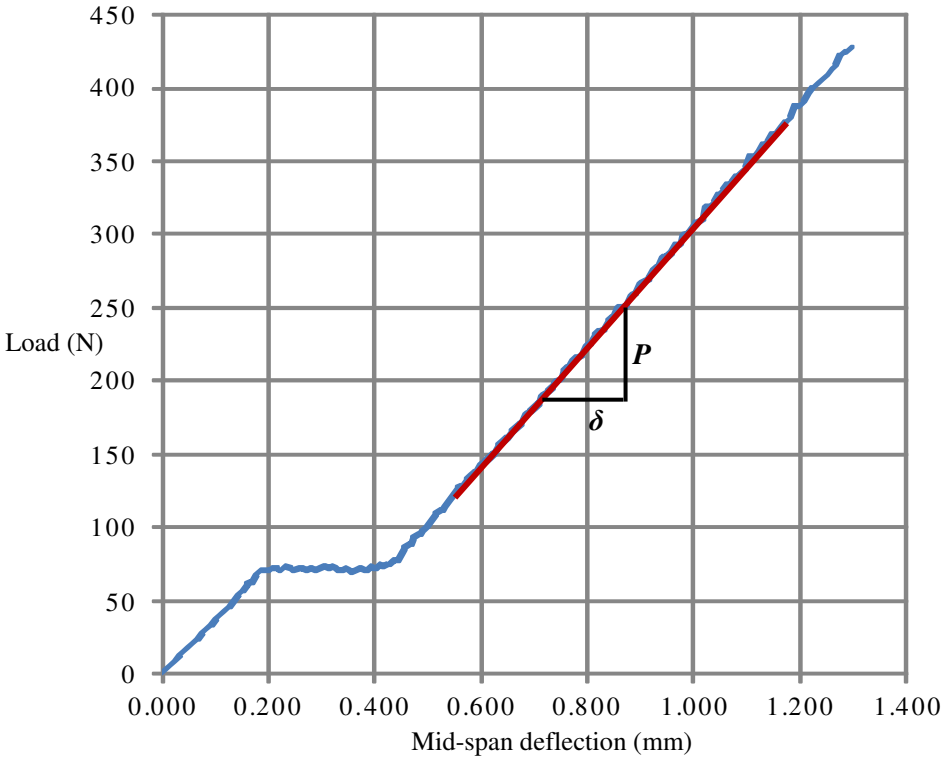

Figure 5.7: Sample load-displacement curve (SLM Ti6Al4V solid rod #4, run #3) showing laxity region at ~75N load.

As an elastic response was desired, testing was manually terminated at approximately 400N applied load for each test, a value well below the calculated yield point for spinal rod prototypes. Load-displacement data for five load/unload cycles were recorded. The first two load/unload cycles were considered to be conditioning runs and were excluded from analysis. The slope of the remaining three loading curves was determined based on linear regression.

5.2.4 Estimation of theoretical flexural rigidity

To compare the experimental response of the porous construct to that predicted by the proposed equations, the flexural rigidity may be calculated using the Euler-Bernoulli (E-B) equation for the mid-span deflection, δ, of a simply-supported beam, as in the 3-point bend test:

$$\delta = PD^3/(48EI) \quad (5)$$

or

$$EI = [D^3/48](P/\delta) \quad (6)$$

where P is the applied load, D is the distance between the support rollers and EI is the flexural rigidity of the porous or solid rod.

Since the porous construct includes both a solid outer layer and a porous inner core, an **equivalent** porous structure with **homogenous** material properties and a uniform cross section may be defined. The theoretical flexural rigidity of the equivalent porous construct which combines the flexural rigidity of both the solid outer layer and porous inner core is given by:

$$(EI)_{equivalent} = (EI)_{solid\ outer} + (EI)_{porous\ inner} \quad (7)$$
$$= (E_{Ti6Al4V}[\pi(d_o^4 - d_i^4)/64])_{solid\ outer} + (E_{porous}[\pi(d_i^4/64)])_{porous\ inner}$$

where d_o = outer diameter (6.35 mm), d_i = inner diameter (5.35 mm), $E_{Ti6Al4V}$ = Young's modulus of the solid outer layer (113.8 GPa) and E_{porous} = Young's modulus of the porous inner core (57.6 GPa), the value predicted by equation (1) as developed in the FE analysis (Chapter 4).

Substitution in equation (7) yields an equivalent theoretical flexural rigidity, $(EI)_{equivalent}$ of a homogenous construct:

$$(EI)_{equivalent} = (EI)_{outer\ layer} + (EI)_{porous\ inner}$$
$$= (113{,}800\,[\pi(12.6)])_{outer\ layer} + (57{,}600[\pi(12.8)])_{porous\ inner}$$
$$= 6.821 \times 10^6\ N\text{-}mm^2$$

As a solid Ti6Al4V rod is intrinsically homogeneous, the corresponding theoretical flexural rigidity is:

$$(EI)_{solid} = (E_{Ti6Al4V}[\pi(d_o^4/64)])$$

where d_o = outer diameter (6.35 mm) and $E_{Ti6Al4V}$ = Young's modulus of the solid material (113.8 GPa) which upon substitution gives:

$$(EI)_{solid} = 113{,}800[\pi(25.4)]$$
$$= 9.083 \times 10^6 \text{ N-mm}^2$$

These calculated theoretical values for flexural rigidity for both the solid and porous Ti6Al4V rods are compared to the experimental flexural rigidity predicted by E-B beam theory and the experimental P/δ data generated in the 3-point bend tests of the porous and solid physical constructs. Comparisons of the experimental and theoretical estimations of flexural rigidity are essential to this research as the theoretical flexural rigidity of the porous rod depends on the validity of the predictive equations developed in Chapter 4.

5.2.5 Estimation of experimental flexural rigidity

As the MTS TestWorks software provides load-displacement data directly, the flexural rigidity of the experimental test specimens, $(EI)_{exp}$, is determined from the E-B equation (6):

$$(EI)_{exp} = [D^3/48](P/\delta)$$

or

$$= 21850(P/\delta) \qquad (8)$$

where D = distance between support rollers (101.6 mm), P is the applied load at mid-span, δ is the resulting deflection of the test specimen at the point of applied load P, and the ratio P/δ is the slope of the load-displacement curve. Subsequent substitution of the regressed values for P/δ into equation (8) yields the experimental flexural rigidity of the porous and solid constructs and facilitates comparison with the theoretical estimations.

5.3 Results

Experimental loading

The regressed values for slopes, P/δ, of the experimental load-displacement data for each of the 5 loading runs are shown in Figures 5.8 and 5.9 for the EBM and SLM rods, respectively.

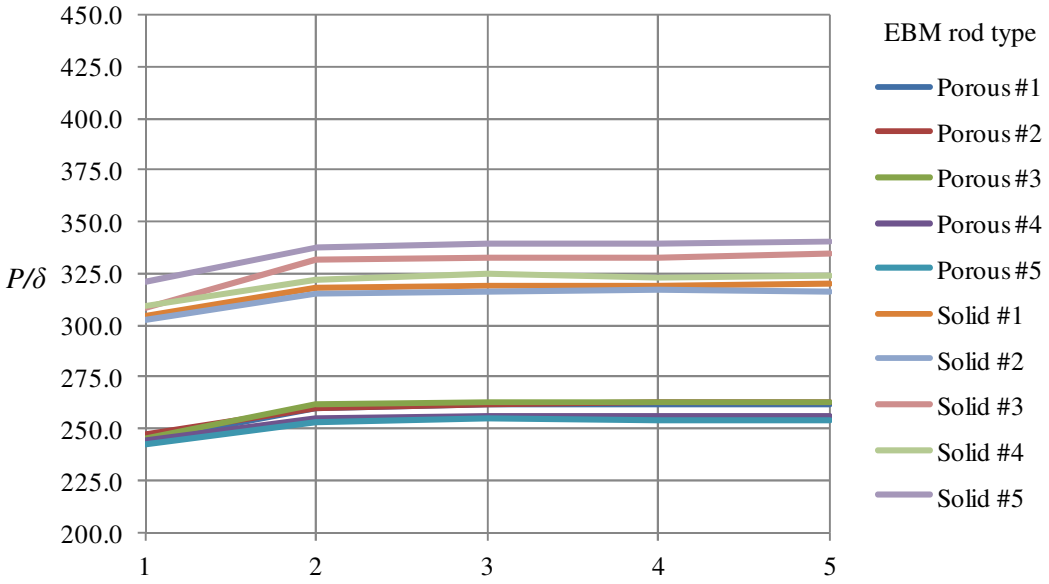

Figure 5.8: Slope (N/mm) of the experimental load-displacement data by test run; EBM prototypes

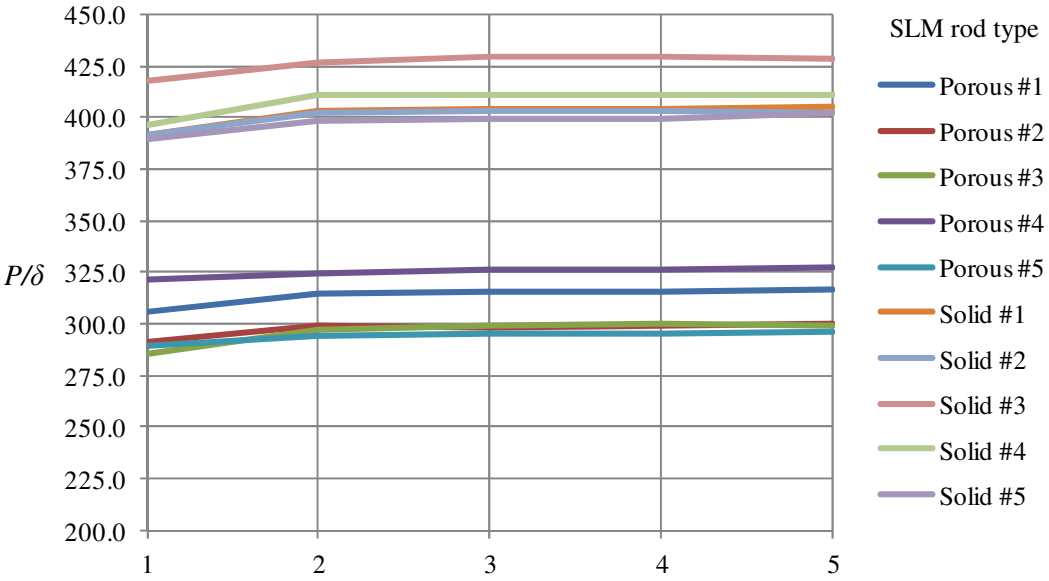

Figure 5.9: Slope (N/mm) of the experimental load-displacement data by test run; SLM prototypes

Table 5.2 summarizes the mean slope and summary statistics of the load-displacement data for the final three runs (excluding the initial two conditioning runs) for each group of test specimens.

Table 5.2: Slopes (P/δ) in N/mm of the experimental load-displacement data for test runs #3 through #5 for each spinal rod specimen.

Slope (P/δ)	**EBM**		**SLM**	
Rod type	Porous	Solid	Porous	Solid
Mean	259.31	326.67	307.28	409.67
Standard Deviation	3.71	9.19	12.37	10.86
95% Confidence Interval	257.26-261.37	321.58-331.75	300.43-314.13	403.66-415.69

Comparison of theoretical versus experimental data

As predictable modification of flexural rigidity is the primary focus of this research, load-displacement slope data were used to estimate the experimental flexural rigidity using equation (8):

$$(EI)_{exp} = [D^3/48](P/\delta) = 21850(P/\delta)$$

and are shown in Figures 5.10 and 5.11. These figures also include the theoretical flexural rigidity estimates for the porous (EI = 6.82 x 10^6 N-mm^2) and solid (EI = 9.08 x 10^6 N-mm^2) rods as calculated in 5.2.4.

E-B beam theory may also be applied to the theoretical estimates of flexural rigidity such that the corresponding theoretical mid-span deflection, δ, in response to a load of 400 N may be estimated. This theoretical mid-span deflection, as well as the experimental mid-span deflection and normalized difference, Δ, in flexural rigidity and mid-span deflection between the theoretical and the experimental results are summarized in Table 5.3.

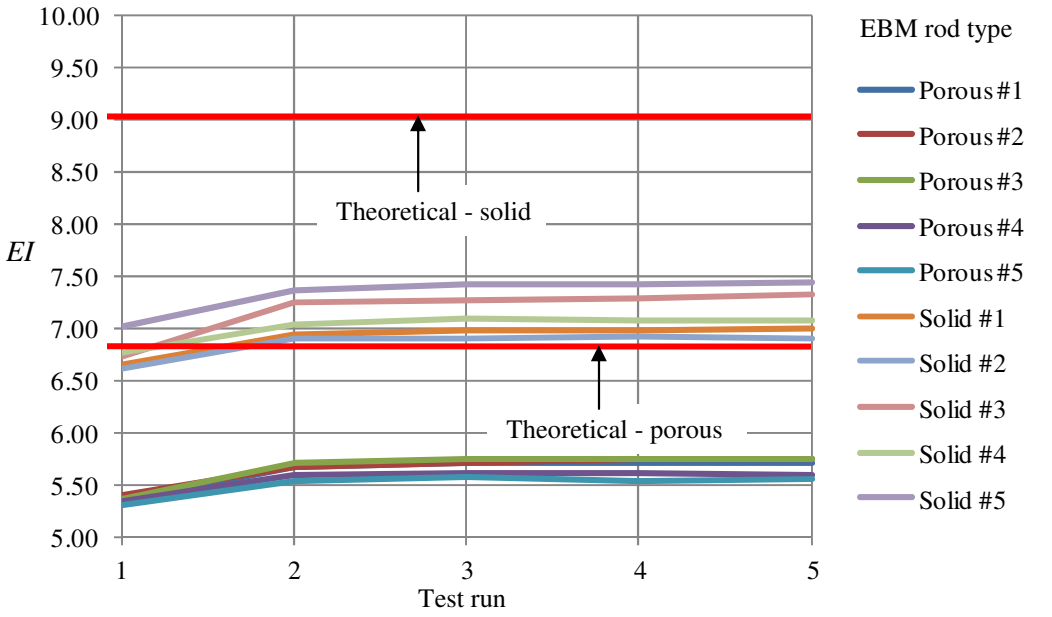

Figure 5.10: Comparison of experimental flexural rigidity (N-mm^2) with theoretical flexural rigidity of the EBM Ti6Al4V prototype spinal rods.

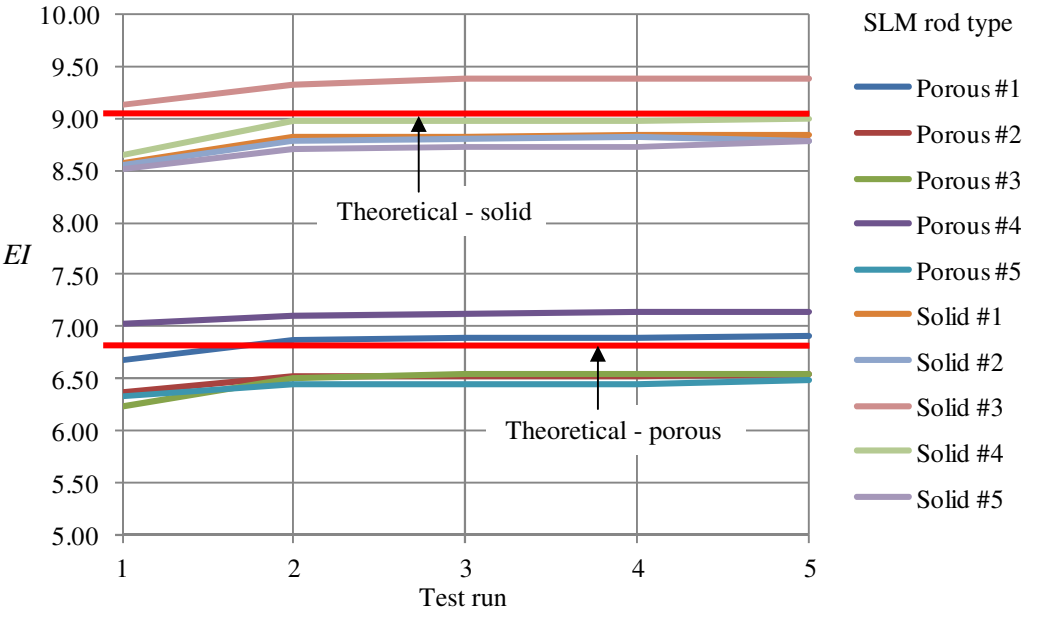

Figure 5.11 Comparison of experimental flexural rigidity (N-mm^2) with theoretical flexural rigidity of the SLM Ti6Al4V prototype spinal rods.

Table 5.3: Comparison of theoretical estimation and experimental flexural rigidity and mid-span deflection. The load-displacement data (P/δ) are mean values for all prototype constructs of one type during test runs #3 through #5.

	Theoretical		**EBM experimental**		**SLM experimental**	
	Porous	Solid	Porous	Solid	Porous	Solid
P/δ **(N/mm)**	-	-	259.31	326.67	307.28	409.67
EI **(N-mm^2 x 10^6)**	6.82	9.08	5.67	7.14	6.71	8.95
Δ **(*EI*)**	-	-	-16.9%	-21.4%	-1.6%	-1.4%
δ **(mm)**	1.28	0.96	1.54	1.22	1.30	0.98
Δ **(** δ **)**	-	-	+20.3%	+27.1%	+1.6%	+2.1%

5.4 Discussion

The results of the 3-point bend test for the **solid** SLM Ti6Al4V rods yield values for flexural rigidity that agree to within 1.4 % of the theoretical calculation with Young's modulus, $E_{Ti6AL4V}$, of 113.8 GPa. For the porous rod, the theoretical estimates of flexural rigidity, $(EI)_{equivalent}$, assumed a value of 57.6 GPa for Young's modulus of the porous inner core of the designed /fabricated spinal rod, a value based on the predictive equations developed in Chapter 4. The experimental 3-point bend test results for the **porous** SLM Ti6Al4V rod yielded an experimental flexural rigidity of 6.71 x 10^6 N-mm^2, within 1.6% of the theoretical flexural rigidity determined from application of the proposed predictive equations. These minimal errors confirm the validity of the basic predictive equations for Young's modulus that correlate a specific porous microstructure (FCC pore arrangement) and loading condition (normal to the faces of the unit cubes) with mechanical properties.

The large differences between the theoretical flexural rigidity and the experimental flexural rigidity based on the physical tests of the EBM Ti6Al4V rods suggest an issue with EBM machine settings rather than a deficiency in the predictive equations. As noted earlier in 5.2.2, improper machine settings, notably scan spacing or laser or electron beam power, can fail to fully

melt the titanium power and produce a fully dense component. The net effect of these deficiencies in machine build parameters is the inadvertent creation of a porous matrix, separate from the designed porosity and defined pore arrangement detailed in the input build file.

The mean values for experimental flexural rigidity of the EBM rods were significantly reduced from expected theoretical values: 16.9% less for the porous rods and 21.4% less for the solid rods. These large deviations can only be attributed to machine settings as Arcam AB has repeatedly demonstrated that their process is able to consistently produce components in Ti6Al4V with a Young's modulus equivalent to those produced on an SLM machine [22].

The experimental flexural rigidity calculated from the load-displacement data indicated that the solid EBM Ti6AL4V rod had an *EI* of 7.14 x 10^6 N-mm^2 rather than the expected value of 9.08 x 10^6 N-mm^2 (theoretical) or 8.95 x10^6 N-mm^2 (as demonstrated by the experimental SLM rods). However, if this reduced experimental flexural rigidity is redefined as a percentage of fully dense material, comparison of the EBM porous constructs is still possible. For example, if the solid EBM rods are assumed to have approximately 80% of the flexural rigidity of a solid, fully dense Ti6Al4V rod, the mean flexural rigidity for the porous EBM rods should also be ~80% of the expected value if the deviation from expected results is due to machine variability rather than a problem with the predictive equations. The equations proposed in this work predicted a theoretical flexural rigidity of 6.82 x 10^6 N-mm^2 for the porous construct. Taking 80% of this value yields a flexural rigidity of 5.46 x10^6 N-mm^2, which is within 4% of the mean experimental flexural rigidity (5.67 x10^6 N-mm^2) of the tested porous constructs from Arcam AB, as noted in Table 5.3.

After the 3-point bend tests were completed, all rods were weighed to determine if differences in as-fabricated density might explain the disparity in EBM versus SLM test results. The porous EBM rods were found to have a mean weight 8.3% less than that of the SLM rods.

Similarly, the mean weight of the solid EBM rods was 11.0% less than that of the SLM rods which confirms the existence of unintended microporosity within the EBM samples. While variation in diametrical dimensions and/or surface roughness may be contributory or differentiating factors, these differences in EBM versus SLM test results suggest further future evaluation of EBM test specimens fabricated at machine settings that preclude the development of unintended porosity in the final construct.

Since the design of the porous test rods incorporates a solid outer layer that contributes significantly (~ 65%) to the overall equivalent flexural rigidity of the resulting construct, the sensitivity of the theoretical flexural rigidity to the proposed predictive equations was investigated. An additional analysis was performed in which the Young's modulus of the porous inner core was reduced by 30% and the theoretical equivalent flexural rigidity, as calculated in section 5.2.4, was re-evaluated. The resultant theoretical flexural rigidity of 6.126×10^6 N-mm^2, associated with a 30% reduction in Young's modulus for the inner core, was compared to the initial determination with Young's modulus of 57.6 GPa, a value based on the use of the predictive equations developed in Chapter 4. As shown in Figure 5.12, the 30% reduction in the Young's modulus of the porous inner core resulted in a 10% reduction in theoretical flexural rigidity. As such, the experimental prototype design, with porous inner core and solid outer skin, is sufficiently sensitive to the Young's modulus of the porous inner structure, and is an appropriate construct with which to evaluate the proposed predictive equations for Young's modulus for a specific porous microstructure and loading condition.

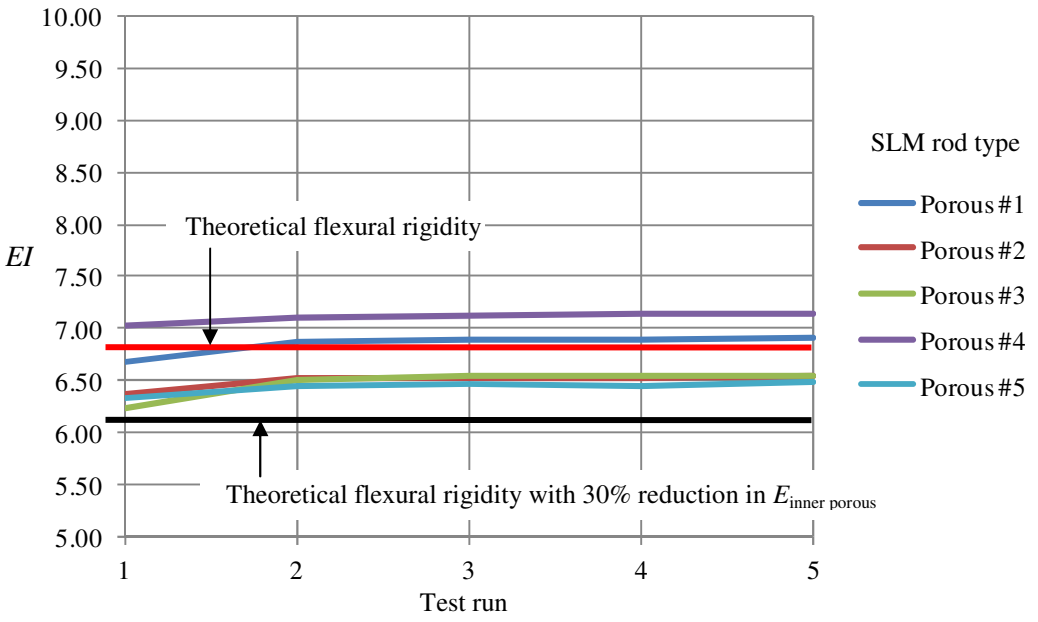

Figure 5.12: Comparison of theoretical flexural rigidity (N-mm^2) of the porous spinal rods with initial and 30% reduction in Young's modulus for porous inner core. The experimental flexural rigidity data for the porous SLM Ti6Al4V spinal rods are included for comparison.

While initial FE analyses (Chapter 4) indicated that a second order equation describes changes in Poisson's ratio as a function of ψ or volume porosity and predicted that Poisson's ratio is reduced to about 90 ± 3% of that of the non-porous material, the physical test procedure used in this study cannot be used to confirm the validity of those equations. Future work should include additional testing in accordance with ASTM E132 – 04: *Standard Test Method for Poisson's Ratio at Room Temperature* to confirm or refute the proposed predictive equations for Poisson's ratio.

5.5 Conclusions

The results of the physical testing confirm the validity of the equations proposed to predict the moduli of a specific microstructure and load orientation to within 2% of theoretical over a range of 20-50% porosity. As the selection of microstructure appears to minimally affect the effective Young's modulus, future studies might investigate different load orientations to

further establish the validity of the underlying relationships between ψ and/or volume porosity and effective moduli.

Of primary concern is the potential clinical viability of this design methodology. None of the porous constructs in this study have been evaluated for fatigue properties. Any future study aimed at clinical application needs to include analysis of currently available *S-N* or *M-N* curves (i.e., plots of stress, *S*, or moment, *M*, against the number of cycles to failure, *N)* to obtain a theoretical estimate of the fatigue life ($N \geq 5 \times 10^6$ cycles) of the reduced-stiffness implant. While data on fatigue properties of titanium specimens fabricated by AM processes is available, none of the published fatigue data include or anticipate the proposed application of engineered porosity to the manufacture of orthopaedic implants.

Further work is also needed to confirm the validity of any estimate of fatigue life to determine if the engineered porosity concept is viable for long-term, load-bearing implant applications. While the results of future work may indicate that these porous structures are not appropriate for high load applications, the process may still be appropriate for the design of bone plates or upper extremity implants for which stress shielding and bone resorption concerns are less critical to functional outcome.

5.6 References

[1] Simões, J.A., Marques, A.T., Jeronimidis, G., *Design of a controlled-stiffness composite proximal femoral prosthesis*, Composites Science and Technology, Vol. 60, pp. 559-567, 2000.

[2] Simões, J.A.O., Taylor, M., Marques, A.T., Jeronimidis, G., *Preliminary investigation of a novel controlled stiffness proximal femoral prosthesis*, Proceedings of the Institution of Mechanical Engineers, Vol. 212, Part H, pp. 165-175, 1998.

[3] Kuiper, J.H., Huiskes, R., *Mathematical Optimization of Elastic Properties: Application to Cementless Hip Stem Design*, Journal of Biomechanical Engineering, Vol. 119, No. 2, pp. 166-174, 1997.

[4] Tensi, H.M., Gese, H., Ascherl, R., *Non-linear three-dimensional finite element analysis of a cementless hip endoprosthesis*, Proceedings of the Institution of Mechanical Engineers: Journal of Engineering in Medicine, Vol. 203, Part H, pp. 215-222, 1989.

[5] Niinimaki, T. J., Puranen, J.P., Jalovaara, P K., *Total Hip Arthroplasty Using Isoelastic Femoral Stems: A Seven- to Nine-Year Follow-Up in 108 Patients*, Journal of Bone & Joint Surgery (Br), Vol. 76-B, pp. 413-418, 1994.

[6] Bobyn, Mortimer, Glassman, Engh, et al., *Producing and Avoiding Stress Shielding*, Clinical Orthopaedics and Related Research, Vol. 274, pp. 79-96, 1992

[7] Glassman, A., Bobyn, J., Tanzer, M., *New Femoral Designs: Do They Influence Stress Shielding?, Clinical Orthopaedics and Related Research, Vol. 453, pp. 64-74, 2006.*

[8] Harvey, E.J., Bobyn, J.D., Tanzer, M. et al., *Effect of Flexibility of the Femoral Stem on Bone-Remodeling and Fixation of the Stem in a Canine Total Hip Arthroplasty Model without Cement*, Journal of Bone and Joint Surgery, Vol. 81-A, No. 1, pp. 93-107, 1999.

[9] Glassman, A.H., Crowninshield, R.D., Schenck, R., Herberts, P., *A Low Stiffness Composite Biologically Fixed Prosthesis*, Clinical Orthopaedics and Related Research, Vol. 393, pp. 128-135, 2001.

[10] Bobyn, J., Glassman, A., Goto, H., Krygier, J., et al., *The Effect of Stem Stiffness on Femoral Bone Resorption after Canine Porous-coated Total Hip Arthroplasty*, Clinical Orthopaedics and Related Research, Vol. 261, pp. 196-213, 1990.

[11] Skinner, H.B., *Isoelasticity and Total Hip Arthroplasty*, Orthopedics, Vol. 14, No. 3, pp. 323-328, 1991.

[12] Lewis, J.L., Askew, M.J., Wixson, R.L. et al., *The Influence of Prosthetic Stem Stiffness and of a Calcar Collar on Stresses in the Proximal End of the Femur with a Cemented Femoral Component*, Journal of Bone and Joint Surgery, Vol. 66-A, No. 2, pp. 280-286, 1984.

[13] Ryan, G., Pandit, A., Apatsidis, D.P., *Fabrication methods of porous metals for use in orthopaedic applications*, Biomaterials, Vol. 27, No. 13, pp. 2651-2670, 2006.

[14] Li, C., Zhu, Z., *Dynamic Young's modulus of open-porosity titanium measured by the electromagnetic acoustic resonance method*, Journal of Porous Materials, Vol. 13, pp. 21-26, 2006.

[15] Karageorgiou, V., Kaplan, D., *Porosity of 3D biomaterial scaffolds and osteogenesis*, Biomaterials, Vol. 26, No. 27, pp. 5474-5491, 2005.

[16] Boccaccini, A.R., *Comment on "Dependence of ceramic fracture properties on porosity"*, Journal of Materials Science Letters, Vol. 13, pp. 1035-1037, 1994.

[17] Rice, R.W., *Comparison of physical property-porosity behavior with minimum solid area models*, Journal of Materials Science, Vol. 31, pp. 1509-1528, 1996.

[18] Chua, C.K., Leong, K.F., Cheah, C.M., Chua, S.W., *Development of a Tissue Engineering Scaffold Structure Library for Rapid Prototyping*, The International Journal of Advanced Manufacturing Technology, Vol. 21, No. 4, pp. 291-301, 2003.

[19] Hayashi, T., Maekawa, K., Tamura, M., Hanyu, K., *Selective Laser Sintering Method Using Titanium Powder Sheet Toward Fabrication of Porous Bone Substitutes*, JSME International Journal Series A –Solid Mechanics & Material Engineering, Vol. 48, No. 4, pp. 369-375, 2006.

[20] Lin, C.Y., Kikuchi, N., Hollister, S.J., *A novel method for biomaterial scaffold internal architecture design to match bone elastic properties with desired porosity*, Journal of Biomechanics, Vol. 37, No. 5, pp. 623-636, 2004.

[21] Collins, E.W., *Materials Properties Handbook: Titanium Alloys*, ASM International, December, 1995.

[22] Arcam EBM system: *Ti6Al4V ELI Titanium Alloy*, brochure , n.d., Arcam AB, Mölndal, Sweden

[23] Kwak, S.D., Slivka, M., *Biomechanical Characterization of Cobalt-Chromium Alloy Spinal Rods*, DePuy Spine, Inc., Raynham, MA

[24] Ratner, B.B., Hoffman, A.S., Schoen, F.J., Lemons, J.E., *Biomaterials Science: An Introduction to Materials in Medicine,* Academic Press, San Diego, CA, 1996

[25] Hodgskinson, R., Currey, J.D., *Young's modulus, density and material properties in cancellous bone over r a large density range*, Journal of Materials Science: Materials in Medicine, Vol. 3, pp. 377-381, 1992.

6. Study conclusions

As stress shielding due to implant stiffness and the resulting bone resorption is a valid clinical concern, this research was focused on developing a factual response to the question…

> *Can engineered porosity be applied to predictably reduce the flexural rigidity of an orthopaedic implant?*

In addressing this question through the research activities detailed herein, several key findings became evident:

1) **Existing mechanical property-porosity relationships**, specifically those that describe Young's Modulus and Poisson's ratio over a porosity range of 20-50%, are generally interpretive rather than predictive and **cannot be used for the design of an engineered porous structure**.

2) **Application of finite element (FE) methods** to three microstructures, characterized by FCC, HCP or BCC internal pore arrangements, **resulted in predictive equations for effective moduli**. Use of these equations for a rhombohedral (FCC) pore arrangement with 30% porosity indicated an effective reduction of ~50% in Young's modulus.

3) **Young's modulus was shown to be a linear function of ψ**, the ratio of pore radius to pore separation, over a porosity range of 20-50%. These linear relationships for various microstructures differ primarily in their intercept rather than slope.

4) **Poisson's ratio as a function of ψ is second order** over the same range of porosity. Results indicate that Poisson's ratio approaches a minimum near the largest porosity level in this study (~50%).

3) Results of the FE simulation demonstrate that **these microstructures do not exhibit isotropic behavior** and become increasingly anisotropic (>10% at 50% porosity) as the porosity or ψ value increases. This change in anisotropic behavior as porosity increases is evident for both Young's modulus and Poisson' ratio

4) Selection of a specific **microstructure has only a minimal effect** (2.5% across a range of 20-50% porosity) **on the resultant Young's modulus**. However, different microstructures subjected to identical loading conditions yield measurably different results for Poisson's ratio.

3) **Fabrication of a prototypical porous Ti6Al4V implant** structure in the form of a spinal rod **resulted in well-defined pores** and allowed the comparative physical testing

of constructs produced by both electron beam melting (EBM) and selective laser melting (SLM).

5) Three-point bend **testing** in combination with the Euler-Bernoulli equation **showed that the proposed equations allow prediction of experimental flexural rigidity to within 2% of theoretical flexural rigidity**.

In summary, this research indicates that the moduli of porous constructs can be tailored to meet specific clinical needs with the appropriate selection of load orientation, microstructure (in the case of Poisson's ratio only), porosity or ψ level, and the proposed porosity-mechanical property relationships. A graphical comparison of proposed and existing porosity-mechanical property relationships is shown in Appendix E.

Of primary concern is the viability of this methodology to the design of orthopaedic implants. It must be noted that none of the porous constructs in this study have been evaluated for fatigue properties. While data on fatigue properties of titanium specimens fabricated by additive manufacturing (AM) processes is available, none of these data include or anticipate the proposed application of engineered porosity to the manufacture of orthopaedic implants. Future work is needed to obtain a theoretical estimate of the fatigue life of the reduced-stiffness implant.

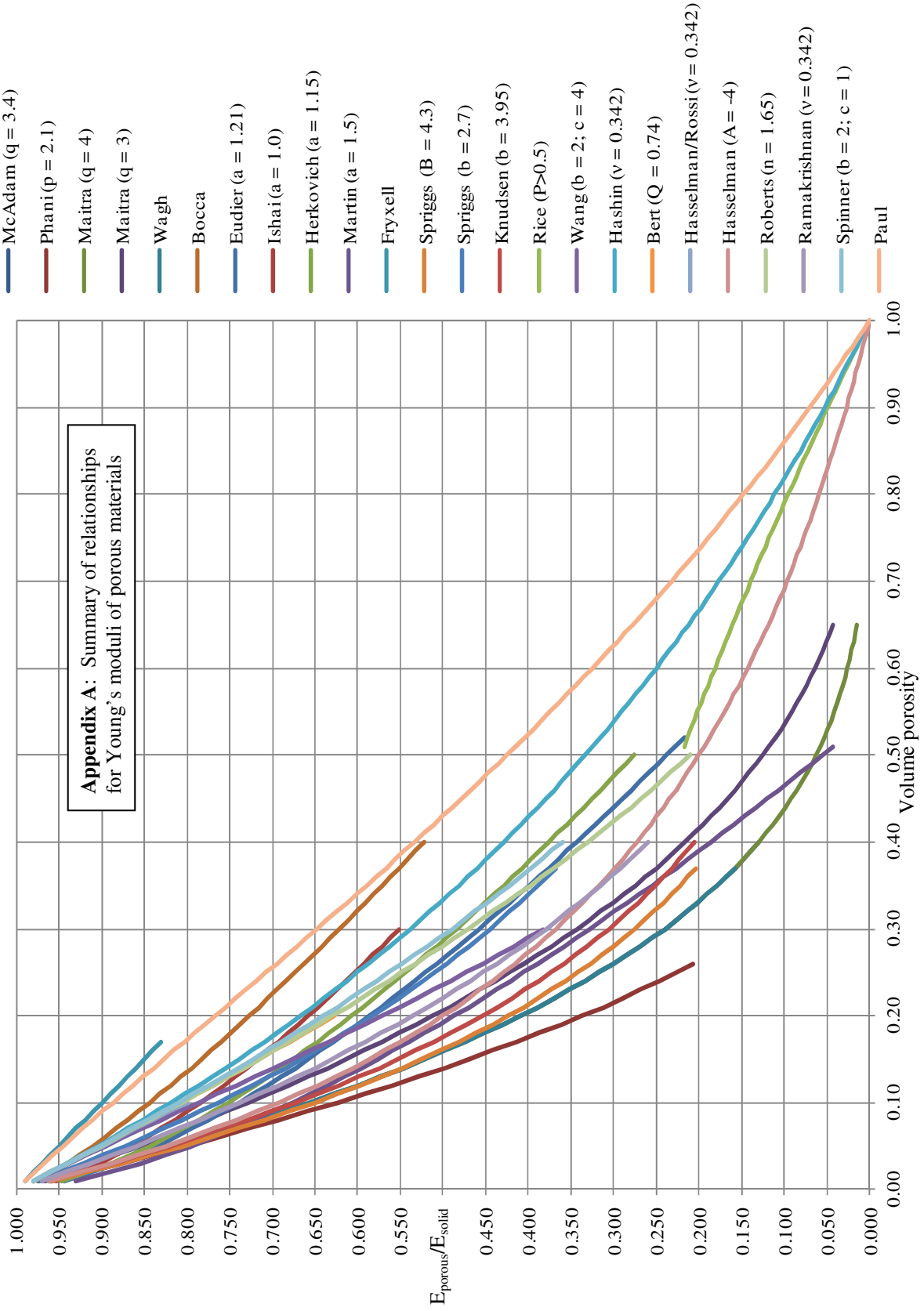
Appendix A: Summary of relationships for Young's moduli of porous materials
McAdam (q = 3.4)
Phani (p = 2.1)
Maitra (q = 4)
Maitra (q = 3)
Wagh
Bocca
Eudier (a = 1.21)
Ishai (a = 1.0)
Herkovich (a = 1.15)
Martin (a = 1.5)
Fryxell
Spriggs (B = 4.3)
Spriggs (b = 2.7)
Knudsen (b = 3.95)
Rice (P>0.5)
Wang (b = 2; c = 4)
Hashin (v = 0.342)
Bert (Q = 0.74)
Hasselman/Rossi (v = 0.342)
Hasselman (A = -4)
Roberts (n = 1.65)
Ramakrishnan (v = 0.342)
Spinner (b = 2; c = 1)
Paul
E_{porous}/E_{solid}
Volume porosity
1.000
0.950
0.900
0.850
0.800
0.750
0.700
0.650
0.600
0.550
0.500
0.450
0.400
0.350
0.300
0.250
0.200
0.150
0.100
0.050
0.000
0.00
0.10
0.20
0.30
0.40
0.50
0.60
0.70
0.80
0.90
1.00

Appendix B: Graphical representation of RVE evaluation scheme

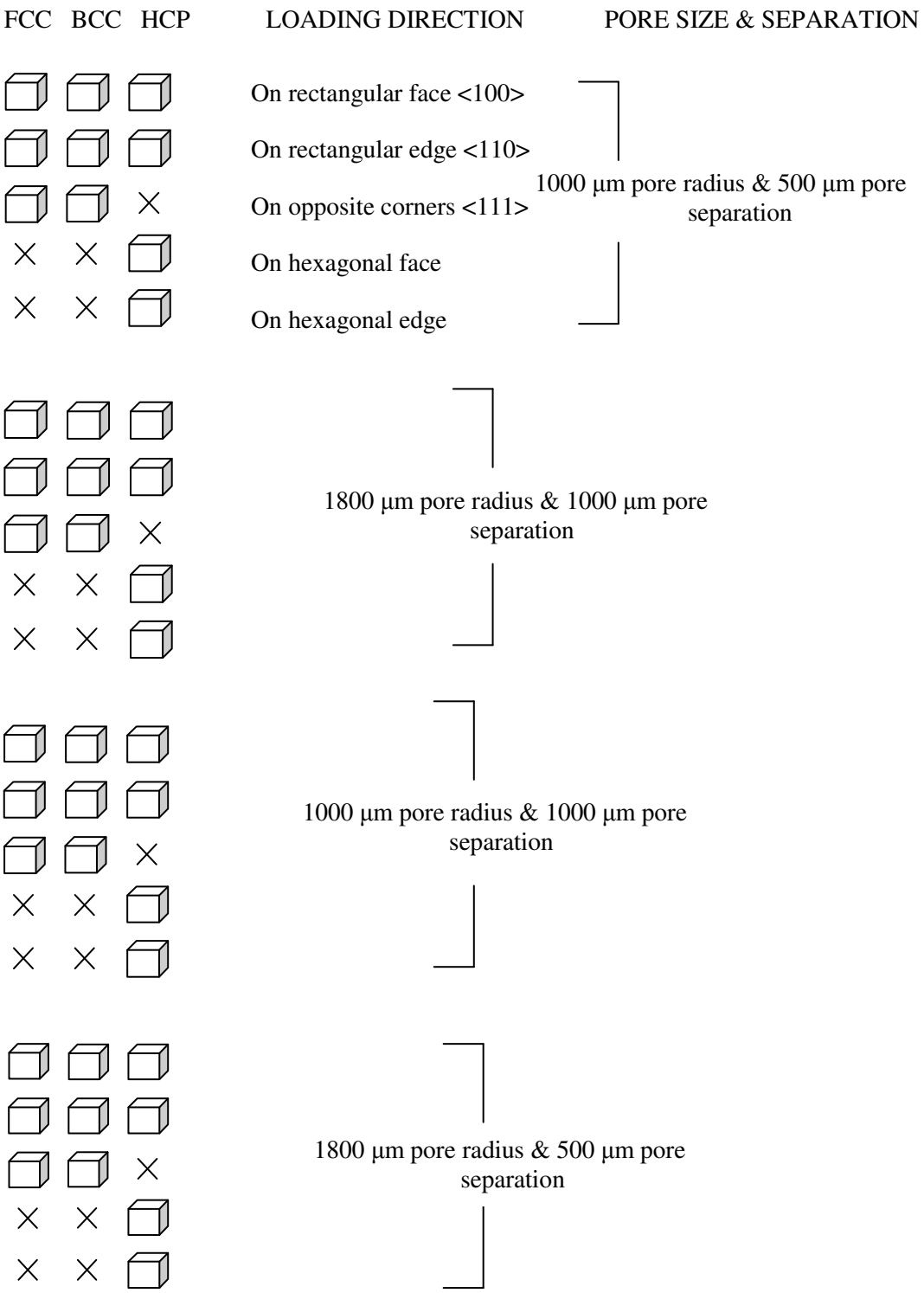

Appendix C: Summary of RVE dimensions by designation/load direction

RVE designation	Macroscopic structure FCC: *A* HCP: *B* BCC: *C*	Load direction on rect face: *1* on long edge: *2* on corner: *3* on hex face: *4* on hex edge: *5*	Pore Radius *r* (μm)	Minimum separation distance *s* (solid material between pores) (μm)	Resulting L dimension (minimum pore c-to-c dimension) (μm)	*r/L* ratio (ψ)	Volume porosity *P* (%)	x_{max} dimension of resulting RVE (mm)	z_{max} dimension of resulting RVE (mm)	y_{max} dimension of resulting RVE (mm)
1205A1	A	1	1200	500	2900	0.4138	42.0	8.202	8.202	8.202
1325A1	A	1	1320	500	3140	0.4204	44.0	8.881	8.881	8.881
105A1	A	1	1000	500	2500	0.4000	37.9	7.071	7.071	7.071
1206A1	A	1	1200	600	3000	0.4000	37.9	8.485	8.485	8.485
1407A1	A	1	1400	700	3500	0.4000	37.9	9.900	9.900	9.900
1608A1	A	1	1600	800	4000	0.4000	37.9	11.314	11.314	11.314
1809A1	A	1	1800	900	4500	0.4000	37.9	12.728	12.728	12.728
20010A1	A	1	2000	1000	5000	0.4000	37.9	14.142	14.142	14.142
7925A1	A	1	792	500	2084	0.3800	32.5	5.894	5.894	5.894
8865A1	A	1	886	500	2272	0.3900	35.1	6.426	6.426	6.426
1145A1	A	1	1140	500	2780	0.4101	40.8	7.863	7.863	7.863
1545A1	A	1	1536	500	3572	0.4300	47.1	10.103	10.103	10.103
2255A1	A	1	2250	500	5000	0.4500	54.0	14.142	14.142	14.142
2875A1	A	1	2875	500	6250	0.4600	57.7	17.678	17.678	17.678
105A2	A	2	1000	500	2500	0.4000	37.9	6.250	7.071	6.250
105A3	A	3	1000	500	2500	0.4000	37.9	7.500	7.500	7.500
105B1a	B	1	1000	500	2500	0.4000	37.9	6.250	6.124	6.495
105B2a	B	2	1000	500	2500	0.4000	37.9	6.495	6.124	6.250

RVE designation	Macroscopic structure FCC: *A* HCP: *B* BCC: *C*	Load direction on rect face: *1* on long edge: *2* on corner: *3* on hex face: *4* on hex edge: *5*	Pore Radius *r* (μm)	Minimum separation distance *s* (solid material between pores) (μm)	Resulting L dimension (minimum pore c-to-c dimension) (μm)	*r/L* ratio (ψ)	Volume porosity *P* (%)	x_{max} dimension of resulting RVE (mm)	z_{max} dimension of resulting RVE (mm)	y_{max} dimension of resulting RVE (mm)
105B4a	B	4	1000	500	2500	0.4000	37.9	6.250	6.495	6.124
105B5a	B	5	1000	500	2500	0.4000	37.9	5.941	6.250	5.951
1445C1	C	1	1440	500	3380	0.4260	42.1	7.806	7.806	7.806
1605C1	C	1	1600	500	3700	0.4324	44.0	8.545	8.545	8.545
105C1	C	1	1000	500	2500	0.4000	35.7	5.774	5.774	5.774
105C2	C	2	1000	500	2500	0.4000	34.8	5.103	5.774	5.103
105C3	C	3	1000	500	2500	0.4000	34.8	6.124	6.124	6.124
1810A1	A	1	1800	1000	4600	0.3913	35.5	13.011	13.011	13.011
1810A2	A	2	1800	1000	4600	0.3913	35.5	11.500	13.011	11.500
1810A3	A	3	1800	1000	4600	0.3913	35.5	13.800	13.800	13.800
1810B1a	B	1	1800	1000	4600	0.3913	35.5	11.500	11.268	11.951
1810B2a	B	2	1800	1000	4600	0.3913	35.5	11.951	11.268	11.500
1810B4a	B	4	1800	1000	4600	0.3913	35.5	11.500	11.951	11.268
1810B5a	B	5	1800	1000	4600	0.3913	35.5	10.931	11.500	10.950
1810C1	C	1	1800	1000	4600	0.3913	32.6	10.623	10.623	10.623
1810C2	C	2	1800	1000	4600	0.3913	32.6	9.390	10.623	9.390
1810C3	C	3	1800	1000	4600	0.3913	32.6	11.268	11.268	11.268
1010A1	A	1	1000	1000	3000	0.3333	21.9	8.485	8.485	8.485
1010A2	A	2	1000	1000	3000	0.3333	21.9	7.500	8.485	7.500

RVE designation	Macroscopic structure FCC: *A* HCP: *B* BCC: *C*	Load direction on rect face: *1* on long edge: *2* on corner: *3* on hex face: *4* on hex edge: *5*	Pore Radius *r* (μm)	Minimum separation distance *s* (solid material between pores) (μm)	Resulting L dimension (minimum pore c-to-c dimension) (μm)	*r/L* ratio (ψ)	Volume porosity *P* (%)	x_{max} dimension of resulting RVE (mm)	z_{max} dimension of resulting RVE (mm)	y_{max} dimension of resulting RVE (mm)
1010A3	A	3	1000	1000	3000	0.3333	21.9	9.000	9.000	9.000
1010B1a	B	1	1000	1000	3000	0.3333	21.9	7.500	7.349	7.794
1010B2a	B	2	1000	1000	3000	0.3333	21.9	7.794	7.349	7.500
1010B4a	B	4	1000	1000	3000	0.3333	21.9	7.500	7.794	7.349
1010B5a	B	5	1000	1000	3000	0.3333	21.9	7.129	7.500	7.141
1010C1	C	1	1000	1000	3000	0.3333	20.2	6.928	6.928	6.928
1010C2	C	2	1000	1000	3000	0.3333	20.2	6.124	6.928	6.124
1010C3	C	3	1000	1000	3000	0.3333	20.2	7.348	7.348	7.348
185A1	A	1	1800	500	4100	0.4390	50.1	11.597	11.597	11.597
185A2	A	2	1800	500	4100	0.4390	50.1	10.250	11.597	10.250
185A3	A	3	1800	500	4100	0.4390	50.1	12.300	12.300	12.300
185B1a	B	1	1800	500	4100	0.4390	50.1	10.250	10.043	10.652
185B2a	B	2	1800	500	4100	0.4390	50.1	10.652	10.043	10.250
185B4a	B	4	1800	500	4100	0.4390	50.1	10.250	10.652	10.043
185B5a	B	5	1800	500	4100	0.4390	50.1	9.743	10.250	9.760
185C1	C	1	1800	500	4100	0.4390	46.0	9.469	9.469	9.469
185C2	C	2	1800	500	4100	0.4390	46.0	8.369	9.469	8.369
185C3	C	3	1800	500	4100	0.4390	46.0	10.043	10.043	10.043

Appendix D: Summary of FE results by RVE designation

RVE designation	*r/L* ratio (ψ)	Volume porosity *P* (%)	Effective Young's modulus E_{BC1} (GPa)	Effective Young's modulus E_{BC2} (GPa)	Δ (E_{BC2} : E_{BC1}) (%)	Average effective Young's modulus (GPa)	Average effective Young's modulus (% of Ti6Al4V)	Effective Poisson's ratio, ν_x (BC2)	Effective Poisson's ratio, ν_z (BC2)	Δ (ν_z: ν_x) (%)	Average effective Poisson's ratio
1205A1	0.4138	42.0	41.725	42.141	1.0	41.933	36.8%	0.310	0.310	0.1	0.310
1325A1	0.4204	44.0	39.327	39.733	1.0	39.530	34.7%	0.310	0.311	0.2	0.310
105A1	0.4000	37.9	47.127	47.556	0.9	47.342	41.6%	0.310	0.310	0.1	0.310
1206A1	0.4000	37.9	47.130	47.560	0.9	47.345	41.6%	0.310	0.310	0.1	0.310
1407A1	0.4000	37.9	47.152	47.590	0.9	47.371	41.6%	0.310	0.310	0.1	0.310
1608A1	0.4000	37.9	47.103	47.535	0.9	47.319	41.6%	0.310	0.310	0.1	0.310
1809A1	0.4000	37.9	47.170	47.607	0.9	47.388	41.6%	0.310	0.310	0.1	0.310
20010A1	0.4000	37.9	47.139	47.584	0.9	47.362	41.6%	0.310	0.310	0.1	0.310
7925A1	0.3800	32.5	54.566	55.013	0.8	54.790	48.1%	0.310	0.310	0.1	0.310
8865A1	0.3900	35.1	50.910	51.358	0.9	51.134	44.9%	0.310	0.310	0.1	0.310
1145A1	0.4101	40.8	43.240	43.667	1.0	43.454	38.2%	0.310	0.310	0.1	0.310
1545A1	0.4300	47.1	35.842	36.192	1.0	36.017	31.6%	0.311	0.312	0.1	0.311
2255A1	0.4500	54.0	28.181	28.444	0.9	28.313	24.9%	0.314	0.315	0.1	0.315
2875A1	0.4600	57.7	24.484	24.730	1.0	24.607	21.6%	0.317	0.317	0.1	0.317
105A2	0.4000	37.9	48.867	49.527	1.3	49.197	43.2%	0.263	0.331	20.7	0.297
105A3	0.4000	37.9	50.662	50.805	0.3	50.734	44.6%	0.290	0.286	1.4	0.288
105B1a	0.4000	37.9	49.968	50.825	1.7	50.396	44.3%	0.304	0.287	5.9	0.295
105B2a	0.4000	37.9	49.307	49.841	1.1	49.574	43.6%	0.301	0.286	5.2	0.294
105B4a	0.4000	37.9	no mesh								

RVE designation	r/L ratio (ψ)	Volume porosity P (%)	Effective Young's modulus E_{BC1} (GPa)	Effective Young's modulus E_{BC2} (GPa)	Δ (E_{BC2} : E_{BC1}) (%)	Average effective Young's modulus (GPa)	Average effective Young's modulus (% of Ti6Al4V)	Effective Poisson's ratio, v_x (BC2)	Effective Poisson's ratio, v_z (BC2)	Δ (v_z: v_x) (%)	Average effective Poisson's ratio
105B5a	0.4000	37.9	47.458	48.853	2.9	48.156	42.3%	0.313	0.286	9.3	0.299
1445C1	0.4260	42.1	42.334	43.201	2.0	42.768	37.6%	0.305	0.305	0.0	0.305
1605C1	0.4324	44.0	39.862	40.879	2.5	40.370	35.5%	0.304	0.304	0.0	0.304
105C1	0.4000	35.7	51.637	52.501	1.6	52.069	45.8%	0.307	0.307	0.0	0.307
105C2	0.4000	34.8	53.799	55.378	2.9	54.588	48.0%	0.270	0.325	16.9	0.297
105C3	0.4000	34.8	56.508	57.494	1.7	57.001	50.1%	0.287	0.301	4.7	0.294
1810A1	0.3913	35.5	50.476	50.797	0.6	50.637	44.5%	0.310	0.310	0.1	0.310
1810A2	0.3913	35.5	52.109	52.771	1.3	52.440	46.1%	0.267	0.329	18.7	0.298
1810A3	0.3913	35.5	52.585	53.785	2.2	53.185	46.7%	0.291	0.288	1.2	0.290
1810B1a	0.3913	35.5	53.237	54.110	1.6	53.674	47.2%	0.305	0.290	5.1	0.297
1810B2a	0.3913	35.5	52.485	52.991	1.0	52.738	46.3%	0.302	0.289	4.4	0.295
1810B4a	0.3913	35.5	52.863	54.112	2.3	53.488	47.0%	0.292	0.290	0.6	0.291
1810B5a	0.3913	35.5	50.874	52.239	2.6	51.556	45.3%	0.313	0.289	8.4	0.301
1810C1	0.3913	32.6	54.583	55.440	1.5	55.011	48.3%	0.308	0.308	0.0	0.308
1810C2	0.3913	32.6	56.911	58.325	2.4	57.618	50.6%	0.274	0.324	15.6	0.299
1810C3	0.3913	32.6	59.412	60.486	1.8	59.949	52.7%	0.290	0.303	4.3	0.297
1010A1	0.3333	21.9	71.124	71.567	0.6	71.346	62.7%	0.315	0.315	0.1	0.315
1010A2	0.3333	21.9	72.139	72.590	0.6	72.365	63.6%	0.296	0.324	8.7	0.310
1010A3	0.3333	21.9	72.257	73.059	1.1	72.658	63.8%	0.307	0.305	0.5	0.306

RVE designation	r/L ratio (ψ)	Volume porosity P (%)	Effective Young's modulus E_{BC1} (GPa)	Effective Young's modulus E_{BC2} (GPa)	Δ (E_{BC2} : E_{BC1}) (%)	Average effective Young's modulus (GPa)	Average effective Young's modulus (% of Ti6Al4V)	Effective Poisson's ratio, v_x (BC2)	Effective Poisson's ratio, v_z (BC2)	Δ (v_z: v_x) (%)	Average effective Poisson's ratio
1010B4a	0.3333	21.9	no mesh								
1010B5a	0.3333	21.9	71.447	72.349	1.2	71.898	63.2%	0.317	0.305	4.0	0.311
1010C1	0.3333	20.2	73.856	74.492	0.9	74.174	65.2%	0.316	0.316	0.0	0.316
1010C2	0.3333	20.2	75.644	76.714	1.4	76.179	66.9%	0.298	0.324	7.9	0.311
1010C3	0.3333	20.2	no mesh								
185A1	0.4390	50.1	32.312	32.651	1.0	32.482	28.5%	0.312	0.313	0.1	0.313
185A2	0.4390	50.1	34.079	34.836	2.2	34.458	30.3%	0.240	0.346	30.7	0.293
185A3	0.4390	50.1	35.252	36.529	3.5	35.890	31.5%	0.285	0.276	3.3	0.280
185B1a	0.4390	50.1	34.486	35.301	2.3	34.893	30.7%	0.305	0.273	11.7	0.289
185B2a	0.4390	50.1	34.567	35.159	1.7	34.863	30.6%	0.302	0.275	10.0	0.288
185B4a	0.4390	50.1	34.604	35.618	2.8	35.111	30.9%	0.282	0.278	1.5	0.280
185B5a	0.4390	50.1	32.819	34.218	4.1	33.518	29.5%	0.315	0.277	13.8	0.296
185C1	0.4390	46.0	37.906	38.774	2.2	38.340	33.7%	0.303	0.303	0.0	0.303
185C2	0.4390	46.0	38.517	40.147	4.1	39.332	34.6%	0.258	0.329	21.8	0.293
185C3	0.4390	46.0	41.273	42.290	2.4	41.781	36.7%	0.276	0.297	7.1	0.286

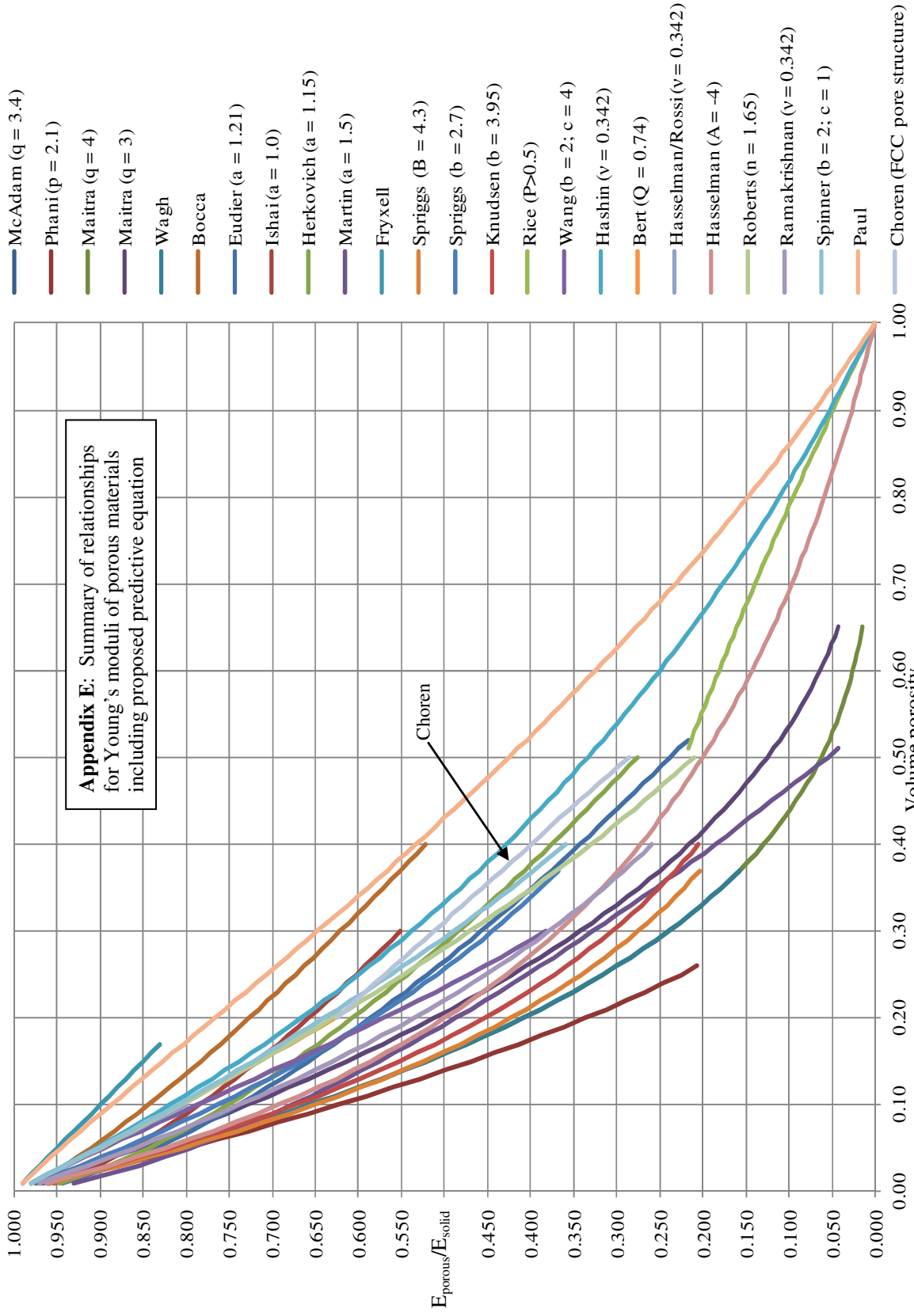
Appendix E: Summary of relationships for Young's moduli of porous materials including proposed predictive equation
McAdam (q = 3.4)
Phani (p = 2.1)
Maitra (q = 4)
Maitra (q = 3)
Wagh
Bocca
Eudier (a = 1.21)
Ishai (a = 1.0)
Herkovich (a = 1.15)
Martin (a = 1.5)
Fryxell
Spriggs (B = 4.3)
Spriggs (b = 2.7)
Knudsen (b = 3.95)
Rice (P>0.5)
Wang (b = 2; c = 4)
Hashin (v = 0.342)
Bert (Q = 0.74)
Hasselman/Rossi (v = 0.342)
Hasselman (A = -4)
Roberts (n = 1.65)
Ramakrishnan (v = 0.342)
Spinner (b = 2; c = 1)
Paul
Choren (FCC pore structure)
Choren
E_{porous}/E_{solid}
Volume porosity
1.000
0.950
0.900
0.850
0.800
0.750
0.700
0.650
0.600
0.550
0.500
0.450
0.400
0.350
0.300
0.250
0.200
0.150
0.100
0.050
0.000
0.00
0.10
0.20
0.30
0.40
0.50
0.60
0.70
0.80
0.90
1.00